



Norwegian University of
Science and Technology

Small Scale Tests of Creep in Pierre Shale

Anna Kay Ying Guan

Petroleum Geoscience and Engineering

Submission date: June 2016

Supervisor: Erling Fjær, IPT

Norwegian University of Science and Technology

Department of Petroleum Engineering and Applied Geophysics

Preface

This Master's thesis is the culmination of five years' study within the field of Petroleum Engineering in the Department of Petroleum Engineering and Applied Geophysics at the Norwegian University of Science & Technology. This thesis has been written during spring 2016 in cooperation with Det norske oljeselskap ASA and SINTEF Petroleum Research. SINTEF has specifically provided facilities and equipment for the experiments, while Det norske has given me strong academic support during the course of this thesis.

I would really like to extend my gratitude to my supervisor Erling Fjær for the enthusiastic guidance and support throughout the thesis work. I would also like to thank my co-supervisor Olav-Magnar Nes, Senior Advisor Rock Mechanics at Det norske, for feedback and help in finding relevant and interesting reading material. Their enthusiasm has truly been inspiring and encouraging. Jørn Stenebråten, Eyvind Sønsterbø and Lars Erik Walle from SINTEF also deserve gratitude for instructions and help during the entire work in the laboratory.

Anna Guan

Trondheim, June 2016

Abstract

The impressive scope of using shale as a permanent well barrier for plug and abandonment (P&A) operations has lately gained much attention in the petroleum industry. Shale is observed to have a natural self-sealing effect as a result of delayed deformation of the rock. This effect is most likely related to creep. Creep tests in the laboratory are normally done on standard core plugs, but these tests are very time-consuming due to ion and temperature diffusion. This thesis will therefore use small mm-size samples to study the creep properties in shale, utilizing a technology developed by SINTEF Petroleum Research. As the use of small samples involves pure shear failure, the effect of pore pressure is minimized.

The objective of this Master's thesis is to investigate the applicability of small scale tests of creep in Pierre shale, through a study on how chemical properties of the pore fluid affect the creep process, primarily pH and chemical activity. The experiments are performed with a shale puncher tool on 3 mm samples, saturated with either marcol oil, brine or hydrochloric acid. The testing procedure involves applying an axial force on the puncher tool, preferably in displacement control, while measuring the axial displacement and force. Creep experiments are conducted in order to study the creep development under constant load, while strain-rate tests are run with various rates of deformation to examine the resulting effect. The P-wave velocity of the samples is also measured through continuous wave technique (CWT) in order to quantify the sample heterogeneity.

The proposed study revealed that Pierre shale undergoes an extensive time-dependent deformation in response to applied axial force. In the creep tests, it is observed that the maximum axial force required to punch the sample is dependent on the loading path and the duration of each loading. In the strain-rate tests, it is found that the weakest sample is the one with fastest displacement rate, indicating that there may exist a pore pressure effect. A time-dependent effect is also observed in response to fluid exposure; an increase in P-wave velocity for the oil-saturated samples, and conversely a decrease for the brine-rich samples. Brine is used to alter the chemical properties of the pore fluid, while a change of pH is obtained by the use of hydrochloric acid. The effect of fluid exposure is shown to be of significance, as a considerably weakening in rock strength of the samples is seen. The experimental results proved the possibility in obtaining some information about creep behaviour using the puncher technology. However, further investigation and improvements are required before any applicable conclusions can be drawn.

Sammendrag

Denne masteroppgaven undersøker hvorvidt anvendelsen av små skiferprøver kan brukes til å studere kryppoppførsel i skifer. En rekke eksperimenter har blitt gjennomført med formål om å undersøke hvordan tidsforsinket deformasjon i skifer kan påvirkes av kjemiske egenskaper i pore fluidet, hovedsakelig pH og kjemisk aktivitet. Ved hjelp av et puncher utstyr som er utviklet av SINTEF Petroleum, ble eksperimentene utført på små skiveformet prøver av Pierreskifer med en prøvetykkelse på 3 mm. Utstyret klemmer parallelt både over og under prøven slik at et hull blir trykket gjennom, og et rent skjærbrudd vil dermed oppstå i prøven.

For å kunne studere mer på den tidsforsinkede effekten i skifer, ble 16 kryptester gjennomført med en lastramme med dødvekter. Dødvekter ble lastet opp stegvis, slik at endringen fra trinn til trinn vil forhåpentligvis kunne si noe om kryptutviklingen i skifer under konstant spenningsbelastning. Videre ble 9 styrketester gjennomført ved hjelp av en-aksiell elektromekanisk lastramme. Ulike deformasjonsrater med kontinuerlig spenningsbelastning ble brukt til å undersøke hvordan ulike rater kan påvirke styrken på skifer. Noen av prøvene ble også mettet med brine eller saltsyre for å undersøke effekten av fluid endring og kjemisk aktivitet. P-bølgehastigheter ble også målt i forkant av testene for å vurdere homogeniteten i prøvene og hvorvidt disse blir påvirket av en kjemisk endring i skiferbergartens pore fluid.

Fra de eksperimentelle dataene, ble det funnet ut at Pierreskiferen kan gjennomgå en betydelig tidsavhengig deformasjon som følge av en økning i aksiellspenning. I kryptestene ble det observert at den maksimale spenningen som kreves for å trykke et hull gjennom prøven er avhengig av spenningsmengden som lastes opp hver gang og varigheten mellom hver opplasting. I styrketestene viste det seg at den svakeste skiferprøven er den som ble utsatt for høyest deformasjonsrate, noe som indikerer det kan eksistere en poretrykkseffekt. Det ble også oppdaget en tidsavhengig effekt som følge av fluid eksponering, hvor en økning i P-bølgehastighet i prøver som har blitt lagret i marcololje i over en lengre periode. Motsatt, en minking i P-bølgehastighet har oppstått i prøver som er blitt eksponert for brine med samme tidsperiode. Effekten av fluid eksponering har vist seg til å være av betydning, ettersom det har blitt observert en vesentlig svekkelse i skiferens styrke på grunn av kjemiske effekter. Selv om eksperimentene på de små prøvene viste seg til å kunne gi noe informasjon om kryppoppførselen i skifer, er det likevel nødvendig med videre undersøkelser og forbedringer før eventuelle konklusjoner kan trekkes.

Table of Contents

Preface	iii
Abstract	v
Sammendrag	vii
Table of Contents	ix
List of Figures	xii
List of Tables	xiv
Nomenclature	xv
List of Abbreviations	xvi
1 Introduction	1
1.1 Background	1
1.2 Thesis Structure	2
2 Understanding Shale	3
2.1 Shale as Annular Barrier	3
2.2 Shale Properties in General	5
2.3 Pierre Shale Characteristics	8
3 Relevant Background Theory	11
3.1 Failure Mechanics	11
3.1.1 Tensile Failure	11
3.1.2 Shear Failure	12
3.1.3 Compaction Failure	15
3.2 Time-Dependent Deformation in Shale	16
3.2.1 Introduction to Creep	16
3.2.2 Stages of Creep	17
3.2.3 Internal Processes Causing Creep in Shale	19
3.2.4 Distinguishing Between Consolidation and Creep	21
3.2.5 Thermoelasticity	21
3.2.6 Chemical Effects of Pore Fluid	22
3.3 Acoustic Waves	24
3.3.1 Wave Propagation in Rocks	24
3.3.2 P-waves	25
3.3.3 P-waves and Pore Fluid Exposure in Porous Materials	26
3.3.4 Temperature and Anisotropic Influence	27
3.3.5 Static and Dynamic Moduli	27
4 Experimental Setups and Procedures	29

4.1	Purpose.....	29
4.2	Equipment Principles	29
4.2.1	Continuous Wave Technique.....	29
4.2.2	Shale Puncher Tool.....	30
4.2.3	Loading Paths	32
4.3	Sample Preparation	33
4.3.1	Type of Exposure Fluids.....	34
4.3.2	Test Matrix for the Creep Tests	34
4.3.3	Test Matrix for the Strain-rate Tests.....	36
4.4	CWT.....	36
4.4.1	Calibration	36
4.4.2	Thickness and P-Wave Velocity.....	36
4.4.3	Test Procedure	37
4.5	LVDT.....	38
4.5.1	Setup	38
4.5.3	Calibration	38
4.6	Load Frame and Load Cell.....	39
4.6.1	Setup.....	40
4.6.2	Test Procedure	40
4.7	Electromechanical Load Frame	40
4.8	Shale Puncher Test.....	41
4.8.1	Procedure for Creep Test.....	43
4.8.2	Procedure for Strain-rate Test.....	43
4.9	Risk Assessment	45
5	Experimental Results.....	47
5.1	P-Wave Velocities and Cohesion Calculations.....	48
5.1.1	P-wave velocity for Pierre Shale 346_2 - 01 to 10.....	48
5.1.2	Cohesion Calculations for Pierre 346_2 – 01 to 10.....	50
5.2	Puncher Tests with Stepwise Loading Path	51
5.2.1	Readjusted Thickness of the Oil Samples.....	52
5.2.2	Samples Immersed in Oil.....	53
5.2.3	Samples Immersed in Brine.....	56
5.2.4	Deviating Trends	60
5.2.5	Estimate of Temperature Effect.....	62
5.3	Puncher Tests with Continuous Loading Path	64
5.3.1	Axial Displacement measured from Crosshead versus LVDT	64
5.3.2	Axial force-displacement Curves	65
5.3.3	Analysis of the Axial Force-Displacement Curves.....	68
5.4	Reliability of the Puncher Method	69
6	Discussion	71
6.1	Chemical Effects.....	71

6.2	Effect of Changing the pH	72
6.3	Effect of Pore Pressure.....	73
6.4	Puncher Tests Discussion.....	73
6.5	Temperature Sensitivity	74
6.5	Sources of Error	75
6.5.1	Parallelism of the Disk-shaped Samples.....	75
6.5.2	Sample Thickness for the Oil Samples.....	75
6.5.3	P-Wave Velocity.....	75
6.5.4	Sample Desiccation	75
6.5.5	Pore Pressure Effects.....	76
6.5.6	Temperature Effects	76
6.5.7	Noise from LVDT	76
6.5.8	Noise from Load Cell and Limitation of Load Frame	77
6.5.9	Time Increments	77
7	Conclusion.....	79
8	Future Work	81
	Bibliography.....	83
Appendix A	Results: Puncher Test with Stepwise Loading Path	i
Appendix B	Results: Puncher Test with Cont. Loading Path.....	vii
Appendix C	Results: Cohesion Calculations	xii
Appendix D	Calculations of Test Speeds	xiii
Appendix E	Additional Tables	xv
Appendix F	Risk Assessment.....	xvii
Appendix G	Pictures of Shale Samples	xix

List of Figures

FIGURE 2- 1 SCHEMATIC OF HOW CREEPING SHALE MAY FORM A SEALING BARRIER AROUND A WELL.....	3
FIGURE 2- 2 (A) SILICON TETRAHEDRAL (B) TETRAHEDRAL SHEET (CHEN, 2015).....	5
FIGURE 2- 3 (A) OCTAHEDRAL FORMED BY ALUMINIUM OR MAGNESIUM (B) OCTAHEDRAL SHEET (CHEN, 2015)..	6
FIGURE 2- 4 HYDROGEN BONDING ON THE SOLID SURFACE (CHEN, 2015).....	6
FIGURE 3- 1 TENSILE FAILURE (FJÆR ET AL., 2008)	12
FIGURE 3- 2 SHEAR FAILURE (FJÆR ET AL., 2008).....	12
FIGURE 3- 3 MOHR-COULOMB CRITERION IN SHEAR-NORMAL STRESS PLANE (STENEBRÅTEN ET. AL., 2008)	14
FIGURE 3- 4 GRAIN ORIENTATION DUE TO CLOSER PACKING (FJÆR ET AL., 2008).....	15
FIGURE 3- 5 LOCATION OF FAILURE MODES IN PRINCIPAL STRESS SPACE FOR TENSILE, SHEAR AND COMPACTION FAILURE (FJÆR ET AL., 2008)	15
FIGURE 3- 6 STRESS-STRAIN CURVE (A) FOR AN ELASTIC MATERIAL (B) FOR AN VISCOELASTIC MATERIAL (MEYERS & CHAWLA, 1999).....	17
FIGURE 3- 7 CHARACTERISTIC STRAIN RESPONSE FOR ROCK MATERIALS UNDER CONSTANT STRESS, SHOWING TRANSIENT, STEADY STATE AND ACCELERATING CREEP (FJÆR ET AL., 2008).....	17
FIGURE 3- 8 CREEP RESPONSE TO DIFFERENT VALUES OF APPLIED STRESS (FJÆR ET AL., 2008).....	18
FIGURE 3- 9 RELATIONSHIP BETWEEN TEMPERATURE AND STRESS (DOWLING, 2007)	22
FIGURE 3- 10 K ⁺ ION AND Na ⁺ IONS ARE MORE EFFECTIVE THAN Ca ²⁺ ION IN REDUCING CLAY HYDRATION DUE TO THEIR SMALL SIZES (CHEN, 2015)	23
FIGURE 3- 11 - LEFT: A CRACK CLOSING DUE TO INCREASING STRESS. RIGHT: NON-LINEAR DEFORMATION CAUSED BY SEVERAL CRACKS CLOSING. (STROISZ & FJÆR, 2011).....	26
FIGURE 4- 1 DRAWING SHOWING THE PARTS MAKING UP TO THE PUNCHER TOOL (STENEBRÅTEN ET AL., 2008).	30
FIGURE 4- 2 DRAWING SHOWING THE ASSEMBLED PUNCHER TOOL (STENEBRÅTEN ET AL., 2008)	31
FIGURE 4- 3 DRAWING SHOWING THE DIFFERENCE IN FAILURE REGION OF A PUNCHER TEST AND A STANDARD TRI- AXIAL COMPRESSION	31
FIGURE 4- 4 SKETCH OF STRESS PATHS; CONTINUOUS AND STEPWISE	32
FIGURE 4- 5 GRINDING PROCESS DURING SAMPLE PREPARATION	33
FIGURE 4- 6 A METAL GRINDING UNIT TO CONTROL THE THICKNESS.....	33
FIGURE 4- 7 THE DIMENSIONS OF THE SHALE SAMPLES	33
FIGURE 4- 8 ACOUSTIC VELOCITY MEASUREMENTS USING CW TECHNIQUE. THE SAMPLE IS CLAMPED BETWEEN TO TRANSDUCERS, AS INDICATED WITH A YELLOW ARROW.	37
FIGURE 4- 9 LVDT CONNECTED TO THE PUNCHER TOOL.....	38
FIGURE 4- 10 LOAD FRAME. THE RIGHT PICTURE SHOWS THE LOAD FRAME, WHILE THE LEFT PICTURE SHOWS LOAD FRAME WITH THE PUNCHER TOOL AND WEIGHT PLATES	39
FIGURE 4- 11 LOAD CELL RECORDING THE TOTAL AXIAL FORCE APPLIED TO THE LOAD FRAME.....	39
FIGURE 4- 12 THE PUNCHER TOOL PLACED INSIDE THE ELECTROMECHANICAL LOAD FRAME	40
FIGURE 5- 1 P-WAVE VELOCITIES FOR OIL SAMPLES BEFORE AND AFTER STORAGE	49
FIGURE 5- 2 P-WAVE VELOCITIES FOR BRINE SAMPLES BEFORE AND AFTER STORAGE.....	49
FIGURE 5- 3 OIL SAMPLE 346_2_03: PUNCH TEST SHOWING THE AXIAL FORCE APPLIED AND THE RESULTING DISPLACEMENT.....	53
FIGURE 5- 4 OIL SAMPLE 346_2_03: ZOOM-IN FORMAT OF THE CHARACTERISTIC S-CURVE OF CREEP AFTER THE FIRST STEP OF 39.24 N AXIAL FORCE IS APPLIED.....	54

FIGURE 5- 5 OIL SAMPLE 346_2_04: PUNCH TEST SHOWING THE AXIAL FORCE APPLIED AND THE RESULTING DISPLACEMENT.....	54
FIGURE 5- 6 OIL SAMPLE 346_2_05: PUNCH TEST SHOWING THE AXIAL FORCE APPLIED AND THE RESULTING DISPLACEMENT.....	55
FIGURE 5- 7 BRINE SAMPLE 346_2_07: PUNCH TEST SHOWING THE AXIAL FORCE APPLIED AND THE RESULTING DISPLACEMENT.....	56
FIGURE 5- 8 BRINE SAMPLE 346_2_07: ZOOM-IN FORMAT OF THE CREEP STAGES.....	57
FIGURE 5- 9 COMPARISON OF THE EXPERIMENTAL RESULT OF BRINE SAMPLE 346_2_07 AND A TYPICAL CREEP RESPONSE TO VARYING APPLIED STRESS.....	58
FIGURE 5- 10 BRINE SAMPLE 346_2_12: PUNCH TEST SHOWING THE AXIAL FORCE APPLIED AND THE RESULTING DISPLACEMENT.....	58
FIGURE 5- 11 BRINE SAMPLE 346_2_12: ZOOM-IN FORMAT TO STUDY THE CREEP STAGES.....	59
FIGURE 5- 12 COMPARISON OF THE EXPERIMENTAL RESULTS OF THE BRINE SAMPLE 346_2_12 AND A TYPICAL STRAIN RESPONSE CURVE FOR MATERIALS UNDER CONSTANT STRESS.....	59
FIGURE 5- 13 BRINE SAMPLE 346_2_13 (EXPOSURE TIME: 15 MINUTES): PUNCH TEST SHOWING STRESS VS STRAIN. AN INCREASE IN STRAIN IS OBSERVED.....	60
FIGURE 5- 14 HYDROCHLORIC ACID SAMPLE 346_2_15 (EXPOSURE TIME: 15 MINUTES): PUNCH TEST SHOWING STRESS VS STRAIN. AN INCREASE IN STRAIN IS OBSERVED.....	61
FIGURE 5- 15 HYDROCHLORIC ACID SAMPLE 346_2_16 (EXPOSURE TIME: 15 MINUTES): PUNCH TEST SHOWING STRESS VS STRAIN. AN INCREASE IN STRAIN IS OBSERVED.....	61
FIGURE 5- 16 OIL SAMPLE 346_2_01 (EXPOSURE TIME 30 DAYS): PUNCH TEST SHOWING STRESS VS STRAIN. AN INCREASE IN STRAIN IS OBSERVED.....	62
FIGURE 5- 17 SAMPLE 223_3_07 (SATURATED WITH HYDROCHLORIC ACID): AN EXAMPLE OF THE DIFFERENCE IN MEASURED AXIAL DISPLACEMENT BETWEEN THE CROSSHEAD AND THE LVDT	64
FIGURE 5- 18 AXIAL FORCE-DISPLACEMENT CURVE FOR 223_3_01, 02 AND 03 (IMMERSED IN MARCOL OIL).....	65
FIGURE 5- 19 AXIAL FORCE-DISPLACEMENT CURVE FOR 223_3_04, 05 AND 06 (IMMERSED IN BRINE).....	66
FIGURE 5- 20 AXIAL FORCE-DISPLACEMENT CURVE FOR 223_3_07 AND 223_3_09 (IMMERSED IN HYDROCHLORIC ACID).....	66
FIGURE 5- 21 AXIAL FORCE-DISPLACEMENT CURVE FOR 223_3_08 (IMMERSED IN HYDROCHLORIC ACID).....	67
FIGURE 5- 22 MOHR CIRCLE AND FAILURE LINE: THE EFFECT OF INCREASING PORE PRESSURE (FJÆR ET AL., 2008)	68
FIGURE 5- 23 DUMMY TEST WITH PLEXIGLAS TO INVESTIGATE THE TILT EFFECT.....	69

List of Tables

TABLE 2- 1 SHALE TYPES AND THEIR MAIN PROPERTIES (FAM & DUSSEAULT, 1998)	7
TABLE 2- 2 COMMON SHALE PROPERTIES (FJÆR ET AL., 2008)	8
TABLE 2- 3 COMMON PIERRE SHALE PROPERTIES (FJÆR ET AL., 2008)	8
TABLE 3- 1 COMMON P-WAVE VELOCITIES FOR SHALE AND WEAK SHALE FROM THE NORTH SEA (FJÆR ET AL., 2008).....	25
TABLE 4- 1 TEST MATRIX 1 FOR 346_2_01 TO 10 SAMPLES.....	35
TABLE 4- 2 TEST MATRIX 2 FOR 346_2_ 11 TO 16	35
TABLE 4- 3 TEST MATRIX FOR 233_3 SAMPLES	36
TABLE 4- 4 CWT INITIAL INPUTS.....	37
TABLE 4- 5 PROCEDURE FOR INSTALLING SHALE SAMPLES IN THE PUNCHER	42
TABLE 4- 6 LIST OF THE RATES OF DISPLACEMENT (TEST SPEEDS) USED FOR RUNNING STRAIN-RATE TESTS	44
TABLE 5- 1 P-VELOCITY SUMMARY TABLE FOR 346_2_01 TO 10	48
TABLE 5- 2 TABLE 5- 2 COHESION OF THE OIL SAMPLES 346_2_01 TO 05	50
TABLE 5- 3 COHESION OF BRINE SAMPLES 346_2_06 TO 10.....	50
TABLE 5- 4 CONVERSION TABLE FROM KG TO N	51
TABLE 5- 5 CALCULATIONS FOR A ROUGH ESTIMATE OF TEMPERATURE CHANGE IN THE LABORATORY.....	63

Nomenclature

A	Area
a_{sh}	Chemical activity of pore fluid in shale
a_f	Chemical activity of fluid
C_o	Unconfined compressive strength
c_o	Relative pressure amplitude
d	Grain size
E	Young's modulus
E_{eff}	Effective Young's modulus
F	Friction occurring due to sliding along contact points or closed micro-cracks in the material during shear loading
G	Shear modulus
G_c	Critical strain energy
K	Bulk modulus
K_I	Tensile stress intensity factor
k	Permeability of the rock
Q	Coefficient dependent on shape and orientation of the crack
\vec{Q}	Fluid flow rate
P_I	A measure of a process involving crushing of asperities at the grain boundaries
p	Pore pressure
S_o	Inherent shear strength/cohesion
T_f	Formation temperature
T_o	Tensile strength
t	Time
v_p	P-wave velocity
β	Failure angle
ε	Strain/Deformation
ε_{ch}	Chemically induced strain by ion exchange
η_f	Dynamic viscosity of the fluid
φ	Frictional angle
μ	Coefficient of internal friction
ρ	Density
σ	Stress
σ'	Principal stress
σ'_1	Maximum principal stress
σ'_2	Intermediate principal stress
σ'_3	Minimum principal stress
σ^*	Stress where a crack is propagated
σ_f	Stress where fracture occurs

σ_{θ}	Hoop stress
σ_x^c	Stress level the crack closes
σ_y	Stress for the onset of micro-plasticity
σ_z	Axial stress
σ_{peak}	Peak stress
τ_{max}	Critical shear stress
ν	Poisson's ratio
ξ	Crack density

List of Abbreviations

CCS	Carbon Capture and Storage
CW	Continuous wave
CWT	Continuous wave technique
HCl	Hydrochloric Acid
LVDT	Linear variable differential transformer
NaCl	Sodium Chloride
NCS	Norwegian Continental Shelf
P&A	Plug and abandon
PP&A	Permanent plug and abandon
UCS	Unconfined compressive strength

1 Introduction

1.1 Background

When the production from a well is no longer profitable, the well is either permanently plugged and abandoned (PP&A) or the slot is re-used by sidetracking a new wellbore (often known as slot recovery). The purpose of P&A is to establish permanent barriers to prevent the undesired migration of hydrocarbons to the surface when the well is abandoned without surveillance. The development of new technology within PP&A is currently of great interest in the petroleum industry, as the traditional P&A operations are both expensive and time-consuming.

Recent studies have focused on improving the existing solutions, with the impressive scope of using the formation, specifically shale, as a permanent barrier element. Generally, a well under operation is traditionally sealed by pumping cement from the casing shoe and up to a certain length in the annulus, leaving longer sections in the annulus un-cemented. However, in case of permanently plugging and abandoning a well, more stringent requirements apply. According to NORSOK Standard D-010, a material must fulfill the following requirements to be qualified as a barrier: being impermeable, providing long-term integrity, being non-shrinking, behaving ductile, wetting and resistant to chemicals.

In shale sections, the annulus is not filled with any cement. During and after drilling through such formations, it is observed that the rock moves inward towards the casing and begins to seal off the well. Thus, this self-sealing effect can potentially enable the rock to fulfill the requirements for a PP&A barrier as a result of delayed deformation of the rock. The self-sealing effect occurs when the boundary conditions are presumably stable, which is most likely related to creep. Creep is a complex process, being highly sensitive to both stress and temperature. During drilling, the rock will be exposed to a drilling fluid with chemical properties that may also have an impact on the process. Some of these conditions can be modified to some extent, which can possibly improve the sealing efficiency of the shale barrier for a given situation. This is often related to the mechanical properties of the shale, which means that obtaining better knowledge about these properties will be useful in optimizing drilling procedures. If shale succeeds to preserve as an alternative to the regular annular barrier, P&A and slot recovery operations can be significantly simplified and thus greatly reducing drilling cost.

Laboratory testing of such effects is normally done on standard core plugs. For shales, preserved core materials are rarely available. Shale cores are often heavily fractured, which makes it difficult to extract standardized cores. Moreover, coring overburden shales are not normally done by oil companies. Finally, running such tests are very time consuming due to

temperature diffusion and ion diffusion. These are slow processes that take long time to establish uniform conditions in the samples.

SINTEF Petroleum Research has initiated a 3 year's project exploring the shale potential to function as a permanent barrier after well abandonment. This research is conducted in cooperation with The Norwegian Research Council and five oil companies. During this project, the shale properties will be carefully examined. In response to the mentioned problems, this thesis will investigate the processes behind the self-sealing effect in shale on smaller shale samples. The tests will be conducted on small mm-sized samples using the Shale Puncher Technology developed by SINTEF Petroleum Research (Nes et al., 1998; Stenebråten et al., 2008). Testing on small samples can be much faster as they are easily prepared, but the most important reason is that the time needed to obtain pore pressure equilibrium is significantly reduced. The objective of this Master's thesis is therefore to investigate applicability of running such tests for studies of creep effects, by studying how chemical properties of the pore fluid affect the creep process.

1.2 Thesis Structure

The thesis is structured into 7 main parts:

- *Chapter 2: Understanding Shale* is an overview of the annular barrier requirements and the shale properties
- *Chapter 3: Relevant Background Theory*, an introduction to rock mechanics and continues to focus on the processes involved in the sealing mechanism
- *Chapter 4: Experimental Details and Procedures* gives a description of how the equipment work, setup, sample preparation and experimental procedures
- *Chapter 5: Experimental Results* is an overview and explanation of the results obtained from the experiments. Brief analyses of the results can also be found. All experimental data is attached in Appendix A, B and C.
- *Chapter 6: Discussion*, and extension of the previous chapter. Interesting findings and relationships will be further discussed in this part. Potential sources of error as will also be identified
- *Chapter 7: The Conclusion* part summarizes the major findings and results
- *Chapter 8: Future Work*, the recommendations for further investigation will be presented

2 Understanding Shale

Shale is believed to have important characteristics that can generate a self-sealing effect. Yet, the shale properties and the involved processes are not fully understood. This section will therefore emphasize the importance of understanding shale as a rock, where the involved processes of the self-sealing mechanism will be briefly introduced.

2.1 Shale as Annular Barrier

A permanent well barrier is required to include all annuli (Abshire et al., 2012). The barrier must extend to the full cross section for the well that seals both vertically and horizontally. In order to qualify *shale* as an annular barrier, the following requirements must also be satisfied (Williams et al., 2009):

- The barrier must be shale
- The rock strength of the shale must be able to withstand the maximum expected pressure that can be exerted on it, i.e. the worst case scenario must be calculated by extrapolating the maximum reservoir pressure to the base of the expected shale barrier via an annular gas column
- The displacement mechanism of the shale must be able to preserve the well barrier properties
- The barrier must extend and seal over the full circumference of the casing, and over a proper interval along the well

The shale can form a barrier element by creeping towards the casing and thus sealing off the wellbore. This process is illustrated in Figure 2- 1, showing a wellbore with casing inside. The desired situation is where the shale moves inward towards the casing and thereby reducing the gap (annulus) between the casing and the formation.

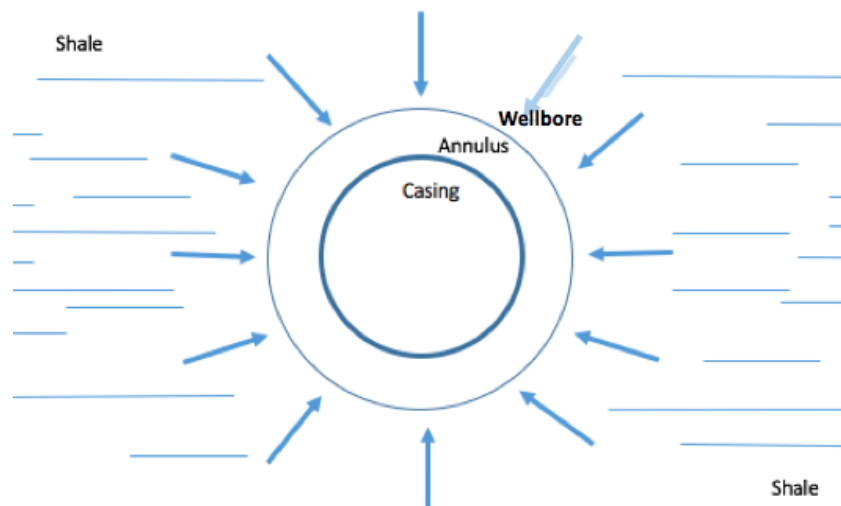


Figure 2- 1 Schematic of how creeping shale may form a sealing barrier around a well

Several displacement mechanisms are believed to contribute this self-sealing effect of the shale. The displacement is often observed on the Norwegian Continental Shelf (NCS) as a reduction in wellbore diameter during and after drilling (Williams et al., 2009). The key displacement mechanisms are most likely related to (Fjær E. , 2006);

- Creep
- Consolidation
- Shear or tensile failure
- Compaction failure and/or consolidation
- Liquefaction
- Thermal expansion/contraction
- Chemical effects

The most common modes of failure are shear and tensile failure, which is often observed in shale sequences. This is most likely to occur when the mud weights fall below the pore pressure. The reduction of the mud density behind casing may therefore be of significance of initiating this failure process (Williams et al., 2009).

Compaction failure and consolidation are likely to occur once there is a change in applied stress exerted on the formation. When the material is compressed, the grains in the rock may loosen and then be pushed into the open pore space, resulting in a closer packing of the material (Fjær et al., 2008). Consolidation is a time-dependent process, where the deformation of the rock continues for a long time after a change in structural load (Fjær et al., 2008). During the deformation, the pore pressure need to be re-equilibrate after a change in stress state.

Thermal expansion/contraction is also suggested to be relevant for the deformation of shale, as materials can either expand or contract under a change in temperature. Thermal response can be important in escalating the process of deforming the formation (Williams et al., 2009). Also, when the formation is exposed to drilling fluid (or other external fluids), the formation may react chemically with the mud and alter the displacement process considerably.

Creep deformation is the time-dependent process that is suggested to have significant impact on shale preserving as an annular barrier element (Williams et al., 2009). Compared to consolidation, creep is related to viscoelastic behaviour of the solid framework rather than pore pressure.

2.2 Shale Properties in General

Shale makes up to one-half to three-fourths of all sedimentary rocks, and underlies more of the Earth's land surface than any other rock (Fooks & Dusseault, 1996). Shale is a fissile fine-grained sedimentary rock with high proportion of clay minerals, usually with a mineral content of 40% or higher (Fjær et al., 2008). Shale is generally recognized as an impermeable rock with extremely low permeability (nanoDarcy range), while the porosity can still vary from less than 1% and up to 70% (Fjær et al., 2008). In addition to clay minerals, shale consists also of structurally bound water with dissolved ions in a state of mechanical, chemical and electrostatic equilibrium (Fjær et al, 2002). If the material is somehow altered, such that the free surface is exposed, this state of equilibrium will be disturbed. Shale has also large specific surface areas due to the narrow pore spaces. These surfaces have negative surface charge, which attract cations from the pore water. This complicates the measurement of the elastic properties of the solid material in shale significantly (Fjær et al., 2008).

Clay minerals are naturally occurring material, which are chemically composed of silica, alumina and water, as well as iron, magnesium, sodium and potassium (Chen, 2015). The mineralogical composition of the clay phase varies widely with shale type. The most common clay minerals present include illite, smectite and kaolinite. Clay minerals are chemically composed of two types of mineral configurations; tetrahedral sheets and octahedral sheets, as shown in Figure 2- 2 and Figure 2- 3 respectively (Chen, 2015).

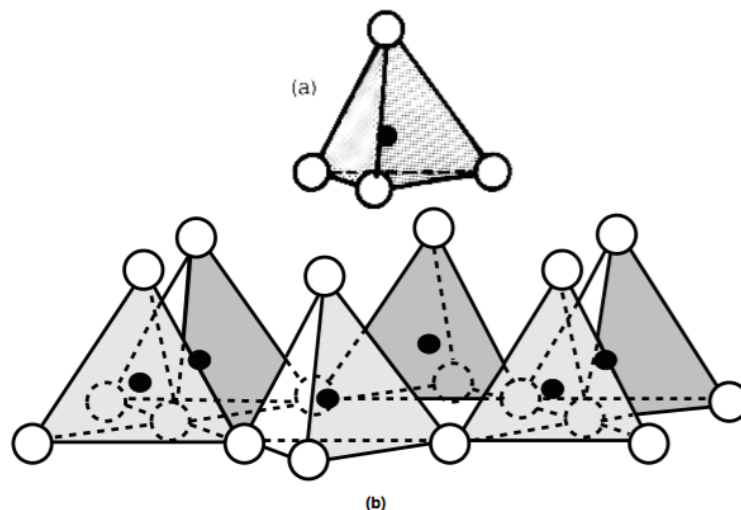


Figure 2- 2 (a) Silicon tetrahedral (b) Tetrahedral sheet (Chen, 2015)

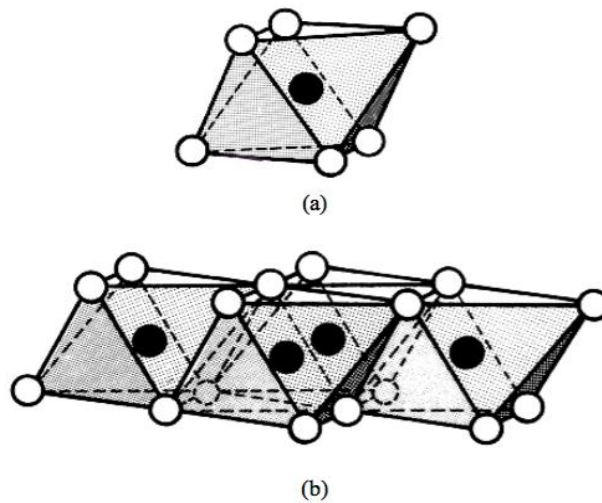


Figure 2- 3 (a) Octahedral formed by aluminium or magnesium (b) Octahedral Sheet (Chen, 2015)

Due to the presence of clay minerals and their special platelet structure, there is a high risk of clay hydration in shale. Clay hydration, or swelling, is the adsorption of water that results in an increase in clay surface volume (Chen, 2015). This is explained by the negative surface charge on the clay platelets, which attracts the dipolar water molecules, as illustrated in Figure 2- 4.

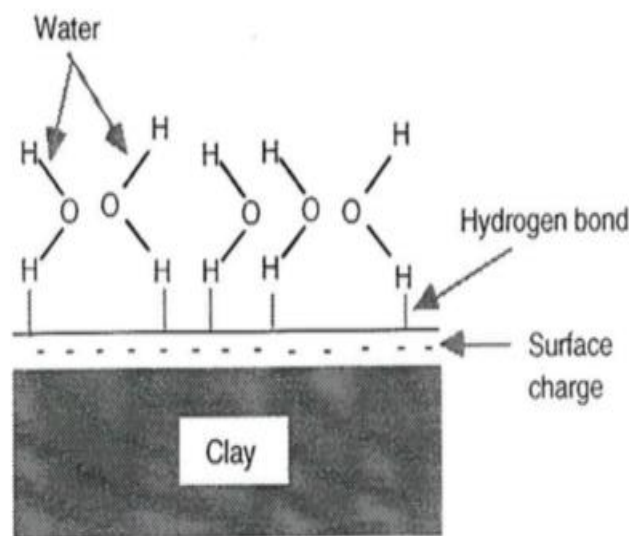


Figure 2- 4 Hydrogen bonding on the solid surface (Chen, 2015)

The swelling mechanism occurs when too much water is forced into the shale interlayers, and the geochemical reactivity of the shale depends largely on the amount of swelling clay minerals present. The most common swelling clay mineral is smectite, as this take much greater volumes than any other clays. In some cases, brines (e.g. potassium chloride, KCl), are used to avoid swelling clays (Chen, 2015). The most common shale types and their main properties are presented in Table 2- 1.

Major Shale Types	Main properties
Smectitic shales	Very high reactivity High porosity (>15%) Ductile Low hydraulic conductivity High specific surface Shallower depths (due to uplift), Depth < 3500 m High degree of diagenesis
Quartzite illite shales	Low reactivity Brittle Intermediate hydraulic conductivity Low specific surface Various depths Variable degrees of diagenesis
Organic shales	Variable reactivity Highly ductile Low hydraulic conductivity

Table 2- 1 Shale types and their main properties (Fam & Dusseault, 1998)

The texture of shale is also strongly anisotropic, which alters both the elastic properties and the strength of the shale (Fjær et al., 2008). A rock is anisotropic if the elastic response of a material is dependent of the material's orientation for a given stress configuration (Fjær et al., 2008). The anisotropy in shale can be observed through a plane of weakness, where the rock can easily be split. In practice, the anisotropic property of shale is often neglected in practical rock mechanical analysis due to lack of data, which can possibly be a source of uncertainty.

Shale is a special rock to study due to its low permeability. This means that performing rock mechanical tests is very time-consuming, since the process of achieving pore pressure equilibrium is slow. These rock tests are therefore costly, because such tests require cores extracted from drilling. These cores can easily be damaged by tensile failure during core retrieval (Fjær et al., 2008). Additionally, the cores have to be carefully preserved, as they can easily be damaged by desiccation. Table 2- 2 is a summary of the typical mechanical and petrophysical properties of shale.

Property	Typical Value	Unit
Porosity	> 1 - 70	%
Permeability	1-100	nD
Pore size	5 – 25	nm
Density	2300 - 2800	kg/m ³
Young's modulus	0.4 - 70	GPa
Poisson's ratio	0 - 0.30	-
Unconfined compressive strength (C _o)	2 - 250	MPa
Friction angle	10 – 20	°
P-wave velocity	1.6 - 4.5	km/s

Table 2- 2 Common shale properties (Fjær et al., 2008)

2.3 Pierre Shale Characteristics

The shale that will be tested in this study is the Pierre shale. Pierre shale is a geologic formation in the Upper Cretaceous period that occurs in the east of the Rocky Mountains in the Great Plains in the United States (US). This formation spans a large geographical area, stretching from Pembina Valley in Canada to New Mexico in the US. The formation is of marine environment deposits, which can be found near the surface and outcrops (Fooks & Dusseault, 1996). This shale has the characteristics of a typical shale appearance, with its dark grey colour and visible laminations. It is also relatively uniform in moisture content, mineralogy, grain size and bedding thickness.

The Pierre shale is not buried too deeply, which makes it much easier to recover in large amounts compared to other offshore shales (Fooks & Dusseault, 1996). Despite the shallow burial, the mineralogy of the Pierre shale is still similar to the shales found in deep offshore drilling. The Pierre shale is therefore a suitable rock to use in laboratory testing. The common Pierre shale properties are listed in Table 2- 3.

Property	Typical Value	Unit
Density	2370 - 2390	kg/m ³
Young's modulus	0.77 - 1.12	GPa
Poisson's ratio	0.35 - 0.37	-
Unconfined compressive strength (C _o)	7.5 - 13.9	MPa
P-wave velocity	2.5 - 2.2	km/s

Table 2- 3 Common Pierre shale properties (Fjær et al., 2008)

At the SINTEF Petroleum Physics Laboratory the Pierre shale is available in different batches. The proposed study will use Pierre shale samples from batch ML-346_2 and ML-223_3, where the mineralogical composition is mainly of quartz, chlorite, illite, and smectite. Shales that are rich in the brittle mineral, quartz, will have higher Young's modulus that gives stiffer rock (Morsy, Hetherington, & Sheng, 2013). Young's modulus is a measure of the stiffness of the rock, i.e. the rock's resistance to compression by a uniaxial stress (Fjær et al., 2008). The mechanical properties of shale vary as a function of mineralogy, and the details of the mineralogy obtained from fine analysis at SINTEF Petroleum can be found in Appendix E (Table E- 3).

For all experiments, small 15-mm disk-shaped samples of Pierre shale will be used. The samples are prepared by cutting the core plugs into thin slices. This will be described in detail in *Chapter 4*.

3 Relevant Background Theory

The time-dependent behaviour of rock materials is one of the fundamental mechanical properties of rocks. Shale layers may interact with reservoir fluids, and thereby deform in a time-dependent manner. This section covers therefore an introduction to rock mechanics and the relevant theoretical background for a proper understanding of the creep behaviour.

3.1 Failure Mechanics

An introduction to the basic concepts in failure mechanics is essential in understanding the rock strength and the time-dependent effects of shale. Rock failure implies that the rock can change its shape permanently when subjected to sufficiently large stresses, and eventually fails and falls apart. The stress level that the rock typically fails is referred as the rock strength.

The concept of rock failure is associated with the solid framework of the rock. The stress causing the failure are the effective stresses experienced by the framework (Fjær et al., 2008). The effective stress is carried by the external stress of the solid framework and the fluid inside. The orientation of the failure is dependent on the plane of weakness of the rock. Rock failure is still regarded as a complex process, and various failure mechanisms are identified to describe the rock failure behaviour through tensile failure, shear failure and compaction failure.

3.1.1 Tensile Failure

Tensile failure occurs when the effective tensile stress across a plane in the rock exceeds the critical limit of tensile strength (T_0). The tensile strength is a characteristic property of a rock. The failure criterion specifies the stress condition at which the failure will occur, and identifies the location of the failure surface at the principal stress (σ'), which is given as (Fjær et al., 2008);

$$\sigma' = -T_0 \quad 3-1$$

Most sedimentary rocks have a relatively low tensile strength, and the tensile failure tends to occur along pre-existing cracks. Tensile fractures typically orient normal to the direction of the tensile stress, as illustrated in Figure 3- 1.



Figure 3-1 Tensile failure (Fjær et al., 2008)

3.1.2 Shear Failure

Shear failure initiates when the shear stress along a plane in the rock is sufficiently high. A fault zone will eventually develop along the failure plane, where the two sides of the plane will move relatively to each other that causes a frictional process, as illustrated in Figure 3- 2.



Figure 3- 2 Shear failure (Fjær et al., 2008)

The extent of the frictional force caused by the movement is dependent on the force that pushes the bodies together. The critical shear stress (τ_{max}) is the point where shear failure occurs, which is dependent on the normal stress (σ') acting over the failure plane (Fjær et al., 2008);

$$|\tau_{max}| = f(\sigma') \quad 3- 2$$

This is known as Mohr's hypothesis, where the pure shear failure depends only on the maximum (σ_1) and minimum (σ_3) principal stresses, and not on the intermediate stress (σ_2)

(Fjær et al., 2008). By choosing specific parameters of the function $f(\sigma')$ of Eq. 3- 2, different shear failure criteria are obtained. The simplest form is called the Tresca criterion, where the frictional force is neglected;

$$\tau_{max} = \frac{1}{2}(\sigma'_1 - \sigma'_3) = S_o \quad 3- 3$$

where S_o is the inherent shear strength of the material, also known as cohesion. A more general and commonly used failure criterion is the Mohr-Coulomb criterion, which assumes that $f(\sigma')$ is a linear function of σ' (Fjær et al., 2008);

$$|\tau_{max}| = S_o + \mu\sigma' \quad 3- 4$$

where μ is the coefficient of internal friction. The Mohr-Coulomb can be simplified and rewritten in terms of the maximum principal stress;

$$\sigma'_1 = C_o + \sigma'_3 \tan^2 \beta \quad 3- 5$$

where β is the failure angle and gives the orientation of the failure plane. β is given as;

$$\beta = \frac{\pi}{4} + \frac{\varphi}{2} \quad 3- 6$$

where φ is the frictional angle. The unconfined compressional strength, C_o or UCS, is also a function of β ;

$$C_o = 2S_o \tan \beta \quad 3- 7$$

Figure 3- 3 illustrates the Mohr-Coulomb circle corresponding to a critical stress state. The straight line represents the Coulomb failure envelope, which crosses the shear stress axis at the cohesion point S_o . The straight line separates a “safe region” from a critical failure envelope, thus shear failure occurs when the Mohr circle touches the failure envelope.

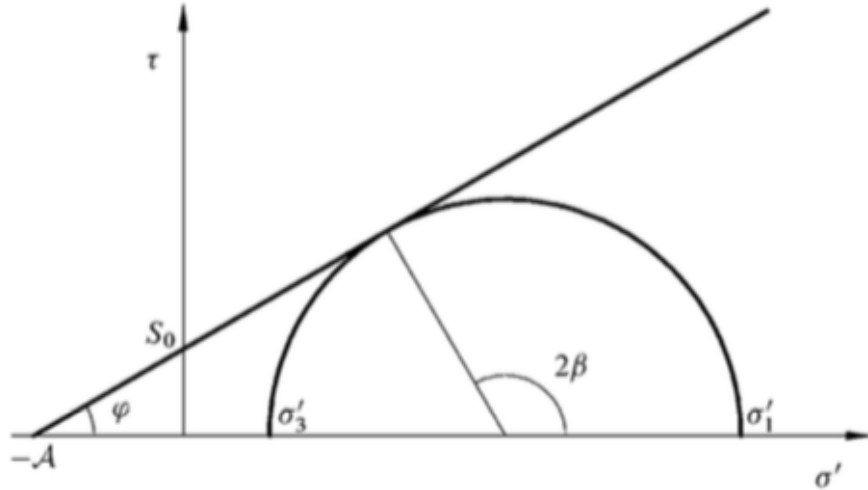


Figure 3-3 Mohr-Coulomb criterion in shear-normal stress plane (Stenebråten et. al., 2008)

Cohesion S_0 is a component of the shear strength of a rock, which can be estimated from the peak stress σ_{peak} with the relationship;

$$S_0 = \frac{\sigma_{peak}}{\cos(\varphi)} \quad 3- 8$$

The peak stress σ_{peak} is found by dividing the maximum force by the area of the shear surface. The friction angle φ can be obtained from the failure angle β in Eq. 3- 6.

Cohesion can also be estimated from the P-wave velocity of the rock. The correlations relating the P-wave velocity, UCS (C_o) and failure angle are defined by (Horsrud, 2001);

$$C_o = 0.77 \cdot V_p^{2.93} \quad 3- 9$$

$$\beta = 49.8^\circ + 0.3 \cdot C_o \quad 3- 10$$

$$\beta = 39.9^\circ + 5.5 \cdot V_p \quad 3- 11$$

Using the correlations above for UCS and β , the cohesion can then be estimated with;

$$S_o = \frac{C_o}{2\tan(\beta)} \quad 3- 12$$

3.1.3 Compaction Failure

Compaction failure is a response to pore collapse. This failure mode is commonly observed in high porosity materials, where the grain skeleton forms an open structure. Compaction results in a closer packing of the rock, illustrated in Figure 3- 4.

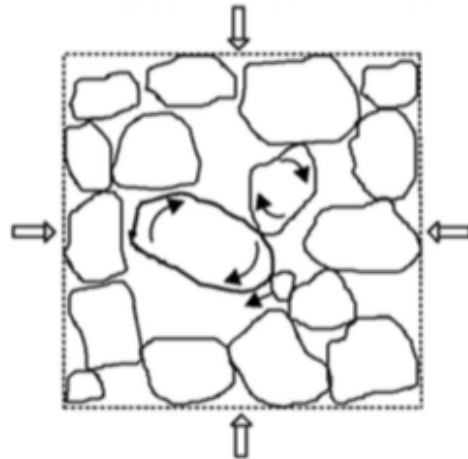


Figure 3- 4 Grain orientation due to closer packing (Fjær et al., 2008)

Pore collapse may be caused by hydrostatic loading, and failure occurs due to local excessive shear forces acting through grains and the contact areas. If the stresses are sufficiently high, the grains may be split up due to grain crushing.

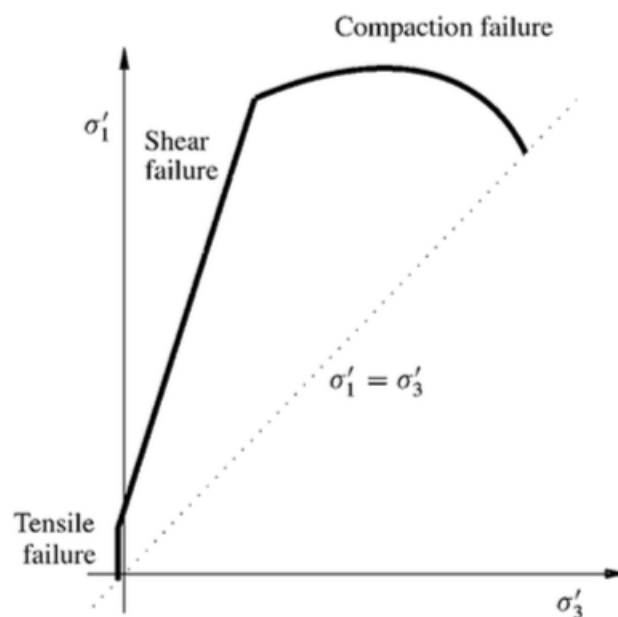


Figure 3- 5 Location of failure modes in principal stress space for tensile, shear and compaction failure (Fjær et al., 2008)

Figure 3- 5 is a schematic of the location of tensile, shear and compaction failure modes in a principal stress space, assuming that the intermediate principal stress (σ_2') is equal to the maximum principal stress (σ_3'). For real rocks, the transition between the different failure modes is smoother than shown in the figure.

3.2 Time-Dependent Deformation in Shale

3.2.1 Introduction to Creep

Time-delayed deformation in rocks is a slow moving process that can possibly deform the rock permanently under the influence of mechanical stresses. This is a phenomenon that can be found in both laboratory tests and in the field, but the timescale can be very different (Fjær et al., 2014). In fact, the deformation of rocks can even continue for a long time after a change of stress state has occurred (Fjær et al., 2008). This effect can possibly complicate the interpretation of the laboratory tests, and raises uncertainty when the laboratory results are applied in the field. There are basically two different explanations for this time-dependent effect; consolidation and creep.

Creep is a time-dependent process that occurs in rock materials under constant stress. Consolidation occurs because of pore pressure diffusion, whereas creep originates from viscoelastic properties in the solid framework (Fjær et al., 2008). Consolidation and creep are often discussed separately, but this in practice is sometimes difficult to distinguish between genuine creep and consolidation effects. However, this study concentrates only on the creep behaviour. Creep deformation occurs in rocks when subjected to constant stress, being highly sensitive to both stress and temperature. Unlike consolidation, creep can occur both in dry and saturated rocks (Fjær et al., 2008).

The viscoelastic effect can be explained by two physical properties; viscosity and elasticity (Meyers & Chawla, 1999). The viscous part is due to the material's ability to resist both shear flow and strain force linearly with time. While the elastic effect enables the material to return to its original state upon stress relief. Figure 3- 6(a) shows the behaviour of an elastic material in a stress-strain curve, where the material's deformation will return to its original state after stress relief. Figure 3- 6(b) shows the path changes when the material behaves viscoelastically. The red area in (b) illustrates the amount of energy that is lost in a loading and unloading cycle (Meyers & Chawla, 1999).

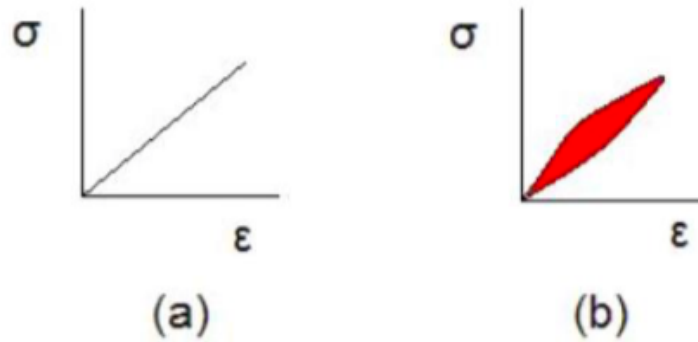


Figure 3- 6 Stress-strain Curve (a) For an elastic material (b) For an viscoelastic material (Meyers & Chawla, 1999)

The rate of creep deformation is time-dependent, where the time-scale is divided into three stages. The stages may change completely, from a time limited process with small amplitude (transient creep) to a seemingly perpetual process (steady state creep), and eventually to a rapid process ending in failure (accelerating creep). The rate of deformation, also known as creep rate, depends on a number of factors including material properties, exposure time, exposure temperature, pore fluid chemistry, sediment composition, porosity and grain size as well as loading conditions.

3.2.2 Stages of Creep

The nature of creep is categorized into three distinct stages. Figure 3- 7 shows a characteristic S-curve for a rock material that undergoes all three stages of creep under constant stress.

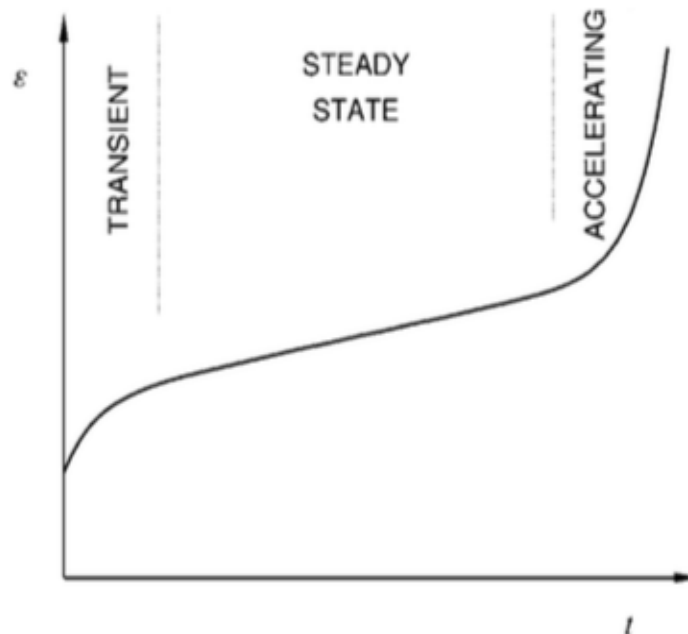


Figure 3- 7 Characteristic strain response for rock materials under constant stress, showing transient, steady state and accelerating creep (Fjær et al., 2008)

At the transient (primary) stage, the rate of deformation *decreases* as a function of time. If the applied stress is low, the deformation rate will finally converge to zero and the creep process will eventually end. If the transient creep process ends, the deformation will not continue to phase into the two other stages. During the transient period, the creep mechanism induces the formation and spreading of micro-fractures at a decaying rate. Moreover, the rock tends to behave elastically during this period. These properties enable the rock to return to its original state upon stress relief.

The next stage has a *constant* deformation rate. If the applied stress is sufficient, the creep process will progress from transient creep into the steady state (secondary) regime. Steady state creep implies a permanent deformation of the material. Unlike transient stage, the rock will not be able to return to its original state once steady state creep has occurred, thus behaving inelastically.

If the applied stress continues to increase and subjected for long enough period of time, the deformation rate will finally converge to the accelerating (tertiary) creep. This is the stage where the deformation rate *increases* with time. The process is associated with a rapid spreading of unstable fractures, and the rock will eventually fail. Figure 3- 8 is a illustration of how creep responses to different values of the applied stress.

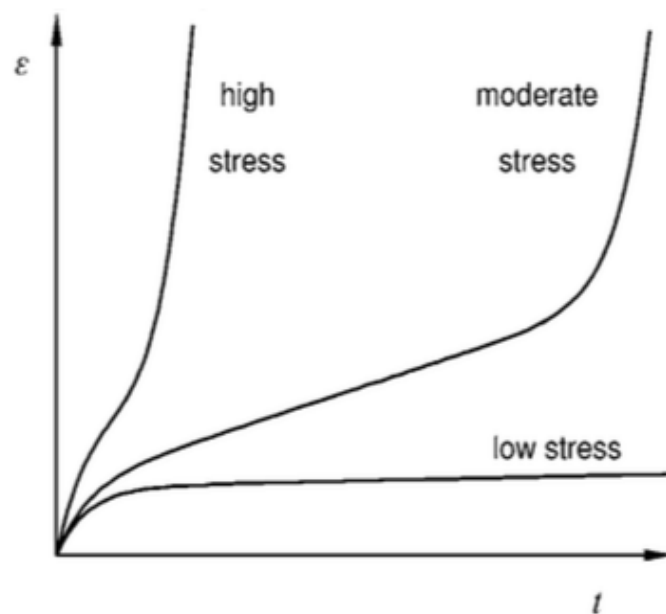


Figure 3- 8 Creep response to different values of applied stress (Fjær et al., 2008)

3.2.3 Internal Processes Causing Creep in Shale

In quartz rich minerals, grain scale processes are likely to occur. These are due to brittle behaviour, frictional mechanisms of intergranular slip, grain rearrangement, pore collapse, micro-fractures, grain crushing, and time and temperature exposure to subcritical crack growth (Chester, Lenz, Chester, & Lang, 2004).

Fractures are commonly caused by stress exceeding the rock strength. At this stress level, the rock tend to loose its cohesion along its weakest plane, and fractures will be formed (Park, 2005). Fracture surfaces are rough and can be connected to each other (Fjær et al., 2008). On the other hand, a crack is an open void of a given idealized shape, which acts as a local discontinuity (Fjær et al., 2008). Cracks are a fracture mechanism that commonly occurs in brittle formations. Subcritical crack growth occurs when the fluids within the fracture can initiate a fracture propagation with a much lower pressure than initially required (Van Der Pluijm & Marshak, 2004). Some fluids may react with the minerals in the rock to compose a lower stress limit required for fracturing.

Creep is often associated with crack growth. Crack propagation can be related to the three distinct creep stages, where transient creep is often referred to as subcritical crack growth (Atkinson, 1982). Cracks can occur in all types of rocks and have a large impact on the elastic properties of the material (Fjær et al., 2008). Atkinson (1982) suggests that crack growth is caused by tensile stress, referred as Mode I of fracture propagation. Here, it is identified that there are four micro-mechanisms that explain the crack growth that lead to fracturing of materials that cleave.

The first mechanism involves the propagation of pre-existing cracks. A crack in a brittle rock is able to propagate at lower stresses than what is required for slip or twinning on any crystallographic system. Fracture occurs at a stress σ_f given by (Atkinson, 1982);

$$\sigma_f \cong \left(\frac{EG_c}{\pi c} \right)^{\frac{1}{2}} \quad 3-13$$

where E is Young's modulus, c is the pre-existing crack length and G_c is the critical strain energy release rate for plane strain ($G_c = K_I^2(1 - \nu^2)/E$, ν : poisson's ratio) and K_I is the tensile stress intensity factor.

The second mechanism involves fracture controlled by cracks generated through microplasticity. If the pre-existing cracks are very small or not present, the stress level can build up to a certain level to initiate slip. This occurs when slip dislocations pile up at grain boundaries. These cracks have a length, which is proportional to the grain size, d , since this is the wavelength of the internal stresses. If the stresses exceed σ^* , given as;

$$\sigma^* \cong \left(\frac{EG_c}{\pi d} \right)^{\frac{1}{2}} \quad 3-14$$

then a crack will propagate as soon as it is formed, according to the stress for the onset of microplasticity, σ_y . If, however, σ^* exceeds σ_y , then a crack initiated by slip will not propagate immediately. At this stage, the stress has to be increased even further before macroscopic fracture occurs (Atkinson, 1982).

The third mechanism is fracture controlled by cracks generated through general plasticity/grain boundary sliding. This type of fractures is caused by large deformation through plastic strain, where the process itself is initiated by an increase in temperature. The increase in temperature decreases the flow stress, which leads to plastic flow and creep. Due to plasticity, the pre-existing faults are less sharp with stronger resistance to further fracturing (Atkinson, 1982).

The last fracture propagating mechanism is intergranular creep fracture. This is failure under high temperatures and low stresses. Voids or wedge cracks tend to merge and grow on grain boundaries, also known as crack nucleation. The nucleation¹ tends to be controlled by dislocation creep, but when the cracks are small, growth is mainly controlled by local diffusion (Atkinson, 1982).

Creep crack growth undergoes also three stages like it does for creep processes (Zhao & Roegiers, 1995). At the primary stage cracks tend to be open, but do not propagate. Stable crack growth occurs eventually at the secondary stage, while unstable crack propagation happens at the third stage. The occurrence of active micro-cracks may influence the stability of the internal structure during the first two stages due to strain-hardening (Zhao & Roegiers, 1995). When the crack density reaches a certain critical value, the weakened region will be formed around the crack tip due to strain-softening, resulting macroscopic fractures. It is important to account for the development of this phenomenon, as the rocks that are loaded below failure strength can still undergo permanent and time-dependent deformation (Zhao & Roegiers, 1995).

¹ Crack nucleation is the initial process, where sufficient quantity of dislocations accumulates to allow separation of crystal planes (Atkinson, 1982)

3.2.4 Distinguishing Between Consolidation and Creep

Consolidation is considered as a transient process as it involves equilibrating the pore pressure after a change in stress state (Fjær et al., 2008). This occurs through viscous flow of pore fluid through the porous rock. The process follows Darcy's law, which states that the volume per unit time flowing (\vec{Q}) through a surface A is proportional to the pore pressure gradient ∇p_f (Fjær et al., 2008). Darcy's law is defined as;

$$\vec{Q} = -A \frac{k}{\eta_f} \nabla p_f \quad 3-15$$

where k is the permeability of the rock and η_f is the dynamic viscosity of the fluid. Eq. 3-15 describes stationary fluid flow in a homogeneous pore pressure gradient field.

Unlike creep, consolidation can only occur in saturated rocks. If a porous media is exposed to external forces, it will alter the pore pressure equilibrium and result to a change in stress distribution in the material. This will initiate a compression and fluid flow within the pores during deformation (Kleien & Lund, 2015). For a saturated rock, the effective stress of the solid material will increase with decreasing pore pressure (Kleien & Lund, 2015). This is explained by the fact that pore pressure will counteract the effect of the external forces, and the applied stress will gradually force the fluid out of the pores until a new equilibrium is established, thus a decrease of pore pressure is seen.

3.2.5 Thermoelasticity

Rocks, like most other materials, expand or shrink when there is a change in temperature. Temperature is suggested to have a significant impact on creep. Traditionally, the temperature effects on rock strength is explained by the transition from the brittle region to the plastic regime. The minerals in the rocks tend to become more plastic as the temperature increases, which compromises the load bearing capacity and thus reduces the rock strength of the material (Hallberg, 2011). Figure 3-9 shows how temperature is related to stress and strain.

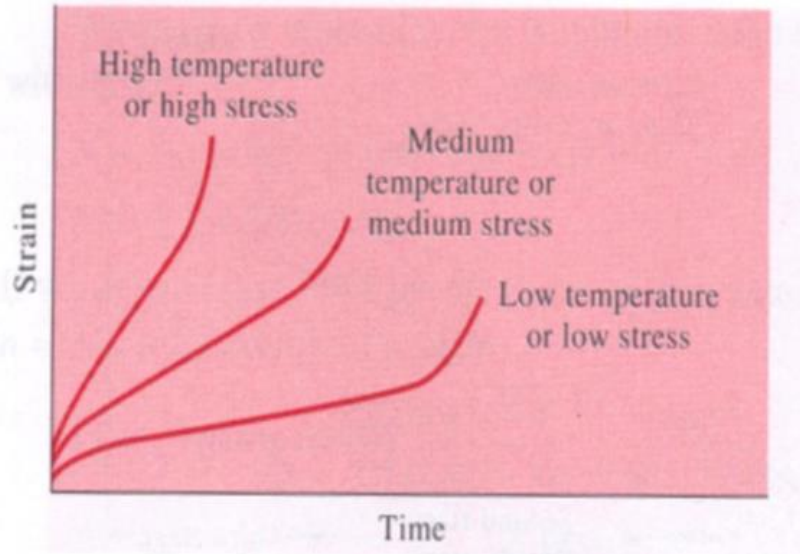


Figure 3- 9 Relationship between temperature and stress (Dowling, 2007)

If there is a temperature difference between the rock's initial temperature and the fluid outside the rock, this temperature difference will propagate by diffusion from the surface and into the rock (Fjær et al, 2002). The thermally induced axial strain, resulting from a change in temperature, is given by (Fjær et al., 2008);

$$\varepsilon_a = -\alpha_T(T - T_0) \quad 3- 16$$

where α_T is the coefficient of linear thermal expansion, T_0 is the initial temperature and T is the final temperature. The minus sign of the equation ensures that α_T is positive, where a temperature increase gives an expansion. The value of the coefficient is different for every type of rock.

3.2.6 Chemical Effects of Pore Fluid

Knowing that the mechanical properties of shales tend to be sensitive to exposed fluids, quantification of such effects is important. The minerals in the rock may react chemically with the pore fluid. Especially clay minerals can become soft or even dissolve in water, which implies that fluid substitution may totally change the framework moduli (Bulk and shear modulus). Both water and ions can diffuse into or out of the shale. Any changes in mechanical properties of the shale are therefore induced by microscopic physical-chemical interactions.

The pore fluid in the shale has chemical activity (a_{sh}) defined by the type and amount of dissolved ions. If the rock surface is exposed to another fluid with a different chemical activity (a_f), the water molecules can either enter or leave the shale to compensate for this disturbance (Fjær et al, 2002). The disturbance (Δp) in pore pressure at the surface is thus given by (Fjær et al, 2002);

$$\Delta p = c_o T_f \ln \frac{a_f}{a_{sh}} \quad 3-17$$

where T_f is the formation temperature and c_o is the relative pressure amplitude.

This disturbance can be positive or negative, depending on whether the activity of the fluid is larger or smaller than the activity of the shale. If the activity of the fluid is less than the activity of the shale, the disturbance in pore pressure will be negative, which is preferred in terms of borehole stability (Fjær et al, 2002).

The rock surface may act as a perfect membrane, that is a membrane that allows only water molecules to pass. If not, the ions will move through the surface and gradually shift the activity of the shale towards the activity of the drilling fluid (Fjær et al, 2002). After a while, the pore pressure shift is reduced to $\sigma \Delta p$, where σ is the membrane efficiency. The time scale for the effect of chemical activity is controlled by pore pressure diffusion, while the time scale for relaxation of fluid in the shale is controlled by ion diffusion. The ion diffusion process is usually much slower than pore pressure diffusion.

It is found that some ions are more effective in reducing the hydration diameter of the clay platelets in the shale structure, which causes the shale to shrink (Chen, 2015). The ions that can effectively minimize the swelling process are able to penetrate the clay lattices due to their small sizes. The clay lattices will then be tightly fixed by the attractive forces, which result in binding the clay sheets closer together that reduces the tendency of the clay to hydrate. This is illustrated in Figure 3- 10.

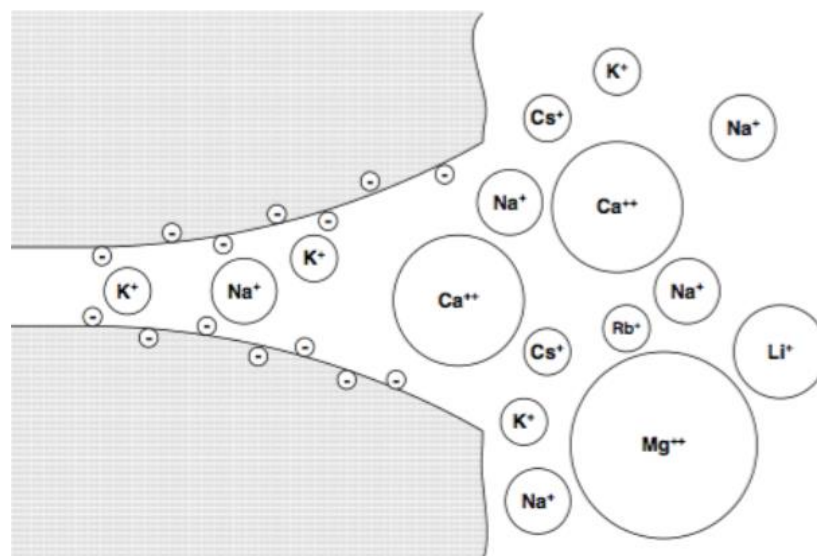


Figure 3- 10 K^+ ion and Na^+ ions are more effective than Ca^{2+} ion in reducing clay hydration due to their small sizes (Chen, 2015)

The degree at which the ion exchange is expected to take place is dependent on ion concentration in the pore fluid of the shale. The ion exchange process is considered to be much faster than the ordinary ion diffusion process that brings the ions into the shale. Ion diffusion is therefore the process that will effectively control the time scale for the total process (Fjær et al, 2002).

The deformation of shale is therefore directly related to a chemically induced strain caused by temperature difference and ion exchange processes (Fjær et al, 2002). The shale deformation caused by a contrast in chemical activity is an elastic response to the change in effective stress by a shift in pore pressure.

3.3 Acoustic Waves

3.3.1 Wave Propagation in Rocks

Acoustic waves are oscillating disturbances propagating through a material (Fjær et al., 2008). The velocity of the propagating waves is a function of the elastic stiffness and the density of the rock. These parameters also depend on other rock mechanical parameters such as porosity, permeability and etc. Acoustic velocities can therefore provide valuable source of information on formation properties due to the interaction between the propagating wave and the medium it travels through (Nes et al., 1996). Acoustic measurement techniques have also proven to be an excellent tool to monitor fluid-shale interaction, particularly ionic diffusion (Holt et al., 1996). Change in velocity measurements resulting from fluid exposure may be indicative of changes in the mechanical properties in the rock.

Generally, acoustic waves can be used to evaluate the difference between static and dynamic moduli (explained in *section 3.5.5 p. 26*), provide correlations in rock strength and estimate the *in situ* stress states.

3.3.2 P-waves

Primary or pressure waves, also known as P-waves, are periodic compressions of a material. The propagation of a P-wave is always longitudinal, which implies that the particles in the rock vibrate along the direction of the motion (parallel) of the wave energy. The velocity for P-waves in a linearly elastic, homogenous and isotropic rock is given by;

$$v_p = \sqrt{\frac{K + \frac{4}{3}G}{\rho}} \quad 3- 18$$

where K is the bulk modulus, G is the shear modulus and ρ is the fluid density. This expression can also be rewritten in terms of Young's Modulus (E) and Poisson's ratio (ν), by using elastic moduli relations;

$$v_p = \sqrt{\frac{E(1-\nu)}{\rho(1-2\nu)(1+\nu)}} \quad 3- 19$$

Note that Eq. 3- 18 and Eq. 3- 19 are given in dynamic moduli, which may deviate from the static moduli.

However, note that most rocks do not show exactly linearly elastic, isotropic and homogenous behaviour (Fjær et al., 2008). Eq. 3- 18 is therefore only an approximation to real rocks, which eventually can complicate the relation between acoustic velocities and elastic moduli (Fjær et al., 2008). Table 3- 1 shows the typical P-wave velocities for weak shale from the North Sea and "regular" shale.

Rock Type	Density	P-Wave Velocity	Conditions
	[kg/m ³]	[km/s]	[-]
Shale	2300 – 2800	1.6 – 4.5	Saturated various porosities
Weak shale (North Sea)	1800 – 2300	2.4 – 2.6	Saturated confined

Table 3- 1 Common P-wave velocities for shale and weak shale from the North Sea (Fjær et al., 2008)

3.3.3 P-waves and Pore Fluid Exposure in Porous Materials

The elastic wave response may vary significantly with stress. The velocities will typically increase with increasing stress, but increasing anisotropic stresses may eventually either reduce or increase the velocities (Fjær E. , 2006). Moreover, the elasticity of a porous material may also be highly sensitive to the presence of a pore fluid. In poorly consolidated sediments, the P-wave velocity for a water saturated rock tend to be several times larger than a dry rock (Fjær et al., 2008). Qualitatively, the presence of pore fluid provides additionally resistance to compression. For materials under high confining pressure, the pore fluid contribution is reduced, while the stiffness of the rock is increased (Fjær et al., 2008). The effect of saturation is therefore much smaller. For a real stiff rock, the P-wave velocity will be reduced due to an increase in saturation (and thus density).

Micro-cracking is one of the processes causing creep, where cracks can cause a decrease in P-wave velocity (Zhao & Roegiers, 1995). This is explained by that a change in stress state implies that pores may either shrink or expand. This changes the porosity of the rock, which causes the cracks to open or close, thus resulting a change in crack densities. Such stress induced changes in the rock are the causes for the stress dependence in wave velocities (Fjær E. , 2006).

The reason for the decrease in P-wave velocity is believed to be linked to an increase in the crack density as a result of one or several of the processes mentioned in *section 3.2.3*. The increase in crack density results in a decrease in the effective Young's modulus, which follows the relation (Fjær et al., 2008);

$$E_{eff} = E(1 - \xi Q) = \frac{\sigma_z}{\varepsilon_z} \quad 3-20$$

where E is the Young's modulus of the material without cracks, ξ is the crack density and a function of the size and number of cracks and Q is a coefficient depending on the shape and orientation of the crack. Considering Figure 3- 11, the strain ε_x is increased as the stress is increased. The closure of the crack is a result of the strain increase and at a certain stress level σ_x^C the crack will be closed.

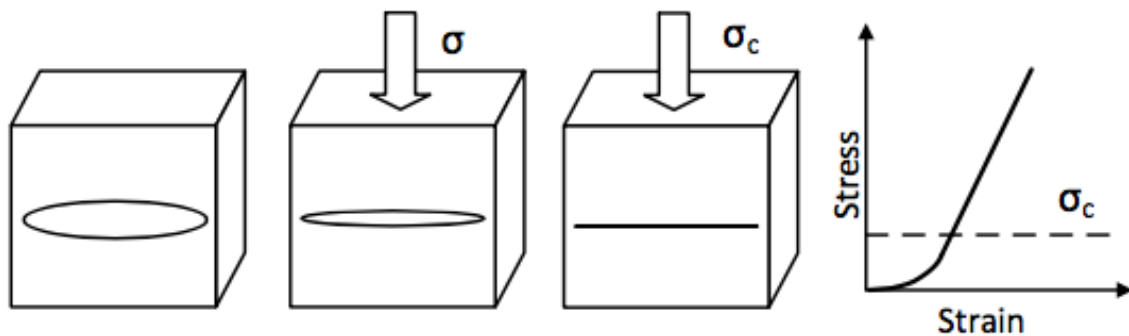


Figure 3- 11 - Left: A crack closing due to increasing stress. Right: Non-linear deformation caused by several cracks closing. (Stroisz & Fjær, 2011)

3.3.4 Temperature and Anisotropic Influence

An increase in temperature exposure gives normally a reduction in velocities (Fjær et al., 2008). This effect is particular high if the rock constituents undergo a phase transition within the actual temperature range, such as during freezing or melting of pore fluid. Bauer et al.'s (2014) study observed that thermally-induced compaction of shale is followed by a creep behaviour that is accompanied by an increase in acoustic velocities, indicating rock stiffening.

As pointed out earlier, shale is an anisotropic rock like most of the sedimentary rocks. Since shale is built up of many layers, the stiffness of each layer will vary with the directions, thus affecting the acoustic properties of the rock (Fjær et al., 2008). This can be accounted with a generalized version of the wave equations and its solutions, but this will not be presented here. The results can be found in Fjær et al. (2008) p. 189 Chapter 5.5.

3.3.5 Static and Dynamic Moduli

Acoustic waves provide means to estimate mechanical properties of rocks. This implies that there are links between the parameters describing elastic waves and the rock mechanical properties. Eq. 3- 19 shows that P-wave velocity depends explicitly on elastic moduli, and thus on cracks and densities as well.

The term *static moduli* is the elastic moduli obtained from stress and strain measurements in a rock mechanical test, while *dynamic moduli* is obtained from acoustic velocities and densities. Static moduli describe a rock's response to strain rates smaller than 10^{-2} s^{-1} with large amplitudes, while dynamic moduli measures response to rapid stress oscillations (typical range $1 - 10^4 \text{ s}^{-1}$) (Fjær et al., 2008). The major difference between static and dynamic measurements is therefore the strain amplitude. The static moduli measure the slopes of stress-strain curves, while the dynamic (elastic) is of small strain amplitude due to plasticity or non-linear effects. The amplitude is an important property in terms of rock behaviour, since small and dynamic amplitude oscillations do not have the ability to overcome the static frictional forces required to close a crack (Olsen, 2015).

However, a wide range of experimental evidence proves that static moduli deviate significantly from dynamic moduli, especially at lower stresses (Fjær et al., 2008). Normally, the dynamic moduli have higher values than the corresponding static ones. The difference is highest for weak rocks, and decreases with increasing confinement. One possible reason explaining the discrepancy between static and dynamic moduli in rocks is the presence of pore fluid (Fjær et al., 2008). During a velocity measurement, the deformation of the rock is undrained, which implies that there is a pore fluid contribution to the velocity. The dynamic moduli derived from

velocity measurements on a saturated rock are therefore slightly higher than the corresponding static moduli from a drained test (Fjær et al., 2008).

Continuing on explaining the static-dynamic discrepancy, the source of this deviation seems to be related to the heterogeneous microstructure of the rocks (Fjær et al., 2008). It is also expected that much of this effect lies at the grain boundaries, because the stress concentrations in the contact areas may exceed the elasticity limit of the material. Fjær (1999) has therefore established a quantitative model that derives the relation between static and dynamic moduli;

$$K_{static} = \frac{K_{dynamic}}{1 + (P_z + 2P_r)K_{dynamic}} \quad 3- 21$$

$$E_{static} = \frac{E_{dynamic}}{1 + P_z E_{dynamic}} (1 - F) \quad 3- 22$$

where $K_{dynamic}$ and $E_{dynamic}$ are the bulk modulus and Young's modulus respectively obtained from velocity measurements, and K_{static} and E_{static} are the corresponding moduli obtained from the slope of the relevant stress-strain curve during initial loading. The difference between static and dynamic moduli is expressed by the parameters P_i and F . The physical meaning of P_i is predominantly a measure of a process involving crushing of asperities at the grain boundaries, while F is associated with the friction occurring due to sliding along contact points or closed micro-cracks in the material during shear loading (Fjær E, 1999). Thus, the discrepancy between static and dynamic moduli in weak rocks is suggested to be caused by a series of local failure processes on a microscopic scale during a loading sequence.

4 Experimental Setups and Procedures

4.1 Purpose

The purpose of the experiments is to investigate the creep behaviour of small shale samples. This is done by examining the rock strength using the shale puncher tool with two different loading paths. The first study involves standard creep tests through a stepwise loading path, while the second one considers strain-rate tests with a continuous loading path. P-wave velocities will also be measured in order to quantify the sample heterogeneities.

Additionally, the chemical effects will also be studied by saturating the samples with only oil, brine or hydrochloric acid. Brine is used to study whether this will provide a chemical effect on the rock strength, while hydrochloric acid also will investigate the effect of pH.

4.2 Equipment Principles

4.2.1 Continuous Wave Technique

One of the techniques developed in the purpose of estimating mechanical properties of rocks from velocities is the Continuous Wave Technique (CWT). CWT is a method used for measuring the acoustic velocities, particularly well-suited for testing of small mm-thick disk-shaped samples (Nes et al., 1996). Potential applications are within estimation of mechanical properties of shales, effects of various drilling fluids, estimation of seismic parameters and pore pressure. Cohesion is one of the mechanical property that can be calculated from the measured velocity, which can provide information about the rock strength (Stenebråten et al., 2008). Performing acoustic measurements on small samples generally yields access to more material, allowing a larger variety of experimental measurements and parameters. CWT is a non-destructive technique, which allows the use of the same samples for other purposes (Stenebråten et al., 2008). Thus, the same samples can be used in strength testing after the acoustic measurements.

The system is based on a simple CW transmission spectrometer that clamps the sample with oppositely mounted acoustic transducers, thus constituting a composite resonator (Stenebråten et al, 2008). One transducer generates acoustic waves, while the other one detects the signal. The ultrasonic standing wave resonance in the composite resonator is generated by sweeping the excitation frequency of a range of several corresponding standing wave resonances.

4.2.2 Shale Puncher Tool

The shale puncher is a compact tool developed for testing the mechanical strength of small shale samples. Traditionally, this type of testing is usually done on shale cores, which is expensive and time-consuming. Such tests have to be run very slowly due to the low permeability in shale (Stenebråten et al., 2008). In contrast, testing on small samples can be run much faster, as the time needed to obtain pore pressure equilibrium is significantly reduced (Stenebråten et al., 2008).

The test involves punching a hole through a prepared disk-shaped sample with various stress loading path. The strength of the sample can be estimated from the peak force required to make the hole. This can be done by rearranging Eq. 3- 6 in terms of the friction angle, ϕ , and then calculate the cohesion by using Eq. 3- 8.

The puncher tool involves a pure shear test, where the changes in volume and pore pressure gradients are minimal. This combined with the use of small samples, the tests can be run very quickly compared to standard tests. The tool is therefore designed to achieve fast and inexpensive testing.

The shale puncher tool is a mechanical device containing two clamping pistons, two punching pistons and two locknuts (Stenebråten et al., 2008). The clamping pistons are made of stainless steel, the punching pistons of hardened tool steel to minimize wear on the piston surfaces and the locknuts are made from brass so avoid seizure of the pistons and the locknuts. Figure 4- 1 is a drawing of the parts making up the puncher tool.

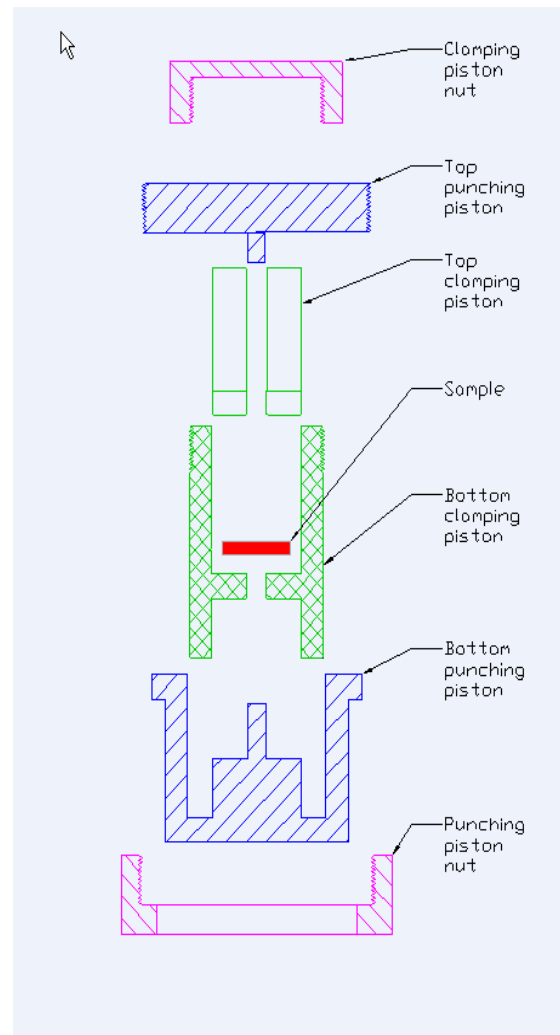


Figure 4- 1 Drawing showing the parts making up to the puncher tool (Stenebråten et al., 2008)

The tool design enables the disk-shaped shale sample to be held between the two clamping pistons, where each clamping piston has a centered hole to fit a punching piston from each side of the sample. The clamping pistons and the punching pistons are locked together in pairs by the locknuts. The test emphasizes on applying an axial force on the punching tool, which creates a shearing force that exerts on the sample as the clamping pistons and the punching pistons are forced in opposite directions. Figure 4- 2 is a drawing showing the entire assembled tool.

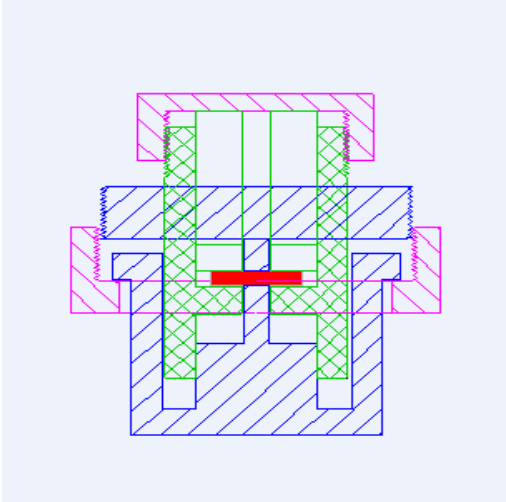


Figure 4- 2 Drawing showing the assembled puncher tool (Stenebråten et al., 2008)

The creep tests performed with the puncher tool differs from the standard creep tests. The location of the failure region is predetermined in a punch test, where a hole is aimed to specifically punch through the sample. This means that the puncher test determines the failure region from the geometry of the tool, whereas failure in a standard tri-axial compressions test follows the weakest zone along the failure plane on the rock. Figure 4- 3 shows graphically the difference in failure region of a standard tri-axial axial compression test and the puncher tool.

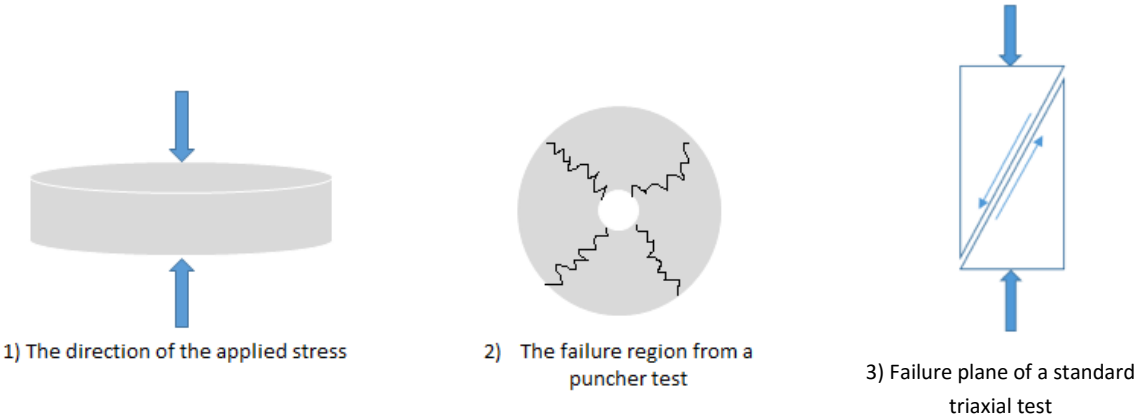


Figure 4- 3 Drawing showing the difference in failure region of a puncher test and a standard tri-axial compression

4.2.3 Loading Paths

Two types of test will be run on the shale puncher tool to study the creep properties in shale; standard creep tests and strain-rate tests. Figure 4- 4 illustrates the difference in loading paths with strain as a function of stress.

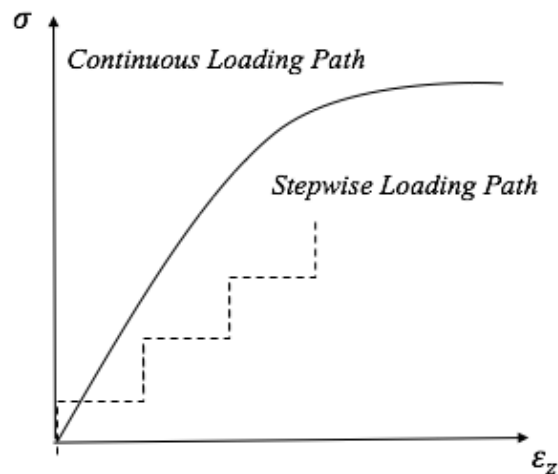


Figure 4- 4 Sketch of stress paths; continuous and stepwise

The creep tests will be run with a stepwise loading path, which implicates that the sample is loaded up to a certain amount of stress and then held constantly. Hence, the shale creeps while the stress is kept constant. This means that the areas of failure are growing as the shear deformation in the sample increases. The increase in stress will be repeated in a stepwise manner until the sample finally fails. Strain-rate tests will also be run in order to study the effect of using different rates of deformation, providing a continuous loading path. This implies that the sample will be deformed with a fixed rate of deformation as the stress is applied continuously. Different rates of deformation are used to study the rate effect. An MTS electromechanical load frame will be used to apply stress on the sample in a continuous manner. Figure 4- 5 is a schematic illustration showing the effects of creep and varying strain rate.

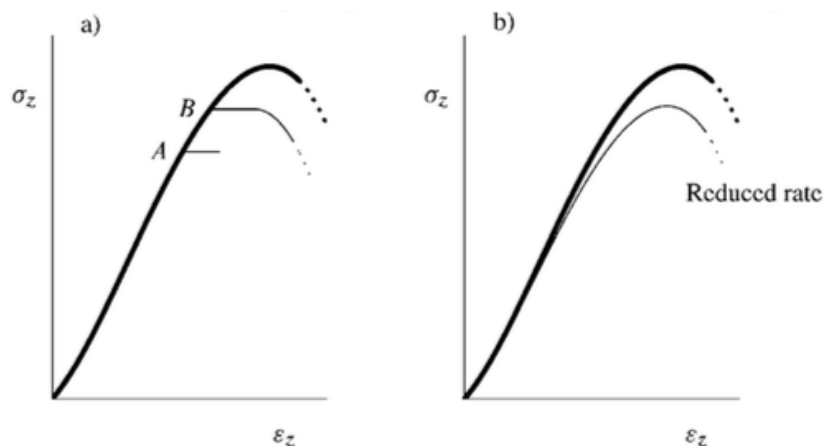


Figure 4- 5 Schematic illustration showing the effects of (a) creep, (b) strain rate (Fjær et al., 2008)

4.3 Sample Preparation

The Pierre samples used for testing are prepared from cylindrical core plugs that are drilled normal to the bedding plane (0°), with a sample diameter of 15 mm. The disk-shaped samples are then cut manually from the cylindrical core plugs with a handsaw. As the samples tend to have irregular surface, these need further preparation before CWT measurements and punching can be done. The disks are therefore manually grinded with abrasive paper (P 320) to ensure flatness and parallelism of the end surfaces. Figure 4- 6 illustrates the grinding process with abrasive paper. During grinding, the sample needs to be moistened with marcol oil to avoid desiccation.



Figure 4- 6 Grinding process during sample preparation



Figure 4- 7 A metal grinding unit to control the thickness

The grinding process continues until the sample reaches to a thickness close to the depth of the first dimple in the metal grinding unit, as shown in Figure 4- 7. The metal grinding unit ensures parallel plane surfaces and correct thickness of the sample. To ensure parallel surfaces on both sides of the sample, the sample is continuously turned and rotated while grinding. The grinding process is completed when the sample thickness is reached to 3 mm \pm 0.001 mm. The dimensions of the prepared shale samples are illustrated in Figure 4- 8.

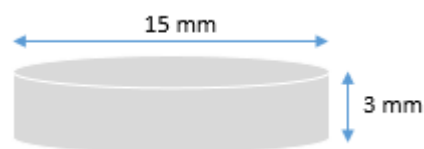


Figure 4- 8 The dimensions of the shale samples

All samples were initially prepared with a thickness of 3 mm. However, the samples that were immersed in marcol oil had to be re-adjusted after the first test, as a sample thickness of 3 mm appeared to be too thick to be punched. The oil samples were therefore later re-adjusted to 2 mm. This will be explained more in detail in *Chapter 5*.

4.3.1 Type of Exposure Fluids

After sample preparation, the samples will be immersed in different fluids to examine the fluids effects on shale. The samples can be stored in only marcol oil², which is supposed to be chemically inert and very pure. The chemical effects of exposing shale to other fluids are studied by using brine and hydrochloric acid. 3,5 wt% brine of sodium chloride (NaCl) is used, as this a concentration that should be close to the salt concentration of sea water.

Hydrochloric acid (HCl) is used to examine the chemical effects of the acid, specifically the effect of altering the pH of the shale. Several tests were done in order to find a proper concentration for the experiments. It was initially tested with much higher concentration on several larger core plugs, which concluded that a low concentration is preferable when testing on such small samples. The acid tests showed that a high concentration of HCl was too strong for the small shale samples, because the acid dissolved the samples. The concentration selected for testing is therefore as low as 0,00125 wt% hydrochloric acid, which gives a pH of 3,14. The test results can be found in Appendix E (Table E- 2).

4.3.2 Test Matrix for the Creep Tests

16 Pierre shale samples from batch ML 346_2 are prepared for testing in room temperature. When working with such small samples, it is important to avoid desiccation that can alter the properties of the shale material. All shale samples are therefore prepared while keeping them moist with an inert fluid (marcol oil) to avoid any direct exposure to air.

After sample preparation, the shale disks are stored individually in containers with either oil, brine or hydrochloric acid. 5 samples in marcol oil, 8 samples in brine and 3 samples in hydrochloric acid from batch 346_2 are tested in two series. The first series involves the 346_2 samples from 01 to 10, where the samples are kept 30 days in the fluids, summarized in Table 4- 1. Since the oil samples had to be re-adjusted to 2 mm, the storage time was extended with 5 days.

² Marcol or Marcol 82, is a purified mixture of liquid saturated hydrocarbons produced by ExxonMobil. It is a colourless, transparent, odourless and tasteless oil. Marcol is chemically inert and generally very pure. It is therefore commonly used in the laboratory for storage of shale samples. (Source: http://www.exxonmobil.com/Norway-English/Specialties/PDS/GLXXENSPCEMMarcol_82.aspx)

Sample no.	Type of Fluid	Exposure Time [days]
346_02_01	Marcol oil	35
346_02_02	Marcol oil	30
346_02_03	Marcol oil	35
346_02_04	Marcol oil	35
346_02_05	Marcol oil	35
346_02_06	3,5% Brine (NaCl)	30
346_02_07	3,5% Brine (NaCl)	30
346_02_08	3,5% Brine (NaCl)	30
346_02_09	3,5% Brine (NaCl)	30
346_02_10	3,5% Brine (NaCl)	30

Table 4- 1 Test matrix 1 for 346_2_01 to 10 samples

The second series comprises the 346_2 samples from 11 to 16, where the exposure time is significantly reduced to 2 hours or 15 minutes in the fluids, summarized in Table 4- 2.

Sample no.	Type of Fluid	Exposure Time [minutes]
346_02_11	3,5% Brine (NaCl)	120
346_02_12	3,5% Brine (NaCl)	15
346_02_13	3,5% Brine (NaCl)	15
346_02_14	0,00125% HCl	120
346_02_15	0,00125% HCl	15
346_02_16	0,00125% HCl	15

Table 4- 2 Test matrix 2 for 346_2_ 11 to 16

4.3.3 Test Matrix for the Strain-rate Tests

9 samples from batch ML 223_3 are prepared for running strain-rate tests with various predetermined rates of deformation. The test matrix for the samples with exposure fluid and time is presented in Table 4- 3.

Sample no.	Type of Fluid	Exposure Time [minutes]
223_3_01	Marcol oil	15
223_3_02	Marcol oil	15
223_3_03	Marcol oil	15
223_3_04	3,5% Brine (NaCl)	15
223_3_05	3,5% Brine (NaCl)	15
223_3_06	3,5% Brine (NaCl)	15
223_3_07	0,00125% HCl	15
223_3_08	0,00125% HCl	15
223_3_09	0,00125% HCl	15

Table 4- 3 Test matrix for 233_3 samples

4.4 CWT

After sample preparation, the thickness and the ultrasonic P-wave velocity of each sample are measured with CW (Continuous Wave) technique. The CW measurements will provide a measureable quantity of the homogeneity in the sample range. The shale material's cohesion can also be calculated from the obtained P-wave velocities.

4.4.1 Calibration

Calibration must be done prior to CWT measurements. A Plexiglas is used to calibrate the tool every time the P-wave velocity of the samples is measured. A Plexiglas provides good signals that can easily be picked up. The P-wave velocity for a Plexiglas should be $2200 \text{ m/s} \pm 50 \text{ m/s}$. The calibration data can be found in Appendix E (Table E- 4).

4.4.2 Thickness and P-Wave Velocity

To measure sample thickness, the sample is clamped between two piezoelectric ultrasonic transducers (Nes et al., 1996), indicated with an arrow on Figure 4- 9. A torque switch is used to control the clamping of the sample, which is located at the top of the digital micrometer. The sample thickness can easily be read from the digital micrometer with a precision of $1 \mu\text{m}$.

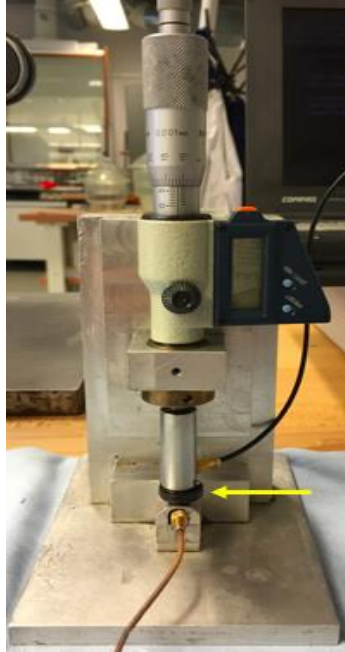


Figure 4- 9 Acoustic velocity measurements using CW technique. The sample is clamped between to transducers, as indicated with a yellow arrow.

The measurements are recorded using a computer program that measures and displays resonance curves of the samples. The initial inputs are listed in Table 4- 4, and the sample thickness is read manually from the micrometer;

Initial Values	Value
Start Frequency	1 MHz
Stop Frequency	6 MHz
Excitation Voltage	10 V
Amplification	60 dB
Sample Thickness	x mm

Table 4- 4 CWT Initial Inputs

A frequency generator generates the requested frequency sweeps, and a resonance spectrum will be displayed. The peak frequency points will then be manually picked out, and the P-wave velocities will be calculated according to standard deviation. If the deviation is large (>80 m/s), the picking process is either repeated or the sample will be tested again.

4.4.3 Test Procedure

For the 346_2 samples ranging from 01 to 10, the CWT measurements are conducted right after sample preparation and after 30 days' storage. These samples are stored either in brine or marcol oil before the puncher tests. The reason why the P-wave velocity is measured twice is to determine whether the exposure to brine will affect the P-wave velocities or not.

4.5 LVDT

4.5.1 Setup

The purpose of installing an LVDT is to measure the axial movement during puncher testing. The LVDT used is a Schaevitz MHR250, with a range of $3 \text{ mm} \pm 0.25\%$ linearity. The LVDT is installed on the torque wrench at the top of the shale puncher. The LVDT is connected to a data acquisition system, Quantum MX480B, which is further connected to a computer. All measurements are then recorded and stored in the software CatMan AP (V 3.5.1). Figure 4- 10 illustrates how the LVDT is connected to the puncher tool.

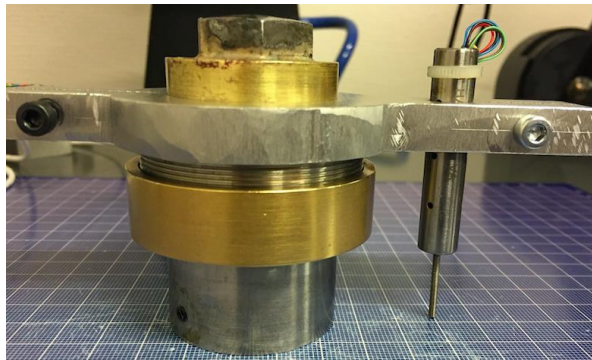


Figure 4- 10 LVDT connected to the puncher tool

For the creep tests performed by applying stress manually on the shale puncher tool, the sampling rate for the LVDT was 0,5 Hz. For the strain-rate tests with the electromechanical load frame, the sampling rate was improved to 1 Hz for the LVDT.

4.5.3 Calibration

Calibration of the tool is done prior to testing. A digital Mitutoyo micrometer, which is in accordance with the CatMan software, is used to calibrate the LVDT. The LVDT is calibrated with two-points, zero and the total load of all the weight plates. The linear range of the LVDT sensor is $\pm 3 \text{ mm}$.

4.6 Load Frame and Load Cell

A load frame is used to conduct the creep experiments, providing a dead weight loading on the puncher tool. Weight plates will be gradually added to the load frame to exert an axial force on the puncher tool. The stepwise load change and the resulting creep development will then be carefully monitored while recording. Figure 4- 11 shows the load frame with load cell, puncher tool and weight plates.

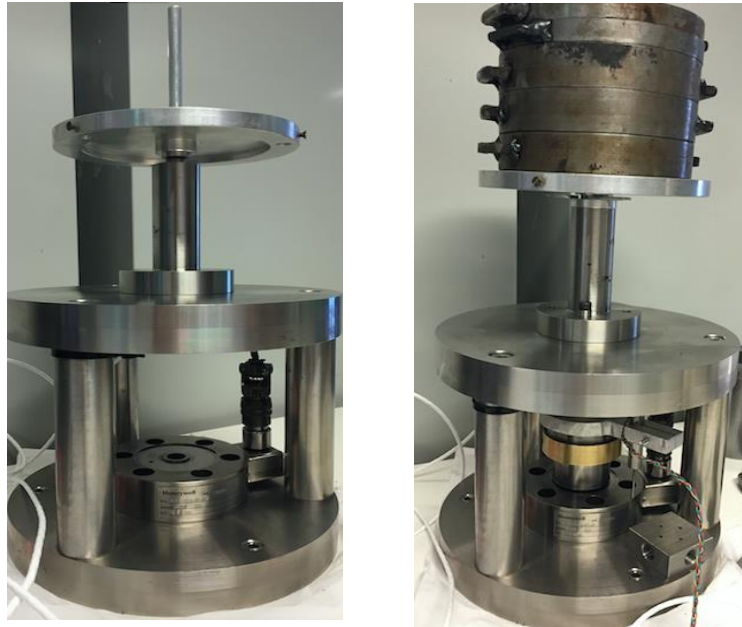


Figure 4- 11 Load frame. The right picture shows the load frame, while the left picture shows load frame with the puncher tool and weight plates

A Honeywell load cell is used to record the total weight added to the load frame, and the recordings are displayed on the software CatMan. The maximum weight that can be added to the load cell is 5000 lbs and the calibration of the load cell can be found in Appendix E (Table E- 1). Figure 4- 12 is a picture of the load cell.



Figure 4- 12 Load cell recording the total axial force applied to the load frame

4.6.1 Setup

The dimensions of the assemble tool are 10 cm in height and 8 cm in diameter. Thus, a small load frame will be sufficient to measure the axial force (load cell) and axial displacement (LVDT).

4.6.2 Test Procedure

The tests are run by varying the load applied on the puncher tool with different static time periods. The creep development during the stepwise loading will be carefully monitored with recordings from the load cell and LVDT.

4.7 Electromechanical Load Frame

A 50 kN MTS electromechanical load frame is used to run the strain-rate tests on the samples. The rate of deformation is a predetermined value that is set as a fixed rate, while the axial force is exerted continuously on the puncher tool. Figure 4- 13 shows the puncher tool that is placed inside the electromechanical load frame.

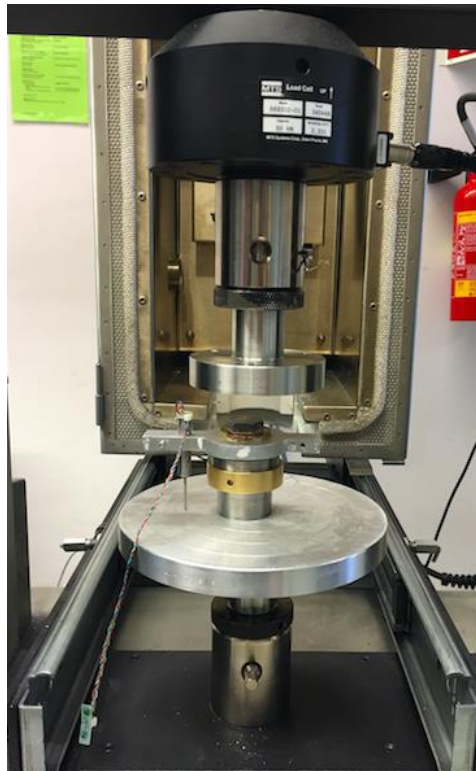
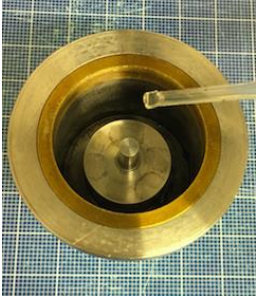
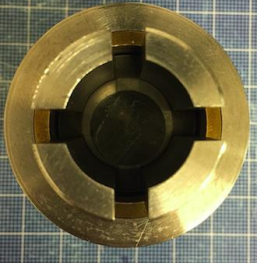
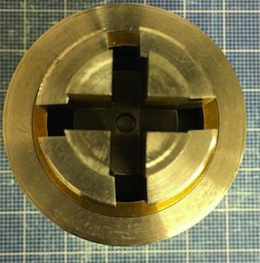




Figure 4- 13 The puncher tool placed inside the electromechanical load frame

4.8 Shale Puncher Test

After performing CWT measurements and calibration of the sensors, the shale samples can now be installed in the puncher. Table 4-5 presents a stepwise procedure for the puncher tool installation.

Step	Description	Illustration
I	The first step is to clean the bottom of the punching piston, as illustrated to the right. Add a few droplets of marcol oil to the bottom surface to avoid desiccation of the shale sample during testing.	
II	The next step is to place the sample in the center of the bottom clamping piston using a pincette. Fill up the space with marcol oil to ensure that the sample is fully hydrated during testing.	
III	Place the top clamping piston carefully above the sample.	
IV	Then place the top punching piston.	
V	Install the clamping piston locknut by using a torque wrench to control the rotation.	

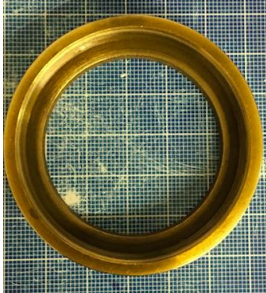
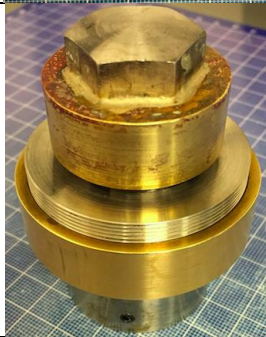
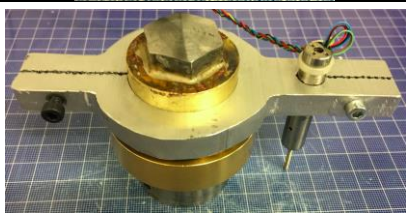

VI	<p>Connect then the clamping piston locknut (assembly from step V) to the bottom punching nut</p>	
VII	<p>Finally, use the torque wrench to tighten the connecting locknuts.</p>	
VIII	<p>Install the LVDT on the top clamping piston nut. The shale puncher is now ready to be placed in the load frame.</p>	
IX	<p>Place the puncher to the center of the load frame. This is to ensure even stress distribution across the whole puncher. Left: Load frame for creep test Right: Load frame for strain-rate test</p>	

Table 4- 5 Procedure for installing shale samples in the puncher

4.8.1 Procedure for Creep Test

16 creep tests will be run with a stepwise loading path to study how the sample creeps under constant load. Weight plates will be added to the load frame with a fixed time interval between each loading. The general procedure for performing creep tests with a stepwise loading path on the shale puncher tool is listed below:

1. Prepare the sample with a diameter of 15 mm and 3 mm thick
2. Measure the actual thickness and the P-wave velocity using CWT
3. Store the sample in the fluid type and time according to Table 4- 1 and Table 4- 2.
4. Measure the CWT again after the fluid exposure time
5. Install the sample in the puncher tool according to Table 4- 5.
6. Make sure that the LVDT is properly connected to the puncher tool with a torque wrench. The LVDT shall stay within the linear range (3 mm) during the entire experiment. The sampling rate for LVDT is set to 0,5 Hz.
7. Place the puncher tool in the center and inside the load frame
8. Start the software for recording the weight and displacement
9. Record manually the initial weight and the LVDT position from the CatMan software
10. Apply 2 kg (equivalent approx. 20 N)/4 kg (equivalent approx. 40 N) on the load frame every 15/30 minutes until a significant drop (approx. 0,3 mm - 0,5 mm) in deformation is observed on the screen (recording from the LVDT)
11. Take notes during the whole experiment in the laboratory journal

4.8.2 Procedure for Strain-rate Test

9 strain-rate tests with different rates of deformation will also be run. This is to study the effect of using different rates, and also how the rate of deformation evolves as stress is applied. These samples will also be installed in the shale puncher tool, but a continuous loading path will be used instead. This is done by using an electromechanical load frame, where the rate of deformation is a pre-determined value set in the CatMan software. The stress is then applied continuously until reaching 90% of the UCS, and the sample will finally creep to failure. The base calculations for the rates of displacement (test speeds) can be found in Appendix D, note that there were done some modifications of the test speeds during testing. The procedure for performing creep test with continuous loading path is as following:

1. Calculate the pre-determined deformational rate that will be used in the creep experiment

2. Install the sample in the shale puncher tool as described in *Table 4-5*.
3. Connect the LVDT to the shale puncher with a torque wrench as described in *Table 4-5*
4. Align the assembled puncher tool to the center of the load frame to ensure even stress distribution across the sample
5. Specify the test speed settings according to the pre-determined deformation rate
6. Check the procedures in the CatMan software and restart computer
7. Adjust the LVDT in the CatMan software. The sampling rate for LVDT is set to 1 Hz.
8. Start both recorders (LVDT and electromechanical loadframe). Note the time difference when starting the recording in both software
9. The test will now run automatically according to a pre-defined procedure and the stress will be exerted to the sample with the customized rate. Leave the equipment undisturbed
10. The test is continued until a hole has been punched through the sample
11. Take photos of the punched sample after creep test

Table 4- 6 is a table showing the rates of displacement (test speeds) used for running the strain-rate tests, and also the sample number and the saturation fluid.

Sample no.	Fluid	Rate of Displacement / Test Speed
223_3_01	Oil	0,003 mm/min
223_3_02	Oil	0,01 mm/min
223_3_03	Oil	0,02 mm/min
223_3_04	Brine	0,001 mm/min
223_3_05	Brine	0,0025 mm/min
223_3_06	Brine	0,005 mm/min
223_3_07	HCl	0,001 mm/min
223_3_08	HCl	0,005 mm/min
223_3_09	HCl	0,01 mm/min

Table 4- 6 List of the rates of displacement (test speeds) used for running strain-rate tests

4.9 Risk Assessment

A risk assessment has been conducted prior to the laboratory work, which is a part of the preparation for the experiments. This is important in determination of quantitative and qualitative risk related to a concrete activity or situation. The potential hazards have therefore been identified and the risks associated were also evaluated. Countermeasures to the potential hazards were suggested in order to reduce and mitigate the risks. A risk assessment form developed by SINTEF has been prepared in advance of the experiments, which can be found in Appendix F.

5 Experimental Results

The results obtained from the experiments will be carefully presented in this section. Due to the large amount of data, this chapter will mainly concentrate on the most relevant results. For the reader to get a better overview, this chapter is structured in a way where the presented results are followed up with a short discussion and analysis. Nevertheless, the next chapter (*Chapter 6*) will provide an extensive overall discussion of the most important elements from this chapter. All results can be found in Appendix A, B and C.

25 tests have been performed on the small shale samples to study the creep behaviour in Pierre shale. Two types of tests with different loading paths were conducted, which can provide a comparative study of the creep behaviour in shale. 16 creep tests were conducted by using the shale puncher tool with a stepwise loading path and various fluid exposure. These tests measured the gradual change in axial displacement over time under constant load. This can possibly provide information about the creep development in the small shale samples. The remaining 9 tests were run as standard strain-rate tests with a continuous loading path on the puncher tool by using an electromechanical load frame. The rate of displacement of each sample is a predetermined value, where an axial force is exerted on the sample continuously as the sample is displaced. Different rates of displacement were used to study the rate effect.

The successfully recorded data will be processed and analysed in the following subsections. Since this involves a wide range of tests and large amount of data are obtained from the experiments, only the most relevant will be presented and discussed. This chapter will therefore presents the relevant results and the results that show deviating trend. The data are presented in graphs, labelled with axial force and displacement as a function of time. Most of the experiments use small force and time increments that are considered to have small impact on the displacement, thus the experimental data are all visualised in a zoom-in format that illustrates the most relevant information.

The different stages of creep were also studied in detail, where the changes in axial displacement after each axial force loading are also plotted as a function of a relative time-scale. The magnified graphs show that the accuracy of the LVDT was somehow inadequate with noise fluctuations, and the fact that the LVDT has different axis range for each experiment. In response to this problem, a relative time-scale is used to improve the measurements of the axial displacement values. This is obtained by moving the curves to the same starting position (zero), which enables the curves to be comparable. This method also reduces the systematic error caused by the noise from the LVDT.

P-wave velocities for the samples were also measured using the CW technique. The cohesion of each sample was calculated according to the obtained P-wave velocities, and thereby the sample heterogeneities can be discussed.

5.1 P-Wave Velocities and Cohesion Calculations

5.1.1 P-wave velocity for Pierre Shale 346_2 - 01 to 10

From the test matrix Table 4- 1, the samples 01 to 05 were stored in marcol oil, while 06 to 10 were stored in brine. The P-wave velocities were measured *prior* to storage and *after* immersed in the fluid in 30 days. The change in velocity for each sample has also been calculated in percentage. The results are presented in Table 5- 1.

Sample no.	Vp_average Before Storage [m/s]	Standard Deviation for Vp [m/s]	Vp_average After Storage [m/s]	Standard Deviation for Vp [m/s]	Change in Vp [%]
Marcol Oil					
346_02 - 01	2533	53	2777	43	9,6
346_02 - 02	2571	69	2869	81	11,6
346_02 - 03	2471	22	2777	66	12,4
346_02 - 04	2522	57	2805	47	11,2
346_02 - 05	2607	60	2847	89	9,2
Brine					
346_02 - 06	2668	80	2355	24	-13,3
346_02 - 07	2556	76	2375	1	-7,6
346_02 - 08	2465	70	2332	35	-5,7
346_02 - 09	2664	82	2355	67	-13,1
346_02 - 10	2861	60	2259	80	-26,6

Table 5- 1 P-velocity summary table for 346_2_01 to 10

By studying the results in Table 5- 1, it is observed a time-dependent effect in exposing the samples to fluids. The measured P-wave velocities from CWT for the samples stored in marcol oil have actually increased after 30 days, varying from 9% and up to 12%. This is also presented graphically in Figure 5- 1. The spread in velocity within these samples are not too high, with only up to 5% in difference before storage and 3% after storage. The consistent velocities show therefore good sample homogeneity.

On the other hand, the velocities for the samples that are immersed in brine in 30 days show an opposite trend, as illustrated in Figure 5- 2. The velocities have actually decreased between 5% and 26%. The spread in velocity is much higher in these samples, where the highest difference can be up to 16% before storage, providing a higher sample heterogeneity initially. However,

the spread is reduced to 5% after storage. The reduction in spread indicates more homogeneity in the samples, which can be a result of full saturation and moisture after the exposure to brine.

The standard deviations of the measured P-wave velocity are also relatively small, thus reducing the uncertainty of the measured velocities. The uncertainty of the oil samples is approximately $2\% \pm 0,5\%$, whereas it is $3\% \pm 0,5\%$ for the brine samples. The reasons for the uncertainty are also discussed more in detail in *Chapter 6, section 6.3.3*.

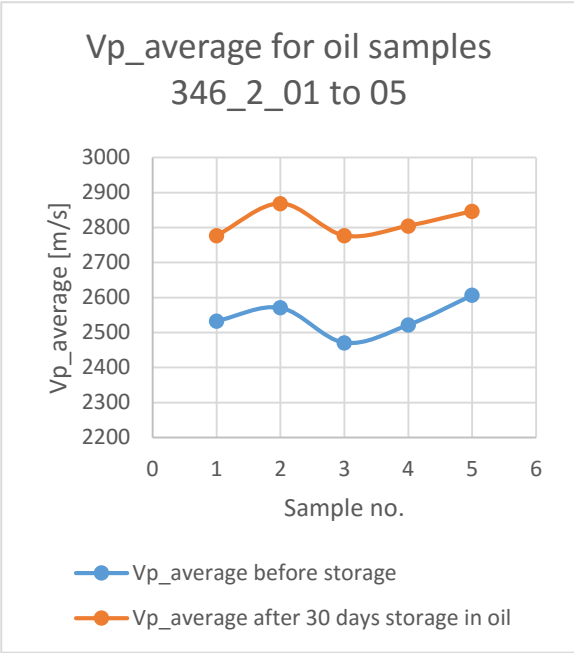


Figure 5- 1 P-wave velocities for oil samples before and after storage

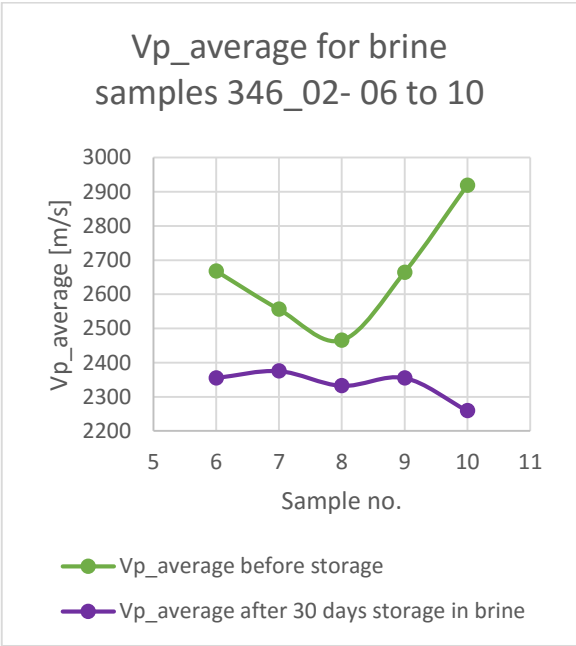


Figure 5- 2 P-wave velocities for brine samples before and after storage

Figure 5- 2 shows that the P-wave velocity for 346_2_10 deviates significantly from the other samples. Since the discrepancy is that high, the testing of this sample should be reconsidered. The reason for the abnormal high velocity initially can be that the sample is somehow drier than the other samples, providing a higher velocity before exposure to brine. After the sample is stored in brine, the P-wave velocity seems to be more consistent with the other samples. After exposing it to brine, the sample has become more saturated causing a reduction in the velocity again. However, this sample turned out to be disintegrated before any testing, thus no further actions were done to this sample.

5.1.2 Cohesion Calculations for Pierre 346_2 – 01 to 10

The cohesion of each sample has been calculated using the correlation presented in *section 3.1.2* Eq. 3- 9 to 3- 16. From the P-wave velocity obtained from the CWT tool, the friction angle and cohesion of each sample can thereby be calculated. The cohesion values for the samples are presented Table 5- 2. The calculated values for UCS and friction angle can be found in Appendix C.

Sample no.	Vp, cw	So	Vp, cw	So
	<i>Before storage</i>		<i>After storage</i>	
	[m/s]	[MPa]	[m/s]	[MPa]
346_2_01	2533	4,62	2777	3,62
346_2_02	2571	4,84	2869	3,7
346_2_03	2471	4,25	2777	3,52
346_2_04	2522	4,72	2805	3,62
346_2_05	2607	4,78	2857	3,24

Table 5- 2 Table 5- 2 Cohesion of the oil samples 346_2_01 to 05

From Table 5- 2, it is observed that the cohesion of the oil samples has increased after storage, which is expected since the P-wave velocities are increased. As cohesion is the measure of the inherent shear strength, an increase in cohesion means stronger rock.

In contrast, the cohesion for the brine samples 06 – 10 has decreased after immersed in brine, presented in Table 5- 3. In practice, the reduction in cohesion is a result of exposure to brine that weakens the rock strength of the shale. One possible explanation for this is that the salt concentration of the shale may be different from the brine concentration mixed in the laboratory, causing an ion exchange process in the clay-rich shale.

Sample no.	Vp, cw	So	Vp, cw	So
	<i>Before storage</i>		<i>After storage</i>	
	[m/s]	[MPa]	[m/s]	[MPa]
346_2_06	2668	5,09	2355	3,62
346_2_07	2556	4,9	2375	3,7
346_2_08	2465	4,28	2332	3,52
346_2_09	2664	4,92	2355	3,62
346_2_10	2861	5,9	2259	3,24

Table 5- 3 Cohesion of brine samples 346_2_06 to 10

5.2 Puncher Tests with Stepwise Loading Path

The results obtained from the puncher tests with a stepwise loading path will be presented in this section. A complete summary table for all the experiments conducted in the 346_2-series can be found in Appendix A. Note that all experiments will have an initial axial force of 15 N exerted on the puncher tool before any additional force is applied. It is also important to note that the time and force needed to punch the sample are located after the data is collected, as it is hard to determine the exact point of failure during testing. This means that for some experiments, the axial force was still applied even though the sample has failed, in order to ensure that the sample is actually punched.

The samples were loaded with weight plates of 1, 2 and 4 kg in a stepwise manner. However, to express this in terms of axial force, these values are converted to Newton [N].

Weight [kg]	Equivalent to [N]
1	9,81
2	19,62
3	29,43
4	39,24
5	49,05
6	58,86
7	68,67
8	78,48
9	88,29
10	98,10

Table 5- 4 Conversion table from kg to N

From the results (see Appendix A, Table A- 1, for the complete summary table), the following relationships are observed;

- If the axial force applied is small for each step, the time it takes to punch the sample is longer, because the sample gets accustomed with the new load
- The time step between each loading step is also relevant, as the samples will get longer time to creep under constant load
- Brine weakens the sample, which means that the time and force required to break the sample is significant reduced compared to the oil samples
- Hydrochloric acid seems to provide the same weakening effect as brine
- The maximum axial force required to punch the sample is equal for both the brine-rich and the hydrochloric acid-rich samples

In order to determine whether the puncher tool is able to give reasonable information about creep behaviour and important shale characteristics, the data obtained from the laboratory testing are carefully studied and analysed. As mentioned earlier, only the most relevant for discussion will be presented. However, the results for all samples and the relevant pictures are collected in Appendix A and G.

The results are presented in two types of graphs, where the first one shows how the deformation (also known as axial displacement) evolves as more force is applied as a function of time. A negative direction in the axial displacement axis implies that the sample is under compaction, thus shrinking.

The second type illustrates how the displacement develops each time more force is applied to the load frame. The starting point of the deformation values is therefore shifted to zero for each time the axial force is increased. The different displacement rates are thereby comparable as all graphs start from the same value. This enables the study of the creep development under constant load and when the sample is subjected to more force.

5.2.1 Readjusted Thickness of the Oil Samples

All samples were initially prepared with a thickness of 3 mm, but the oil samples (346_2_01 to 346_2_05) had to be re-adjusted to 2 mm after testing 346_2_02. The reason is that a 3 mm sample was too thick, thus strong, to be punched. The first puncher test was done with the disk-sample 346_2_02, and it was necessary to run two tests before the sample was successfully punched.

The first test was run for approximately 21 hours on the 3 mm thick sample. The sample was loaded with 20 N in every 30 minutes, but it was not punched even after 3 hours. The sample was therefore left unaltered for creep under constant axial force of 250 N in 18 hours, but unfortunately, there was still no indication of failure on the sample. The experiment was therefore terminated. The sample was still fine after the first test, and no fractures were directly visible on the sample. However, the P-wave velocity could have been measured to see whether the velocity has changed after subjected to axial force.

The second run was tested with the new thickness (2 mm), which was easily punched. This sample failed only 0,43 minutes after start with 53 N. Since a test of 21 hours have previously been done on this sample before, the rock strength is significantly reduced. The sample has also gone through a new grinding process to get a thickness of 2 mm, which means that this test is not representative.

This test led to the conclusion that a 3 mm thick sample immersed in oil is too strong to be punched. The other four samples, including this one, were therefore re-prepared and sanded down to 2 mm before any further tests were conducted. The results of the first and second run of this sample can be found in Appendix A, Figure A- 2.

5.2.2 Samples Immersed in Oil

The time-delayed deformation of shale is clearly seen on the results obtained from laboratory testing. The results show a typical creep behaviour, where the displacement of the shale samples continues for a long time after an increase in axial force has occurred. The sample 346_2_03 is used to illustrate this creep effect, shown in Figure 5- 3.

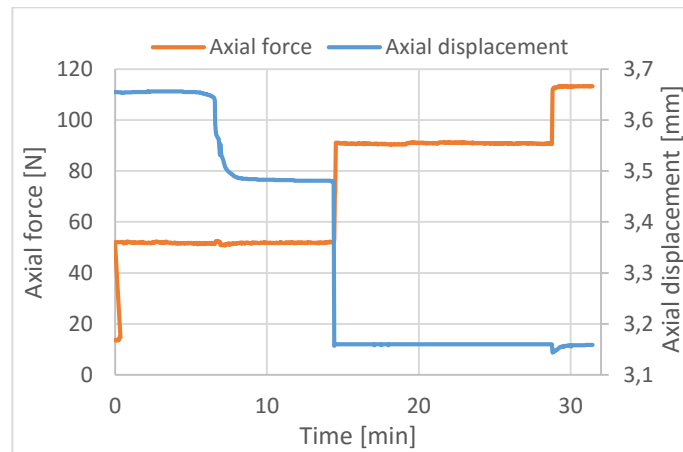


Figure 5- 3 Oil sample 346_2_03: Punch test showing the axial force applied and the resulting displacement

The sample 346_2_03 started with 15 N load initially, and the experiment was continued by adding 39,24 N load in every 15 minutes. Following Figure 5- 3, it is observed that the sample has a constant axial displacement after the first axial force is applied, until it suddenly displaces significantly under constant load. This is clearly a creep behaviour since the displacement of the sample occurs slightly after an increase in axial force has taken place. In terms of the three distinct creep stages, the sample creeps slightly in a transient manner initially and shortly after 6 minutes the sample starts to displace in a faster rate that phases in to the steady-state creep stage. The deformation reaches then to the final accelerating stage and the sample eventually fails after 14,5 minutes with 53 N. The oil samples are usually much stronger, but this sample is considerably weaker. This can be due to internal micro-fractures that initiated the failure process more quickly than the other oil samples.

To study the creep response to constant axial force, a zoom-in plot of this region on the same sample is plotted in Figure 5- 4. This zoom-in format illustrates the displacement of the sample after the first axial force (39.24 N) is applied, where reference position is shifted to zero. The

displacement is also plotted in reversed order to illustrate the characteristic S-curve of creep (See section 3.2.2) when subjected to constant load. Thus, a positive direction of the curve (i.e. negative values, due to the reversed order) indicates that the sample is displacing.

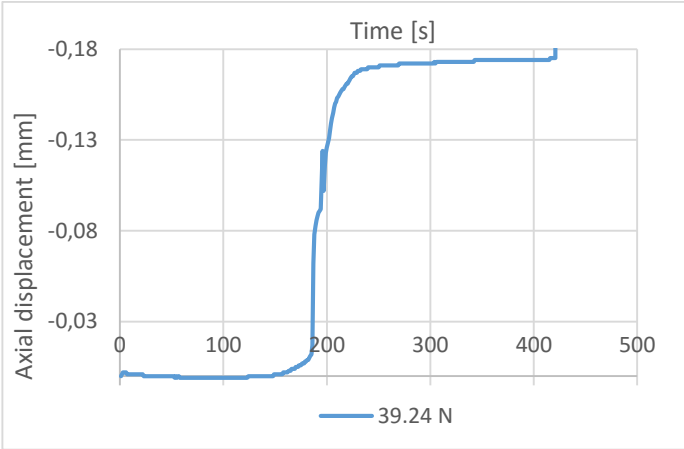


Figure 5- 4 Oil sample 346_2_03: Zoom-in format of the characteristic S-curve of creep after the first step of 39.24 N axial force is applied

However, displacement can also occur as the axial force is applied (not time-delayed). The results for 346_2_04 is plotted in Figure 5- 5, where it is observed a significant drop in axial displacement once the first axial force is applied, and then it continues to stabilize constantly with the new load. The same procedure is applied to this sample as for 346_2_03, where 39.24 N is added to the load frame in every 15 minutes. The sample continues to displace as more axial force is exerted, but stabilizes again with the new load until it finally fails after 30 minutes with 150 N.

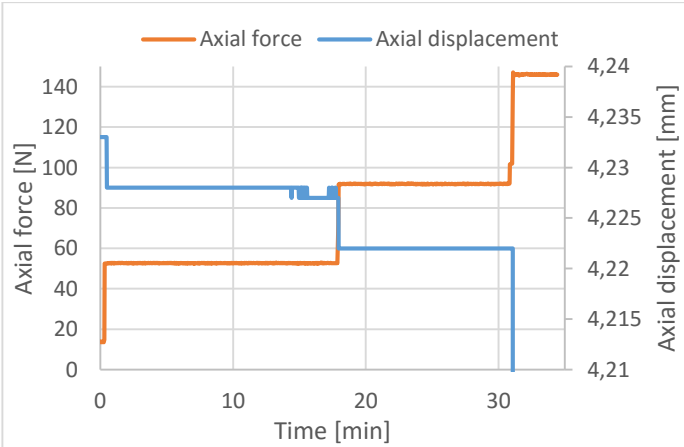


Figure 5- 5 Oil sample 346_2_04: Punch test showing the axial force applied and the resulting displacement

In contrast, 346_2_05 is tested with 19.62 N axial force in every 15 minutes to study the effect of reduced axial force applied in each time step. This is shown in Figure 5- 6. A hole was successfully punched after 2,2 hours with 175 N, thus significant more time and force are required to punch the sample. By comparing this test with the previous ones, it is observed that the displacement of the samples is actually dependent on the amount of axial force applied on each step on the loading path. The samples 346_2_03 and 346_2_04 were both increased with an axial force of 39.24 N in every 15 minutes, while this sample 346_2_05 was increased with 19.62 N with the same time steps. The results show that a high axial force (39.24 N) can punch the sample more easily than a lower force (19.62 N) loading, even though the time steps between each force loading are equal. This means that the sample experiences a rate effect when the loading step applied each time is doubled. Thus, more time and stress are required to punch 346_2_05, as the sample tends to equilibrate with the load every time the sample is subjected to more force.

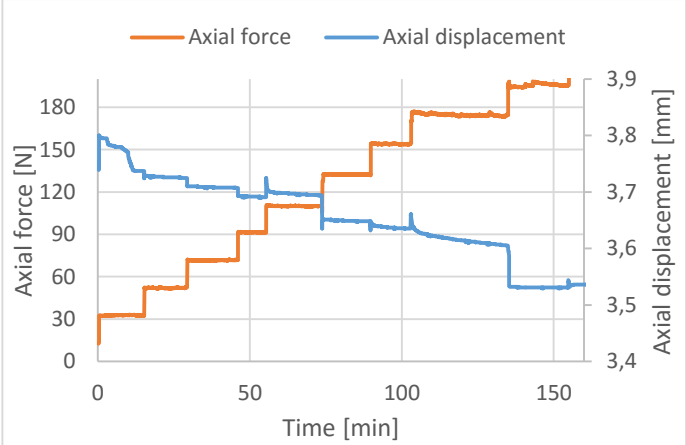


Figure 5- 6 Oil sample 346_2_05: Punch test showing the axial force applied and the resulting displacement

5.2.3 Samples Immersed in Brine

The brine-saturated samples were also successfully punched with the same loading procedures as the oil-saturated samples. Table 5- 5 is a clipart from the complete summary table in Appendix A, where the key properties of 346_2_08 and 346_2_09 samples are shown. It is observed that the holding time (for the sample to be subjected to constant axial force) is crucial for the total time needed to punch the sample. Moreover, the amount of axial force applied on the loading path also controls the time needed to punch the sample. This means that the holding time and the amount of axial force applied on the loading path controls the rate of deformation (creep). If the sample is left for a sufficient long time with constant load, the rock will be able to creep more.

Sample no.	Thickness	Storage Time	Fluid	Loading Path	Total testing time	Axial force punched	Time punched
8	3 mm	30 days	Brine	2 kg every 30 min	35 min	54 N	24 min
9	3 mm	30 days	Brine	1 kg every 15 min	1 hr	63 N	49 min

Table 5- 5 Clipart from the complete summary table (Fig. A-1 in Appendix A)

Another important finding is that the axial force required to punch the sample is significantly reduced in a brine-rich sample than in an oil-rich one. The sample 346_2_07 failed with 74 N after 49 minutes. The results are plotted in Figure 5- 7. The axial force required to break the brine-rich sample is almost halved compared to the oil samples that require around 150 – 180 N.

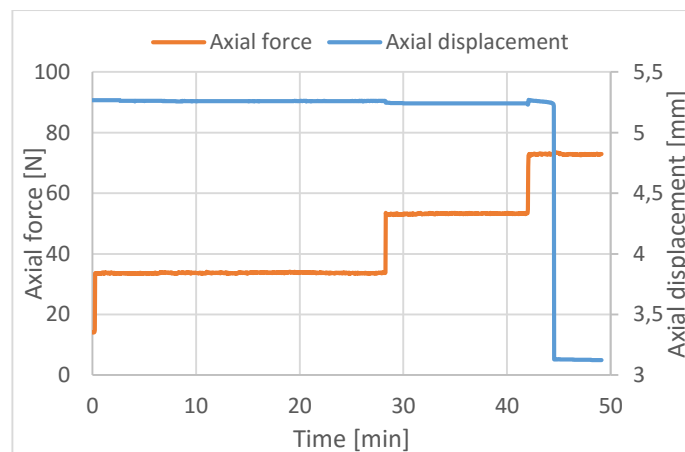


Figure 5- 7 Brine sample 346_2_07: Punch test showing the axial force applied and the resulting displacement

Moreover, to examine how brine can affect the creep development during each axial force loading, a zoom-in plot is used to study of the creep response to varying applied axial force. This zoom-in format illustrates the displacement of the sample every time the axial force is increased. As mentioned earlier, the start position of the deformation as each axial force step is

applied, is shifted to zero. This enables the different stages to be comparable. The time shown is a reference time scale that shows the deformation relatively to each other. In order to study the different creep stages more in detail, the deformation values are plotted in reversed order. This means that a positive direction (i.e. negative values) of the curves indicates that the sample is displacing.

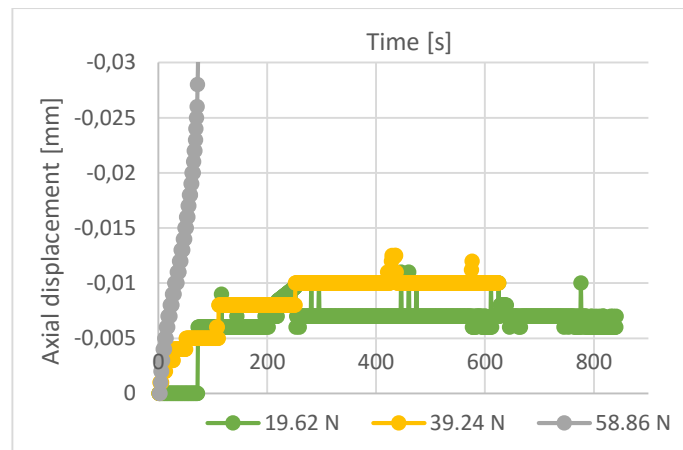


Figure 5- 8 Brine sample 346_2_07: Zoom-in format of the creep stages

Still focusing on sample 346_2_07, Figure 5- 8 is a zoom-in format of the creep behaviour of the sample. The graph indicates a typical characteristic development of the three distinct creep stages. It is observed from the graph that transient creep occurs when the first axial force step is added to the load frame (green curve). When the next step (yellow curve) is applied, the sample creeps in a faster rate than the green curve, but then it stabilizes again. It is hard to distinguish whether the sample still remains in the transient creep stage or it already has moved over to the steady-state creep stage. However, defining the intermediate stress regime is problematic as this is the boundary region between transient and accelerating creep, and the time scale for the three stages can vary significantly over a wide range.

The intermediate stress regime is where the material fully develops each stage of creep, but it is unfortunately hard to distinguish in practice. In fact, even the steady state creep itself can lead to failure. If this occurs, this means that the rock is loaded up to a level below its ultimate strength that initiate the failure after some time while it is subjected to a constant load. Considering the Figure 5- 8 again, it is clearly seen that accelerating creep occurs when the last stress step is added (grey curve) as the deformation is increased rapidly with time. Thus, the sample is accelerated to failure when the sample is successfully punched.

Recalling Figure 3- 8, this figure that illustrates a typical plot of creep development for different values of applied stress, which can be compared to this sample.

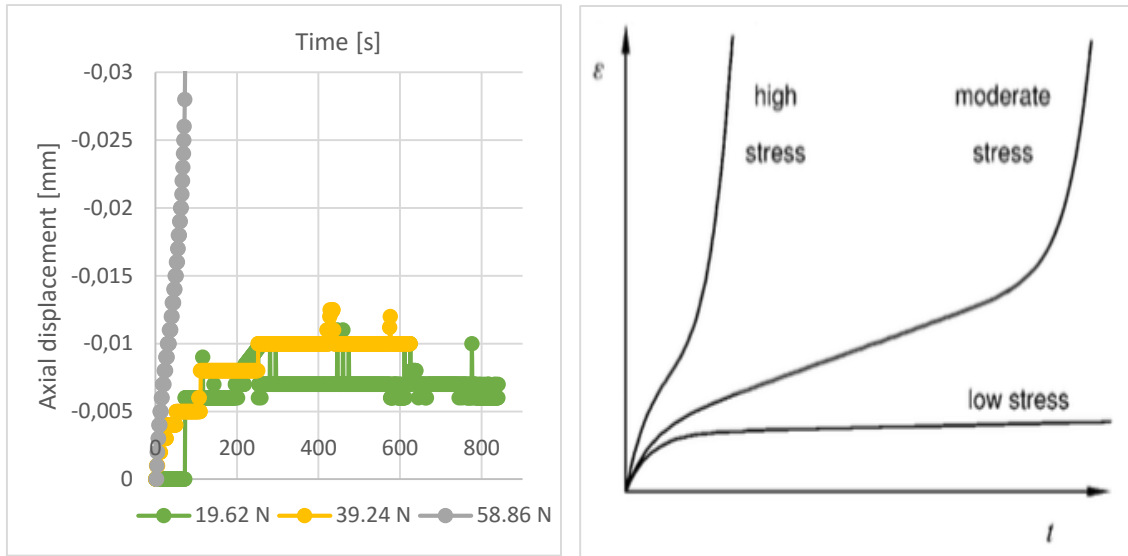


Figure 5- 9 Comparison of the experimental result of brine sample 346_2_07 and a typical creep response to varying applied stress

Figure 3- 9 is a comparison of the experimental results obtained from the brine sample 346_2_07 (also presented as Figure 5- 8) and a typical creep response plot to applied stress (Figure 3- 8). Generally, the actual creep development of a rock depends on the magnitude of the applied stress. For low or moderate stresses, in this case 19.62 N and 39.24 N loading, the material seems to virtually stabilize after a period of transient creep. For the high stress (58.86 N), the sample has already gone through the three stages of creep, until it finally fails.

Similar creep development can be seen in sample 346_2_12. Figure 5- 10 shows the axial force-displacement curve for the entire testing time.

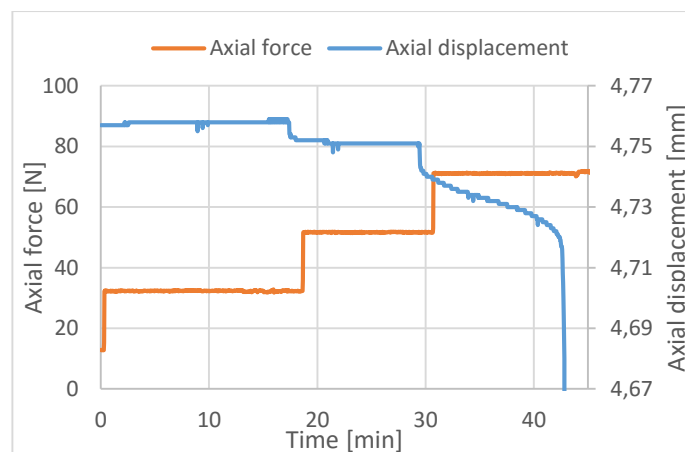


Figure 5- 10 Brine sample 346_2_12: Punch test showing the axial force applied and the resulting displacement

Figure 5- 11 is a zoom-in plot of the sample, which shows the axial displacement every time the axial force is increased (the axial displacement is plotted in reversed order). It is observed the same trend as the previous sample; the more axial force is applied, the faster is the rate of displacement. The green curve shows a slight increase in displacement indicating an expansion within the sample, but with only very small changes in amplitude. The displacement drops again in the yellow curve, and the rate of displacement increases rapidly.

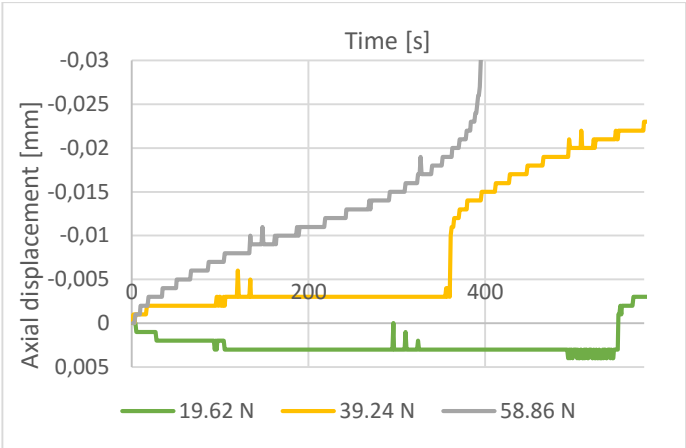


Figure 5- 11 Brine sample 346_2_12: Zoom-in format to study the creep stages

The grey one in Figure 5- 11 is the most interesting curve to study. Recalling Figure 3- 7, this figure shows the characteristic strain response for materials under constant stress. Figure 5- 12 presents a side-by-side comparison of the grey curve in Figure 5- 11 and Figure 3- 7. From the comparison, it is observed that the grey curve shows an identical characteristic S-curve of creep, where the sample goes through all the three stages in creep before it finally accelerates into a rapid process ending in failure under constant stress of 58.86 N (last axial force step applied).

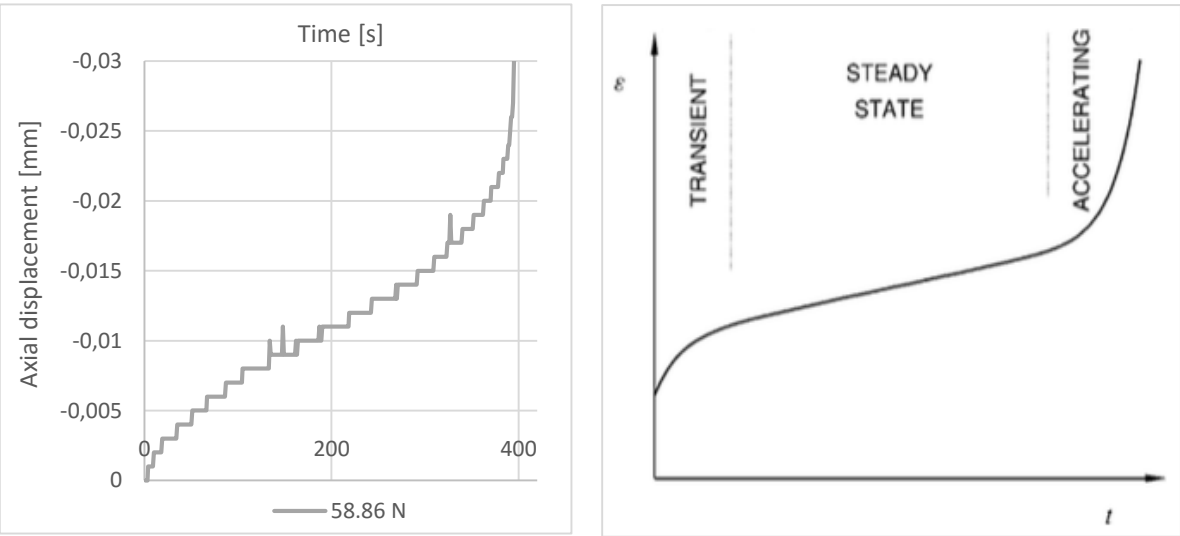


Figure 5- 12 Comparison of the experimental results of the brine sample 346_2_12 and a typical strain response curve for materials under constant stress

However, not all samples show equally interesting creep behaviour. The next section will designate the results that show deviating trends.

5.2.4 Deviating Trends

The experiments that have been presented so far seem to give reasonable explanation of the creep development in shale. However, not all tests showed the exact creep behaviour. In theory, the sample should contract (i.e. drop in axial displacement) every time an increase in axial force has occurred. This was not always the case. Consider the brine sample 346_2_13, shown in Figure 5- 13. It is observed that the displacement is dropped when the first force step is applied, which is reasonable as an increase in force initiates a displacement process. However, the displacement shows an opposite trend, where it starts to increase steadily even though the sample is subjected to constant load.

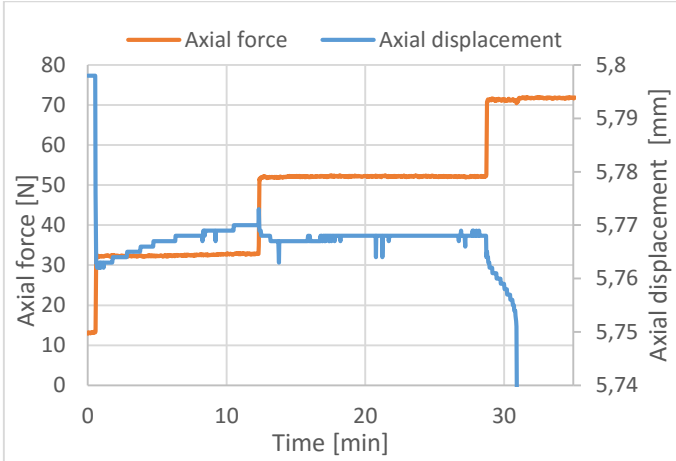


Figure 5- 13 Brine sample 346_2_13 (exposure time: 15 minutes): Punch test showing stress vs strain. An increase in strain is observed.

The increased-displacement phenomenon is also seen on the samples that were immersed in hydrochloric acid. This phenomenon is most decisive in the 346_2_15 sample, where the axial displacement increases every time the axial force is increased until it finally fails. The results are presented in Figure 5- 18.

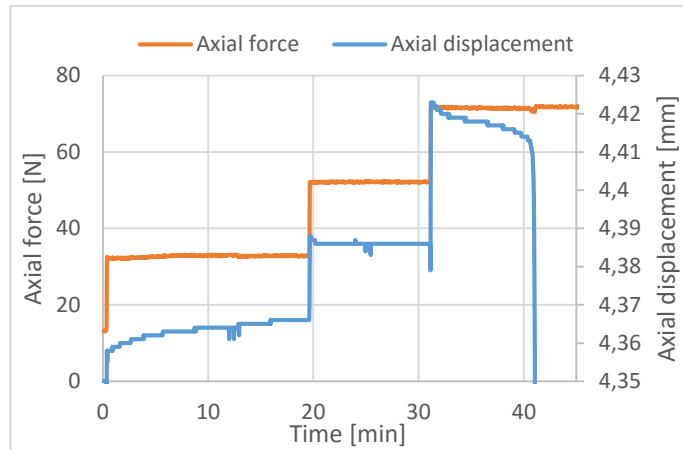


Figure 5- 14 Hydrochloric acid sample 346_2_15 (exposure time: 15 minutes): Punch test showing stress vs strain. An increase in strain is observed

A similar trend is also observed in 346_2_16, but only at the initial stage. The rest of the sample seems to develop in a reasonable manner. The results are shown in Figure 5- 19.

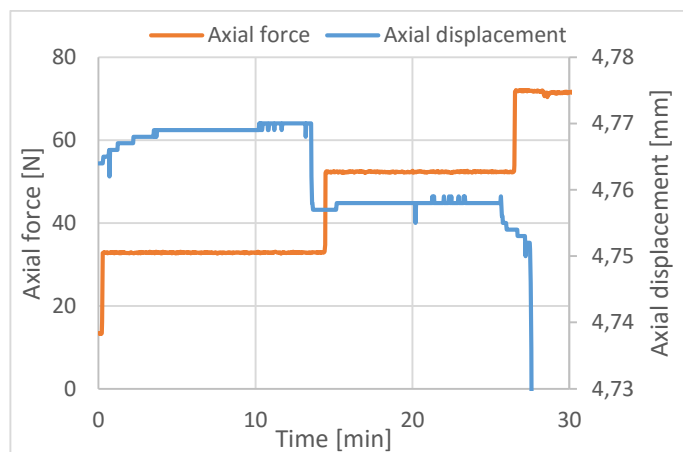


Figure 5- 15 Hydrochloric acid sample 346_2_16 (exposure time: 15 minutes): Punch test showing stress vs strain. An increase in strain is observed.

A positive increase in axial displacement indicates that the sample is expanding. It is also observed that this occurs particularly when the samples are immersed in brine/hydrochloric acid only in a short period of time (15 minutes). All samples presented in this subsection are only immersed in the fluids in 15 minutes, while the others presented earlier are exposed to the fluids in 30 days.

The increasing axial displacement phenomenon can be explained by two possible reasons. The first reason is related to the chemical effects from the exposure to the fluids, which is presented in the theoretical background section. The second reason involves the mechanical part of the puncher tool, where the sample can either be tilted inside the puncher tool when stress is applied

or the LVDT is not properly installed. The tilt effect will be studied in *section 5.4*, while the chemical effects will be discussed more in detail in *Chapter 6*.

5.2.5 Estimate of Temperature Effect

However, this phenomenon is also found in one of the oil-saturated samples. Figure 5- 16 illustrates the axial displacement of 346_2_01. At the initial stage, the sample creeps gradually after the first axial force step is applied. However, an *increase* in axial displacement occurs steadily, when the next axial force step is exerted. This clearly deviates from the expected, especially when the sample is left for creep under constant load.

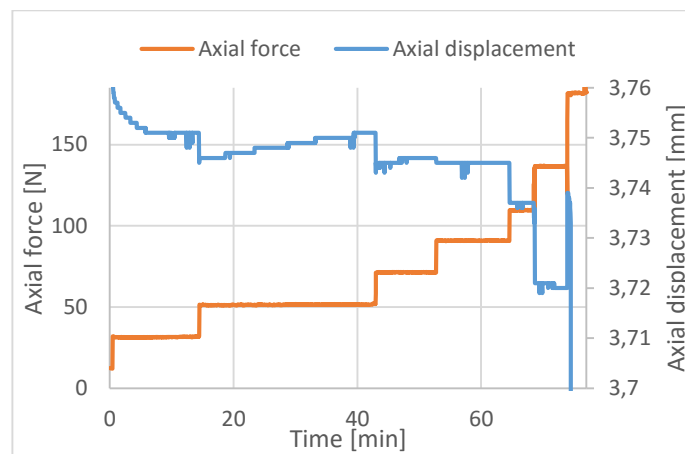


Figure 5- 16 Oil sample 346_2_01 (exposure time 30 days): Punch test showing stress vs strain. An increase in strain is observed.

Since this sample is only saturated with oil, this phenomenon cannot be explained by chemical alterations. The remaining explanation is either due to the tilt effect as emphasized earlier, or there actually may be a temperature effect. Temperature is believed to have a significant effect on creep in rocks, where a change in axial displacement can be caused by a change in temperature (Fjær et al., 2008). The temperature fluctuations in the laboratory were not measured during testing, but a rough estimate of the temperature change can be calculated to determine whether there is likely that an increase in displacement can be caused by temperature fluctuations or not.

The theory about thermoelasticity and the impact of a temperature change in a rock is presented earlier in *section 3.2.3*. From Figure 5- 16, the axial displacement is 0,006 mm (and the sample thickness is 2 mm). By using Eq. 3- 16, the axial thermal strain caused by a temperature change in the laboratory can be calculated. The exact value of the coefficient of linear thermal expansion for Pierre shale is unknown, the coefficient for Mancos shale is therefore used in order to calculate the an estimate of the potential temperature change in the laboratory. The linear expansion coefficient for Mancos shale is $13 - 20 \cdot 10^{-6} \text{ K}$ (Fjær et al., 2008), and the highest value ($20 \cdot 10^{-6} \text{ K}$) will be used.

Sample thickness	2 mm
Axial displacement	0,006 mm
α_T for Mancos shale (Fjær et al., 2008)	$20 \cdot 10^{-6}$ K
Change in temperature	150 °C

Table 5- 6 Calculations for a rough estimate of temperature change in the laboratory

The values used for the calculation of the potential temperature change in the laboratory is listed in Table 5- 6. By using Eq. 3- 16, the change in room temperature is estimated to be 150°C, which is not a reasonable value for a temperature change as it is considered as highly unlikely that the temperature can that high. The hypothesis of a temperature effect on the sample can therefore be discarded.

5.3 Puncher Tests with Continuous Loading Path

9 puncher tests have also been conducted with a continuous loading path with various rate of displacement, also known as strain- rate tests. Unlike the tests presented in section 5.2, the rate of displacement in these experiments is predetermined (test speed) that is run in a constant rate. The stress applied is increased continuously until the sample is successfully punched. The predetermined test speeds are based on the rates of displacement obtained from the experiments in section 5.2. By varying the rates of displacement, the effect of different rates of displacements on deformation will be examined. The base calculations of the test speeds can be found in Appendix D.

An interesting finding from these experiments is that all samples are punched approximately at the same position (Axial displacement value = - 0,03 mm).

5.3.1 Axial Displacement measured from Crosshead versus LVDT

During testing, the axial displacement is measured with two devices; a crosshead that is embedded to the electromechanical load frame and a local LVDT that is directly connected to the puncher tool. The test speed is manually set in the CatMan software, and the sample will be displaced with the fixed constant rate. The measured axial displacement from the electromechanical load frame (crosshead) will therefore give a linear line, while the LVDT will follow the actual displacement of the sample as the LVDT is directly connected to the puncher tool. Hence, the measured axial displacement from the LVDT will not be equally linear. Figure 5- 17 is an example (223_3_07) illustrating the difference in axial displacement between the crosshead and the LVDT.

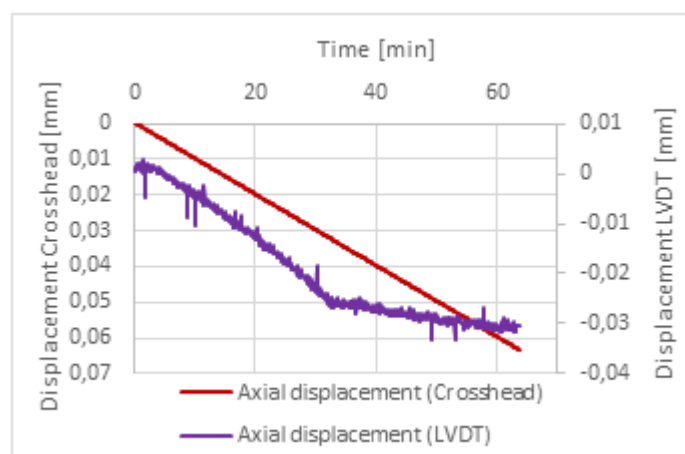


Figure 5- 17 Sample 223_3_07 (saturated with hydrochloric acid): An example of the difference in measured axial displacement between the crosshead and the LVDT

The most relevant axial displacement measurement is the one measured from the LVDT, as this follows the actual displacement of the sample. By studying Figure 5- 17, it is clearly seen that failure occurred when the orange curve (axial displacement from the LVDT) is sharply bent. This can not be seen on the axial displacement curve from the crosshead, because it is a fixed rate that is already pre-specified in the software. This means that the cross head will continue to displace the sample with the fixed rate even though the sample has failed. The following results will therefore only present the displacement values from the LVDT.

5.3.2 Axial force-displacement Curves

The results are plotted as axial force-displacement curves in order to study how the displacement evolves as the axial force is increased. Each fluid (oil, brine or hydrochloric acid) has three samples that are tested with three different rates of displacement. The first sample is tested with the slowest rate of displacement (blue curves), the second one with an intermediate rate (orange curves) and the last sample with the highest rate (grey curves). In order to compare the different rates as a result of applied axial force, these are plotted against each other.

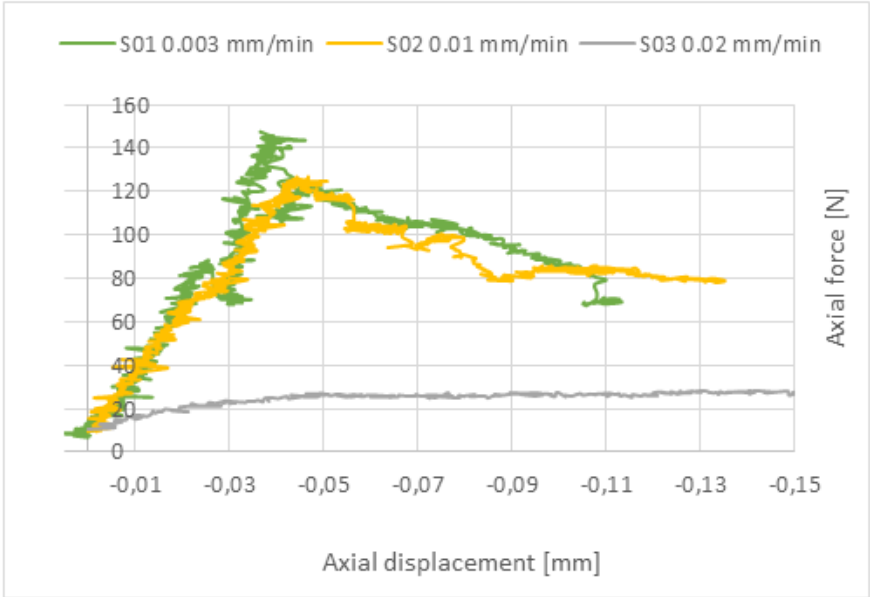


Figure 5- 18 Axial force-displacement Curve for 223_3_01, 02 and 03 (immersed in marcol oil)

Figure 5-18 shows an axial force-displacement curve for the samples that are immersed in marcol oil. By studying the figure, the first two samples show quite similar displacement behaviour when subjected to axial force, while the last sample with the highest rate of displacement seems to be the weakest one.

This is also observed in the samples that are saturated with brine and hydrochloric acid, where the sample with highest rate of displacement is the weakest one. The calculated test speeds for brine and hydrochloric acid are slightly slower than the ones used for oil, because these samples are significantly weaker as pointed out earlier. To punch an oil sample, the axial force required can be up to 150 N, while a sample immersed in either brine or hydrochloric acid only requires approximately 40 N for brine and 30 N for hydrochloric acid. Figure 5- 19 shows the axial force-displacement curves for the samples that are immersed in brine.

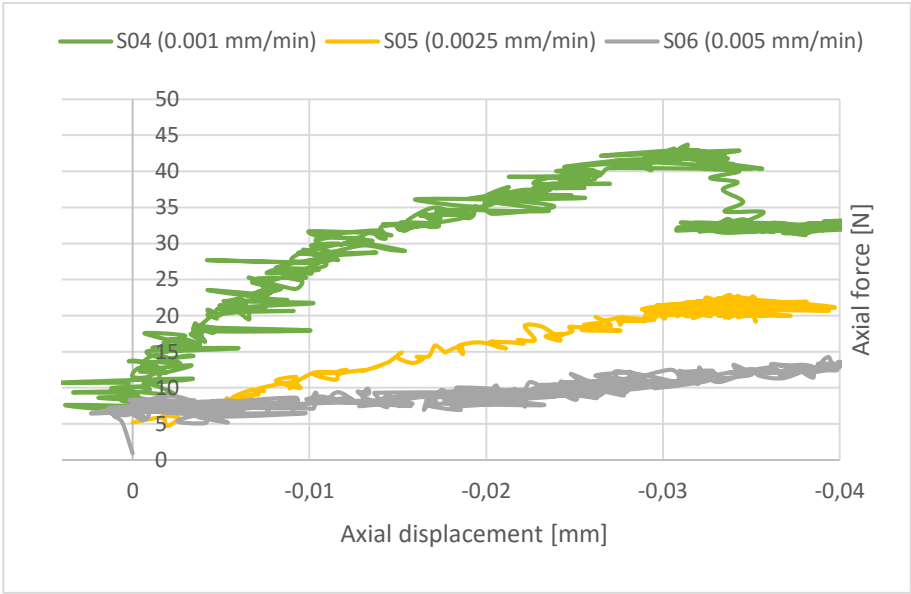


Figure 5- 19 Axial force-displacement Curve for 223_3_04, 05 and 06 (immersed in brine)

The axial force-displacement curves for the samples that are immersed in hydrochloric acid are shown in Figure 5- 20, where only two of the samples gave representative results. Similarly, the weakest sample is still the one with highest rate of displacement.

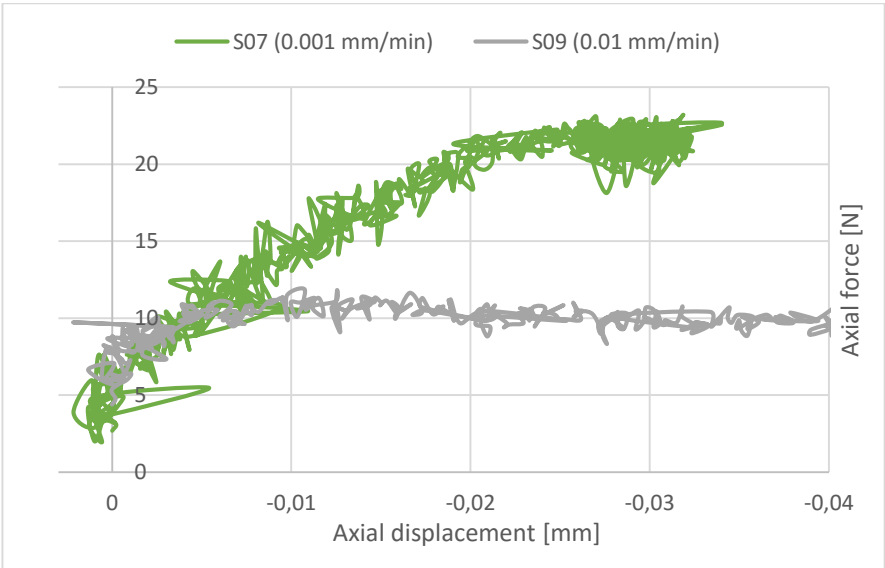


Figure 5- 20 Axial force-displacement Curve for 223_3_07 and 223_3_09 (immersed in hydrochloric acid)

Sample 223_3_08 was tested with an intermediate displacement rate of 0,005 mm/min. This sample is not shown in Figure 5- 20, because the test was terminated before the sample was actually punched. This sample has therefore two recordings, but none of them can be properly interpreted as the test was interrupted. The axial force-displacement curve for 223_3_08 is plotted separately in Figure 5- 21, and it is clearly seen that the axial displacement rate is confusing in the beginning. Since it is physical impossible that the displacement is both increasing and decreasing at the same time, this curve is therefore discarded. This test also confirms that a sample has “memory” of what it previously has been exposed to, and also that it is impossible to reverse the test again after axial force has been applied.

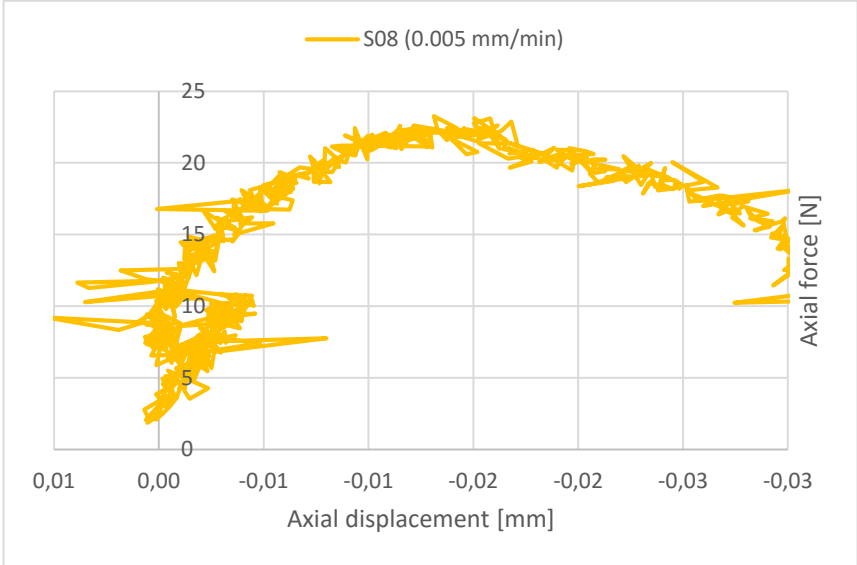


Figure 5- 21 Axial force-displacement Curve for 223_3_08 (immersed in hydrochloric acid)

5.3.3 Analysis of the Axial Force-Displacement Curves

Generally, when a rock is left for creep under constant stress, the deformation will increase with time and the rock will finally converge to failure (Fjær et al., 2008). In case of using a high displacement rate, the sample will actually not have sufficient time to creep, and thus being stronger by not creeping. This means that for a shale sample that is subjected to a high displacement rate, it is expected that this will be the strongest one.

However, this is not the case, as the sample with highest displacement rate appears to be the weakest one. This is most likely related to an increase in pore pressure, which is directly caused by a shrinkage in the shale. The sample experiences a certain amount of compression because of the applied axial force. The pore pressure is originated from the fluid content within the pore spaces of the shale, but it can also appear indirectly through effective stresses (Fjær et al., 2008). The effective stresses carry the forces transmitted through rock structure and thereby affecting the displacement of the rock. In a typical stress-strain curve, illustrated in Figure 5- 22, the effect of increasing pore pressure is actually moving the Mohr circle to the left, and hence closer to the shear failure line. A build-up in pore pressure will therefore destabilize the sample with respect to shear failure that eventually speeds up the failure process. This certainly explains why the sample with the highest rate fails more quickly, because there may exist a pore pressure build-up.

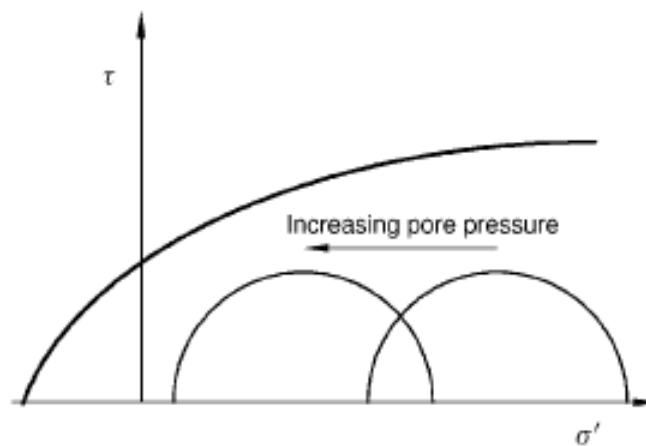


Figure 5- 22 Mohr circle and failure line: the effect of increasing pore pressure (Fjær et al., 2008)

5.4 Reliability of the Puncher Method

To examine whether there exists a tilt effect of the sample or not, a dummy test has been performed on a Plexiglas with the same test procedures for a stepwise loading path. Some of the weight plates were released harder on the load frame to examine whether human errors will give decisive measurements on the LVDT. The result is presented in Figure 5- 23. From the dummy test, it is observed that the axial displacement increases both when the axial force is increased *and* when the Plexiglas is subjected to constant axial force.

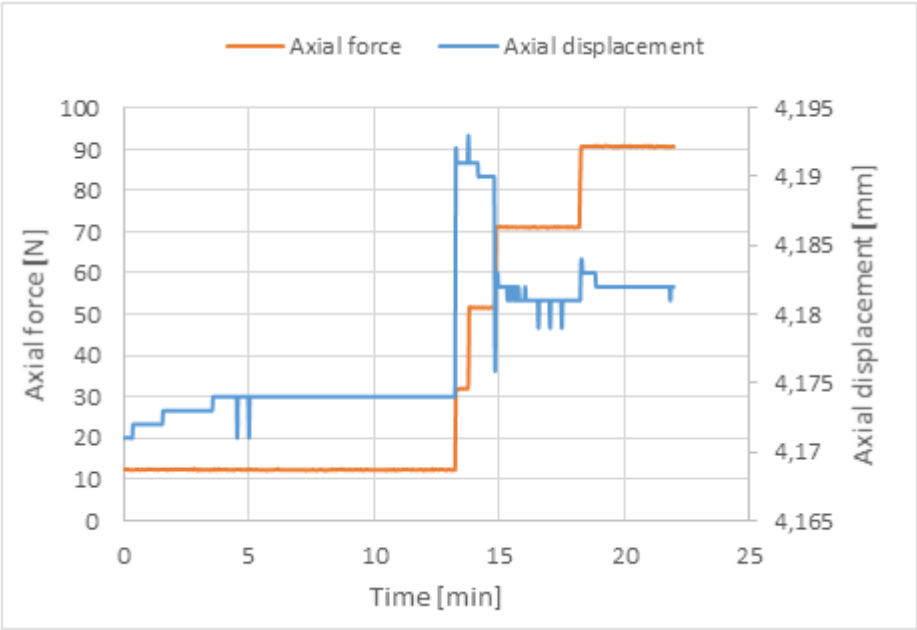


Figure 5- 23 Dummy test with Plexiglas to investigate the tilt effect

The observed phenomenon of increased axial displacement indeed raises questions about the reliability of using the puncher tool with a stepwise loading path as the measurements can be affected by human errors. However, a total of 16 experiments were conducted with the same equipment and procedures, and there were only 1 test that show excessive diverging trend and 4 of them that deviated to a small extent. One should also consider *when* this increasing displacement trend occurs; if it occurs suddenly when the axial force is constant for a while, this could be due to that the sample is about to fail (hence a tilt effect) or it could be related to chemical effects as mentioned earlier. On the other hand, if the displacement increases as a result of human errors, such as the weight plates are not carefully added as pointed out in this dummy test, then the increase in displacement is certainly a result of being inattentive. This test certainly confirms that a tilt effect can actually occur as a result of human errors. However, several experiments should be considered before this type of experiment is fully rejected as there are many factors that should be taken into account.

6 Discussion

6.1 Chemical Effects

From the results presented in *Chapter 5*, it is observed from the CWT measurements and puncher testing that the type of fluid that the sample is immersed in, actually influences the strength of the sample. Significantly less stress and time are required to punch a hole through the sample if it has previously been exposed to brine or hydrochloric acid. One possible explanation of this can be due to chemical effects within the clay-rich shale.

In case of brine, the salt concentration of the shale can be different from the mixed brine concentration in the laboratory, which initiates the exchange process and thereby weakens the rock strength of the sample. A number of researchers has investigated this effect, where it is also experimentally proved that ionic exchange may occur within shale if it is exposed to brine (Steiger, 1982; Horsrud et al., 1998).

This can also be explained in a capillary phenomenon point of view. Shales contain structurally bound water within the shale structure that contributes to the strength of the rock. In case of exposing the shale to brine/hydrochloric acid, the samples will get fully saturated. The saturated shale samples will thereby become weaker, because the capillary suction from the water is removed.

As pointed out in *Section 5.2.2*, it is observed an increase in axial displacement in the samples that are exposed to either brine or hydrochloric acid. The increase in axial displacement occurs typically at the initial phase where the first axial force step is applied. It is also observed that this effect is most significant if the exposure time to the fluid is very short (15 minutes). The samples that are exposed to the fluids in a longer period of time (30 days) are more stabilized, hence providing more reasonable results. The short exposure time may cause a larger difference in the chemical activity of the shale sample and the fluid, thus providing an increase in the displacement values when subjected to axial force. However, this effect seems to be significantly minimized when the exposure time is extended, as this enables the shale and the fluid to be equalized.

In order to obtain better results, the samples that are exposed to another fluid should be subjected to a constant load for an *even longer* period of time to study how the deformation develops under constant stress due to chemical effects.

6.2 Effect of Changing the pH

Similar behaviour is observed when the samples are exposed to hydrochloric acid. The samples are considerably weaker and less stress is required to punch these samples. However, if the sample is exposed too long to hydrochloric acid, the sample can be disintegrated by the acid. 346_2_11 was disintegrated after being 2 hours in the acid.

One of the objectives of this study is to examine the effect of altering the pH of the shale rock, and how this affect the creep processes. Hydrochloric acid was used to change the pH to 3,14, which appeared to weaken the shale considerably. The axial force needed to punch a sample that is saturated with the acid are significantly reduced. Kleiven & Lund (2016) has conducted a comprehensive study on how hydrochloric acid affects creep, and it is found that the shale cores that are immersed in hydrochloric acid creeps faster than the brine-rich samples. This explains why hydrochloric acid can weaken the shale, especially on the small mm-sized samples.

It is also found that if the exposure time is long enough (in this case 2 hours), the acid will disintegrate the shale even though the concentration is very low. Thus, an exposure time of only 15 minutes in the acid was used instead of 2 hours. It is predicted that the main impact of hydrochloric acid on shale will depend on the minerals dissolving, which is actually controlled by the acid strength, temperature and pressure (Morsy, Hetherington, & Sheng, 2013). The experiments could therefore have used an even lower concentration to let the shale stabilize with the acid in a longer period of time, without damaging the shale, to study more of the acid effects. The temperature can also be controlled in parallel with the acid concentration to examine the temperature effects.

The significance of changing the pH is a relevant topic for shale as a barrier in relation to carbon capture and storage (CCS). If shale is intended to seal off the wellbore, then it unquestionably must prevent the leakage of any fluids. In case of CCS, the injection of carbon dioxide (CO₂) can alter the pH of the shale, which in turn can alter the mechanical properties of the shale barrier. This undesired situation can cause leakage in the weakened shale, as a result of a change in pH. The effect of changing the pH in shale must therefore be properly quantified before shale can be used as a barrier element.

6.3 Effect of Pore Pressure

As the experiments involves pure shear stress on mm-sized shale samples, it was initially assumed that there will be no effect from the pore pressure in the shale. The advantage of not having a pore pressure effect is that the experiments can be conducted much faster than standard creep tests on core plugs, as there is no need to consider a volumetric change.

The pore pressure effect is proved to be significant in cases of where the samples are exposed to either brine or hydrochloric acid. Even though the samples are saturated with brine or hydrochloric acid, marcol oil must still be added to the puncher tool to avoid desiccation of the sample during testing. The samples that are immersed in either brine or hydrochloric acid will therefore get an oil film on the shale surfaces, which may initiate the pore pressure effect when the sample is subjected to an external force. According to the Mohr-circle, an increase in pore pressure will move the circle closer to left, hence closer to failure. The samples that are exposed to brine or hydrochloric acid were much weaker, which means that there may be an increase in pore pressure that caused the samples to fail more quickly.

Moreover, it is also found that a samples tends to get accustomed with the axial force applied, meaning that a pore pressure effect may be present. The pore pressure may be equalized as the sample is subjected to the axial force, which contributes to a more stabilized sample so more time and force are required to punch the sample.

If there certainly exists a significant pore pressure effect, this effect must be taken into account in the further investigation. The suggestions that may minimize this effect are discussed in *section 6.5.5*

6.4 Puncher Tests Discussion

From the experimental results, it is observed that the maximum axial force required to displace the sample in the puncher tool is dependent on the force applied in each time step. If the force applied each time step is high, the time required to punch the samples is significantly reduced compared to a lower force, known as a rate effect. Additionally, the time step between each loading also influences the rate of displacement as this has an impact on how much the samples creeps under constant load.

Stenebråten et al. (2008) developed the characteristic shale puncher tool for fast testing of small samples, where they provided the results in axial force and displacement instead of stress and strain. Hence, the axis on the graphs obtained from these puncher tests are also labeled with the same units. Incidentally, it is not a major problem that the curves are plotted in axial force and displacement as the samples have equal thicknesses, but this is not comparable with other test

samples. For comparison with other samples that have different dimensions and thicknesses, it is advantageous of plotting the curves in terms of stress and strain.

However, the conversion to stress and strain is problematic for the results obtained from the puncher tool, because there is probably a situation where the stress geometry changes from indentation to pure shear failure during the axial force loading (Stenebråten et al., 2008). If more detailed deformation studies are conducted with this tool in the future, this point must be studied more comprehensively. Nevertheless, it is still meaningful to compare the samples that have been saturated with different fluids (exposure to oil, brine or hydrochloric acid), although this discussed point has not yet been properly clarified.

6.5 Temperature Sensitivity

Temperature is considered to have a significant impact on creep processes, but this was not measured during the experiments. Although the rough estimate of temperature change calculated in *section 5.2.5* showed that it is unlikely that a temperature change can influence the measurements, the effect of temperature should still be considered with more accurate and scientific measurements.

Hallberg (2011) performed a comprehensive study with the puncher tool too, and where the effect of temperature on shale strength was also examined. This study concludes that the temperature dependency of shale strength can be explained by several factors; the release of bound water from interlayer space, pore pressure increase due to thermal expansion coefficients of pore water and clay minerals, softening of clay minerals caused by chemical reaction with the pore water and reduced solid-fluid friction.

6.5 Sources of Error

6.5.1 Parallelism of the Disk-shaped Samples

If the surfaces between the sample and the clamping piston on the puncher tool are not parallel, the stress applied on the sample will not be evenly distributed. This increases the local stresses in parts of the sample, leading to higher creep in these areas. This may result in early collapse of the sample as one side of the sample is subjected to higher concentration of axial force than the rest of the sample.

6.5.2 Sample Thickness for the Oil Samples

As discussed in *section 5.2.1 Disk-sample 346_2_02*, the test concluded that a sample thickness of 3 mm is too strong to be punched. This test resulted that the other samples had to be re-prepared to 2 mm. Thus, these samples have gone through sample preparation, storage and then a new sample preparation where new fractures on the sample can possibly be initiated. The oil samples are not fully comparable with the brine-rich and acid-rich samples as the thickness is reduced. This should be taken into account when considering the results.

6.5.3 P-Wave Velocity

Many factors can affect the accuracy of the P-wave velocity measurements. The process of sawing and grinding during sample preparation can contribute to a wider spread in the measurements. It is difficult to obtain the exact same thickness and parallel surfaces during sample preparation. The P-wave velocity needs also to be measured in the center of the sample, which was challenging when parallelism of the disk-sample is not fully achieved. Furthermore, manual picking the calculating points in the CW technique contributes to uncertainties in the measured velocities. Large values in standard deviation of the measured P-wave velocity can indicate the presence of internal micro-fractures within the samples. To ensure accuracy in the measured velocities, several measurements should be carried out.

6.5.4 Sample Desiccation

As stated earlier, it is very important to avoid drying out the shale during the entire experiment by always keeping it immersed in a fluid. However, the desiccation of the sample can happen very quickly, which can alter the rock properties drastically. The highest possibilities of desiccation are during measuring the P-wave velocity with CWT or that not enough marcol oil is added in the puncher container during testing. To avoid desiccation of the sample, the sample should be put right back into the fluid container quickly and ensure that enough oil is covering the sample.

6.5.5 Pore Pressure Effects

As discussed earlier, there may exist a pore pressure effect due to the oil film on the shale surfaces in the samples that are saturated with either brine or hydrochloric acid. The pore pressure effect alters the creep development, which should be taken into account. One possible solution that can minimize the pore pressure effect is to moisturize the samples with the saturation fluid (brine or hydrochloric acid) instead of oil during testing. The oil film on the sample surfaces is thus avoided, and a capillary suction is reduced.

However, it is hard to ascertain this effect since the permeability of shale is very low. To examine whether there really exists a real pore pressure effect, a shale puncher experiment should be performed on a more permeable rock.

6.5.6 Temperature Effects

Temperature has significantly impact on creep. Since this was not tested on these experiments, the temperature influence is a *potential* source of uncertainty. The influence of temperature may affect the equipment used, and thereby also the measurements and the rock strength of the samples. The reason for this temperature effect is yet unknown, but probably caused by combination of several reasons; stress changes caused by thermal expansion, large variations in temperature from nearby air condition and temperature dependency of the LVDT.

6.5.7 Noise from LVDT

In the laboratory, people can walk very close to the experiment area. If someone bumps into the table that the measurements are going on, this will provide additional fluctuations in axial deformation in the CatMan software, thus providing noise to the LVDT. For improving the accuracy of the measurements, several LVDTs or higher sampling rate (f.ex. 5 Hz) should be used. It is also important to stay within the linear range of the LVDT (± 3 mm) to ensure the accuracy of the measured strain. It is therefore recommended to use at least 3 LVDTs to get average values.

6.5.8 Noise from Load Cell and Limitation of Load Frame

The load cell is designed to carry a weight of maximum of 2 tons, but the maximum load for some of the experiment was only 25 kg (approx. 250 N). This can cause much fluctuations and noise in the CatMan software.

The construction of the load frame will provide additional uncertainties to the load cell and/or LVDT, because friction will occur between the piston and the puncher tool (Figure 4- 11 illustrates the piston on the load frame). This frictional effect is present in the experiments where weight plates are added manually.

6.5.9 Time Increments

Applying equal time steps between each axial force loading on the puncher tool was also a challenge. The time steps should be consistent during the whole testing on each sample.

7 Conclusion

A series of experiments have successfully been conducted in order to evaluate the applicability of a compact tool, designed to study the creep properties in shale. The testing of small samples facilitates a fast and inexpensive method in obtaining creep parameters. The creep process in shale is a result of time-delayed deformation in the rock that enables the shale to form an efficient well barrier. Creep is an interesting process to study as it integrates traditional rock mechanics with both chemistry and basic fluid mechanics. It is therefore important to emphasize the creep effects in shale in order to predict whether shale is able to function as a permanent barrier, where it is also known that the chemical properties of the pore fluid can affect the creep process. From this extensive study, the following findings have been observed;

- In the puncher tests with stepwise loading path: The axial force exerted on the sample in each time step controls rate of deformation of the sample. If the force applied on each time step is large, the time required to punch the sample is significantly reduced (rate effect)
- An increase in time step resulted in an increase in creep, because rock undergoes more deformation under constant load
- In the puncher tests with a continuous loading path and predetermined displacement rate: the weakest sample is the one with fastest displacement rate
- There may exist a pore pressure effect, as some of the samples were accustomed (hence, more stable) with the axial force applied, and more time is required to punch the sample
- The samples that were saturated with brine (3,5 wt% NaCl) were considerably weaker. Hence, less time and axial force were required to punch the sample
- Similarly, a reduction in pH (pH=3,14) with hydrochloric acid (0,00125 wt% HCl) also weakened the samples considerably
- The samples that were immersed in only oil for a longer period of time experienced an increase in P-wave velocity. Conversely, the P-wave velocities were decreased for the brine-rich samples with equal exposure time. Hence, a time dependent effect is observed
- A sample thickness of 3 mm for an oil-rich shale was too strong to be punched in the puncher tool. The small sample managed to withstand 250 N for 21 hours without breaking.

In order to ascertain whether these small scale tests on the puncher tool is able to provide easy access to creep parameters, the test procedures and the discussed uncertainties must arguably be significantly improved. This is essential in emphasizing whether these creep parameters can support the use of shale as a permanent barrier. Yet, the puncher stool still has a convincing potential to study the creep properties in shale. Based on the experimental results obtained in this study, the puncher method seems to provide reasonable creep behaviour. However, no conclusion can be drawn until further investigations have been conducted.

8 Future Work

As stated in conclusion, in order to verify the applicability of puncher tests for studies of creep effects, further actions are required. Thus, the sources of error discussed in *section 6.5* must be rectified. The most important measure is to conduct even more experiments to get a wide base of experiments that can quantify the creep effects more accurately. Due to the limited time frame of the laboratory work, some of the planned experiments were not carried out in this semester and several improvements could have been done if more time was available. More experiments can be done by varying the thickness of the samples (ranging 3 mm, 2.5 mm, 2 mm and etc.), type and concentration of exposure fluid, exposure time to the fluids, the stress applied, and the duration of constant load. It is also recommended to be as accurate as possible with the time steps to get consistent measurements. The effect of temperature is considered to have a great influence in creep, which is considered as highly relevant for further investigation.

The main uncertainty in the experiments conducted in this thesis is that only one LVDT was used to measure the deformation. The use of only one LVDT has created uncertainties, and thus the reliability of some results are compromised. The measurements can be easily improved by using at least 3 LVDTs to ensure accuracy of the deformation. If one of the LVDT fails, the other two LVDTs can still provide measurements.

The laboratory tests on Pierre shale also aimed to reveal effects of changing the pH and the resulting chemical alterations. This can be improved by using an even lower concentration of hydrochloric acid and then leave it for a longer period of time to let the sample stabilize with the fluid without disintegrating the sample. Also, the significant increase and decrease in P-wave velocity of leaving the shale in marcol oil and brine for a longer period of time should also be verified with more samples.

The effect of pore pressure can be established by running a creep experiment with a more permeable material than shale in the puncher tool. This effect can also be minimized by moisturizing the sample with the saturation fluid in the puncher container during testing, instead of using marcol oil. This can reduce the effect of capillary suction that induces a pore pressure effect within the samples.

Finally, taking the experimental results one step further, the graphs can be modeled with curve fitting by using existing creep models. Several creep models have been developed in order to describe the macroscopic effects of creep. The creep models can be a useful tool in interpreting the results more properly, and ascertain whether the results are reasonable or not. Thus, all these measures are of high relevance for further investigation in order to quantify the applicability of small scale tests to determine the creep processes in shale.

Bibliography

- Abshire, L., Desai, P., Mueller, D., Paulsen, W., Robertson, R., & Solheim, T. (2012). *Permanent Well Barrier*. Houston: Schlumberger Oilfield Review.
- Atkinson, B. (1982). *Subcritical crack propagation in rocks: theory, experimental results and applications*. South Kensington: Journal of Structural Geology Vol.4 No.1.
- Bauer et al. (2014). *Thermally Induced Compaction of Shales*. Trondheim: SINTEF Petroleum Research & NTNU.
- Chen, Z. (2015). *Lecture notes: PTR5024 Drilling Fluids and Cementing*. Sydney: University of New South Wales.
- Chester, J., Lenz, S., Chester, F., & Lang, R. (2004). *Mechanisms of compaction of quartz sand at diagenetic conditions*. Earth and Planetary Science Letters 220, 435-451.
- Dowling. (2007). *Mechanical Behavior of Materials* (Vol. 3rd edition).
- Fam & Dusseault. (1998). *Borehole Stability in Shales: A Physico-Chemical Perspective*. Trondheim: SPE/ISRM 47301.
- Fam et al. (1998). *Borehole Stability in Shales: A Physico-Chemical Perspective*. Trondheim: SPE/ISRM 47301.
- Fjær E. (1999). *Static and Dynamic moduli of weak sandstones*. In: Amadei, B., Kranz, R.L., Scott, G.A., Smeallie, P.H. (Eds). Balkema: Rock MEchanics for Industry.
- Fjær et al. (2002). *Mud Chemistry Effects on Time-Delayed Borehole Stability Problems in Shale*. Texas: SPE/ISRM 78163.
- Fjær et al. (2008). *Petroleum Related Rock Mechanics 2nd edt*. Elsevier.
- Fjær et. al. (2014). *A creep model for creep*. Minneapolis: ARMA 14-7398.
- Fjær, E. (2006). *Modeling the stress dependence of elastic wave velocities in soft rocks*. Trondheim: SINTEF Petroleum and NTNU.
- Fjær, E., Folstad, J., & Li, L. (2016). *How creep shale may form a sealing barrier around a well*. Houston: ARMA 16-482.
- Fooks, J., & Dusseault, M. (1996). *Strength of Pierre I shale as function of moisture content*. Rotterdam: Eurock.
- Hallberg, E. (2011). *Master Thesis: "Temperature Dependent Shale Strength and its Effect on Borehole Stability"*. Trondheim: NTNU.
- Holt et al. (1996). *Fluid effects on acoustic wave propagation in shales*. Rotterdam: Balkema.
- Holt, R. (2013). *Poroelasticity, Lecture Notes in TPG4185 Formation Mechanics*. NTNU.
- Horsrud et al. (1998). *Interaction between shale and water-based drilling fluids: Laboratory exposure tests give new insight into mechanisms and field consequences of KCl contents*. Louisiana: SPE 48986.
- Horsrud, P. (2001). *Estimating Mechanical Properties of Shale from Empirical Correlations*. SPE Drilling & Completion, 16, 68-73.

- Kleiven & Lund. (2015). *Specialization Project; "Creep and Consolidation Effects in Pierre Shale"*. Trondheim: NTNU.
- Kleiven, M., & Lund, E. (2016). *Master Thesis. "Creep and Consolidation in Pierre Shale, Identification of how time-dependent effects are influenced by alteration in pore fluid pH and changes in stress conditions"*. Trondheim: NTNU.
- Meyers & Chawla. (1999). *Mechanical Behaviour of Materials*. Cambridge University Press.
- Morsy, S., Hetherington, C., & Sheng, J. (2013). *Effect of Low-Concentration Hydrochloric Acid on Properties of Shale Rocks*. Pittsburgh: SPE 165689.
- Nes et al. (1996). *Rig-site and Laboratory use of CWT Acoustic Velocity Measurements on Cuttings*. Milan: SPE 36854.
- OLF, & TBL. (2004). *NORSOK Standard D-010 Well integrity in drilling and well operations*. Lysaker: Standards Norway.
- Olsen, J. (2015). *Master Thesis: Investigation of Creep Characteristics for Stresses close to Failure*. Trondheim: NTNU .
- Park, R. (2005). *Foundation of Structural Geology (reprint of the 1997 Chapman and Hall edition)*. Routledge, Abingdon.
- Steiger , R. (1982). *Fundamentals and use of potassium/polymer drilling fluids to minimize drilling and completion problems associated with hydratable clays*. J. Petr. Tech 34, 1661-1669.
- Stenebråten et al. (2008). *The shale puncher - a compact tool for fast testing of small shale samples*. Trondheim: ARMA 08-227.
- Stroisz, A., & Fjær, E. (2011). *Nonlinear elastic wave propagation in Castlegate sandstone*. San Francisco: 45th US Rock Mechanics/Geomechanics Symposium, ARMA.
- Van Der Pluijm, B., & Marshak, S. (2004). *Earth Structure (Vol. 2nd ed)*. New York: W.W. Norton & Company Inc.
- Williams et al. (2009). *Identification and Qualification of Shale Annular Barriers Using Wireline Logs During Plug and Abandonment Operations*. Amsterdam: SPE/IADC 119321.
- Zhao, X., & Roegiers, J. (1995). *Creep crack growth in shale*. Oklahoma: Balkema.

Appendix A Results: Puncher Test with Stepwise Loading Path

Table A- 1 Complete summary table for all experiments in 346_2-series

Sample no.	Sample Thickness	Fluid Exposure Time	Fluid	Loading Path	Total testing time	Axial load punched	Time needed punched
1	2 mm	35 days	Oil	2 kg every 15 min	1,3 hrs	18,5 kg	1,24 hrs
2 (1st run)	3 mm	30 days	Oil	4 kg every 30 min	20 hrs	Not punched	-
2 (2nd run)	2 mm	35 days	Oil	4 kg every 15 min	30 min	5,3 kg	0,43 min
3	2 mm	35 days	Oil	4 kg every 15 min	30 min	5,4 kg	14 min
4	2 mm	35 days	Oil	4 kg every 15 min	35 min	15 kg	31 min
5	2 mm	35 days	Oil	2 kg every 15 min	3 hrs	17,8 kg	2,2 hrs
6	3 mm	30 days	Brine	4 kg every 45 min	1,3 hrs	5,4 kg	16,5 min
7	3 mm	30 days	Brine	2 kg every 30/15 min	50 min	7,5	45 min
8	3 mm	30 days	Brine	2 kg every 30 min	35 min	5,5 kg	24 min
9	3 mm	30 days	Brine	1 kg every 15 min	1 hr	6,4 kg	49 min
10	3 mm	30 days	Brine	DISINTEGRATED	-	-	-
11	3 mm	NOT TESTED	Brine	NOT TESTED	NOT TESTED	NOT TESTED	-
12	3 mm	15 min	Brine	2 kg every 15 min	45 min	7,3 kg	44 min
13	3 mm	15 min	Brine	2 kg every 15 min	45 min	7,3 kg	31 min
14	3 mm	2 hours	HCl	DISINTEGRATED	-	-	-
15	3 mm	15 min	HCl	2 kg every 15 min	49 min	7,3 kg	43 min
16	3 mm	15 min	HCl	2 kg every 15 min	45 min	7,3 kg	29 min

Figure A- 1 Axial force-displacement curve vs time and the resulting zoom-in format of the displacement changes as more axial force is applied

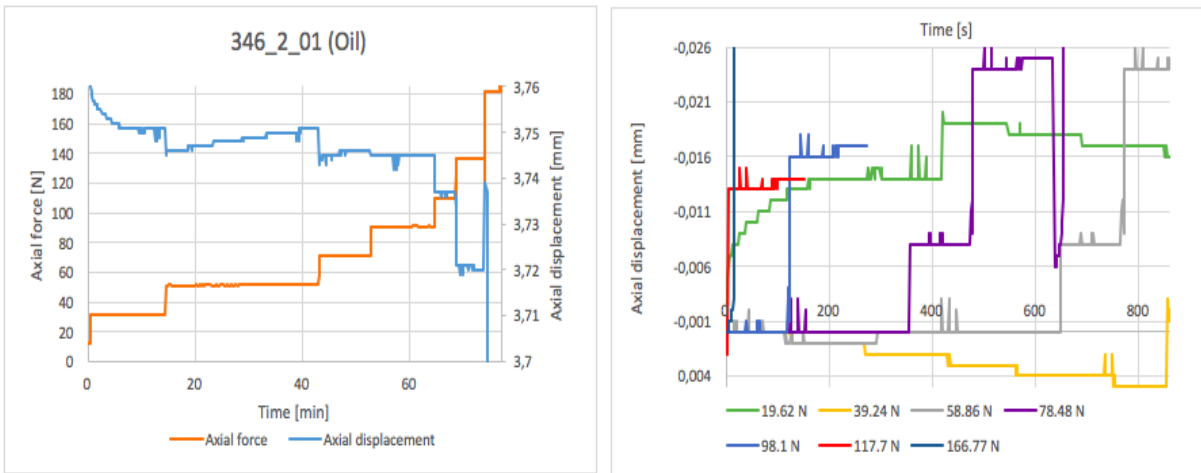


Figure A- 2 Oil 346_2_02: Axial force-displacement vs time curve for the first and second run on the sample. Left: the sample was not punched after left unaltered for 21 hours. Right: the sample is easily punched after 0.43 min.

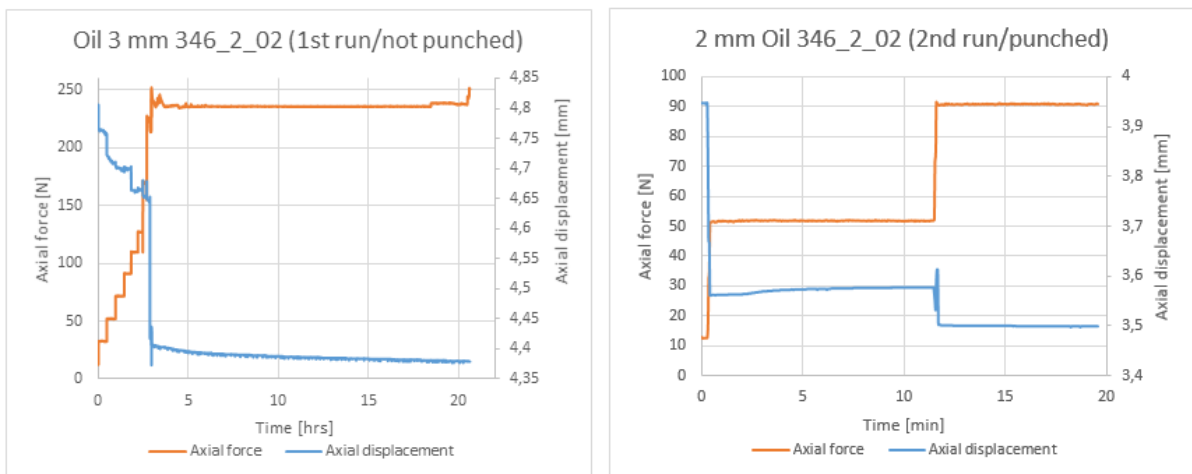


Figure A- 3 Oil 346_2_03: Axial force-displacement curve vs time and the resulting zoom-in format of the displacement changes as more axial force is applied

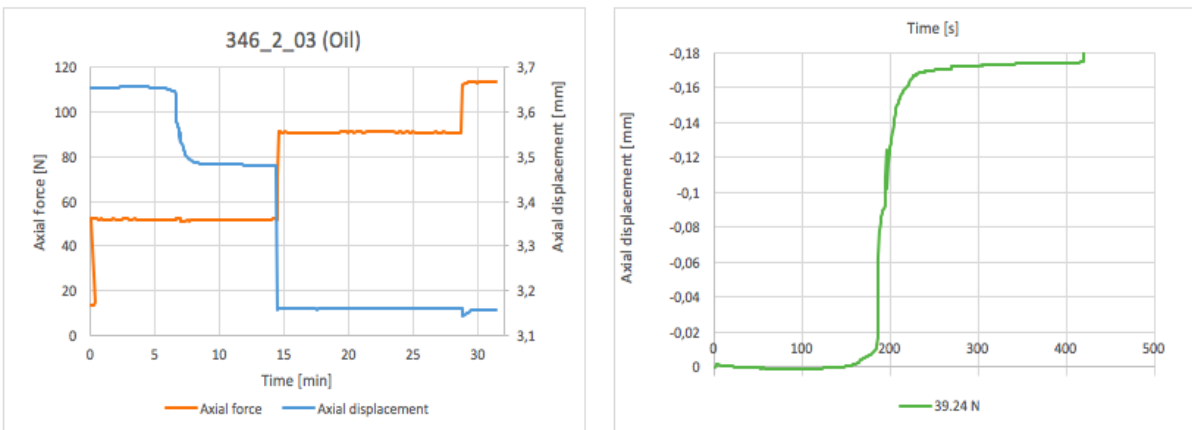


Figure A- 4 Oil 346_2_04: Axial force-displacement vs time curve and the resulting zoom-in format of the displacement changes as more axial force is applied

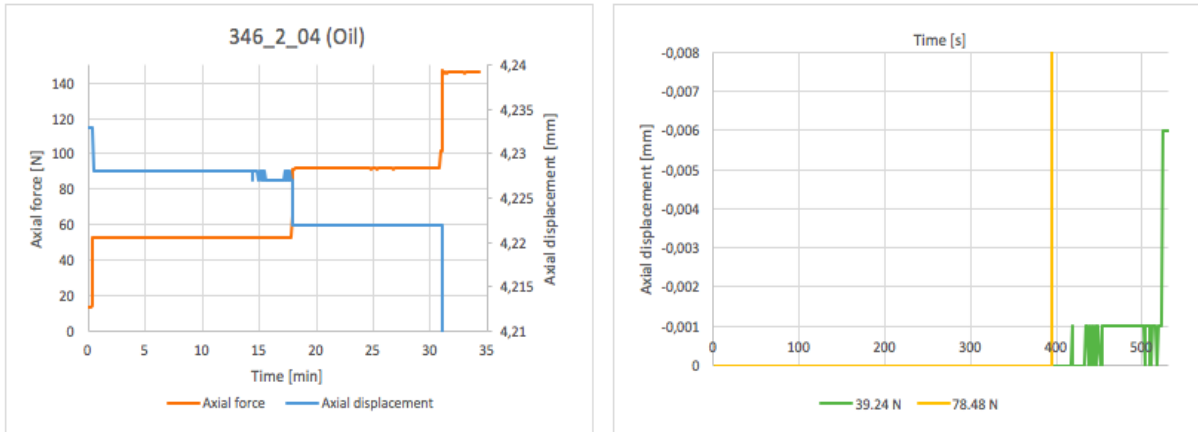


Figure A- 5 Oil 346_2_05: Axial force-displacement vs time curve and the resulting zoom-in format of the displacement changes as more axial force is applied

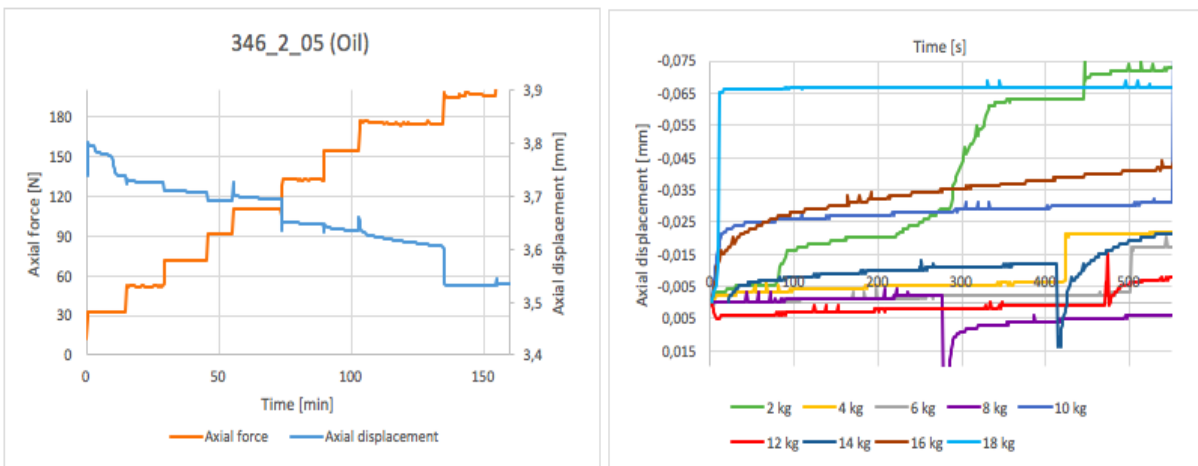


Figure A- 6 Brine 346_2_06: Axial force-displacement curve vs time and the resulting zoom-in format of the displacement changes as more axial force is applied

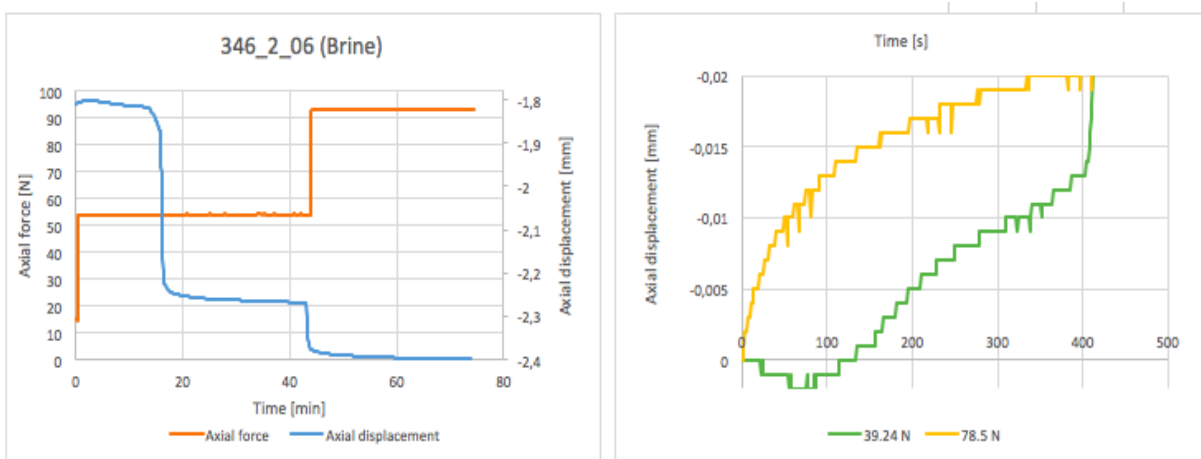


Figure A- 7 Brine 346_2_07: Axial force-displacement curve vs time and the resulting zoom-in format of the displacement changes as more axial force is applied

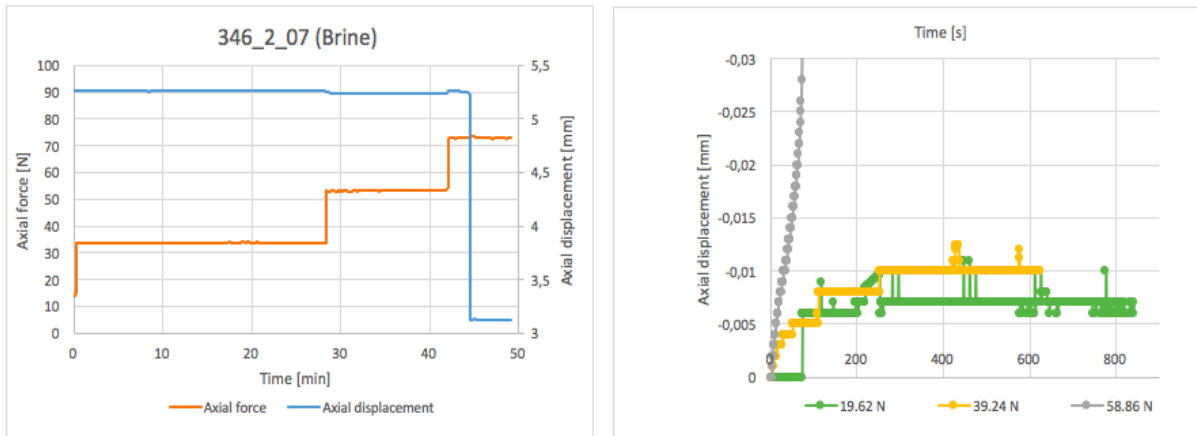


Figure A- 8 Brine 346_2_08: Axial force-displacement curve vs time and the resulting zoom-in format of the displacement changes as more axial force is applied

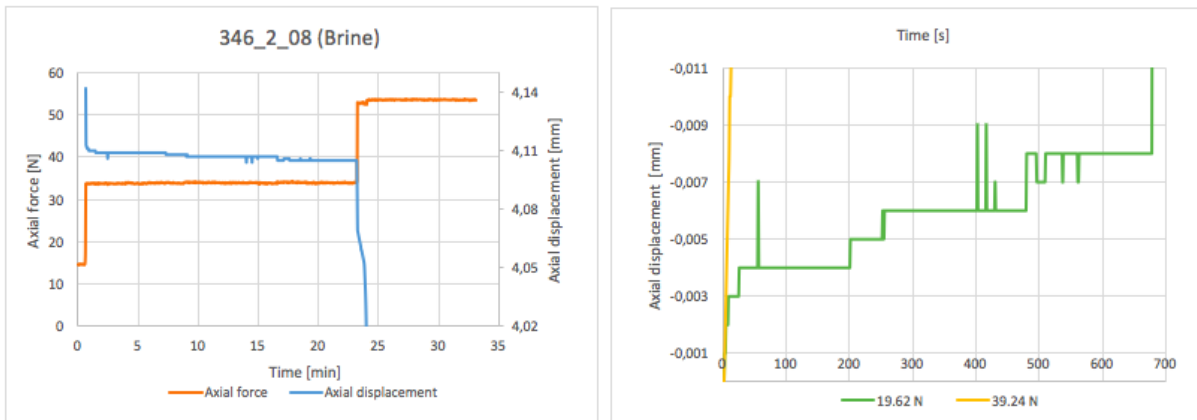


Figure A- 9 Brine 346_2_09: Axial force-displacement vs time curve and the resulting zoom-in format of the displacement changes as more axial force is applied

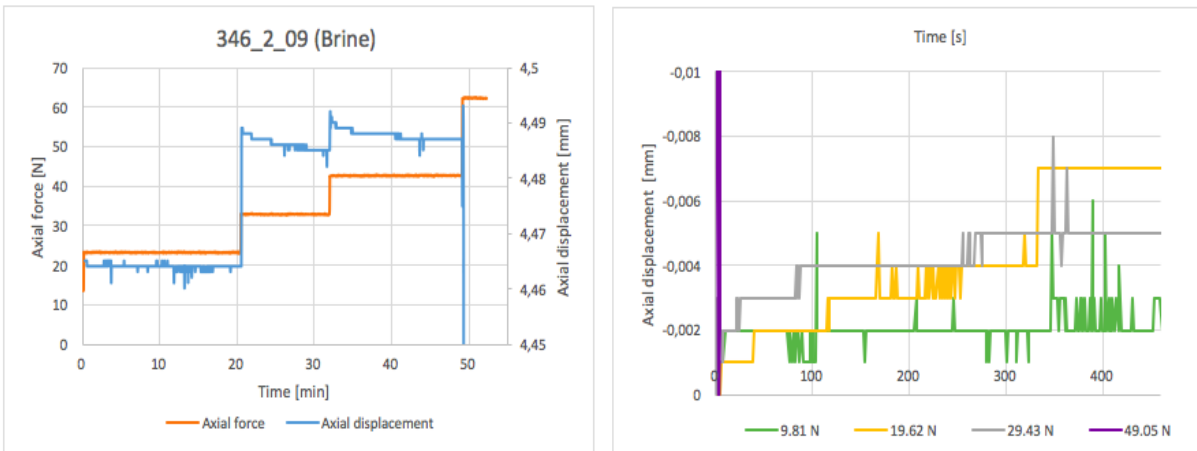


Figure A- 10 Brine 346_2_12: Axial force-displacement vs time curve and the resulting zoom-in format of the displacement changes as more axial force is applied

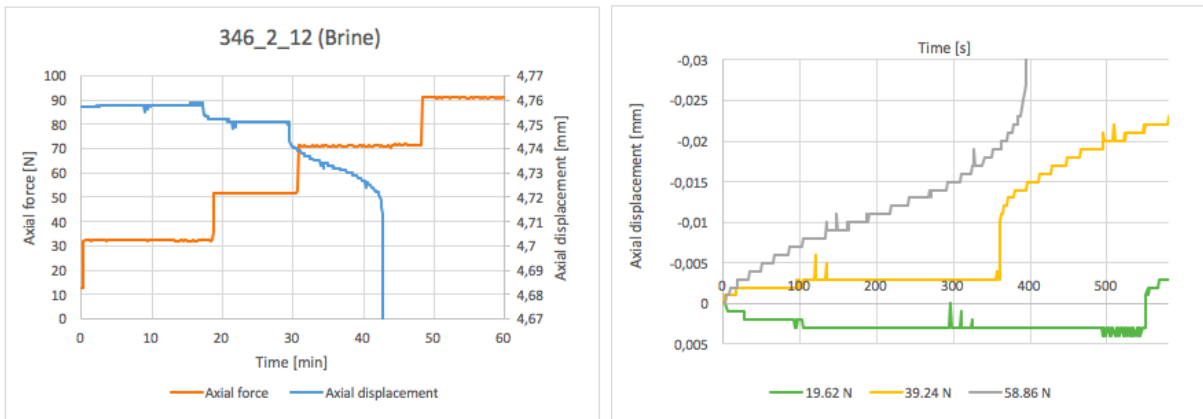


Figure A- 11 Brine 346_2_13: Axial force-displacement curve and the vs time resulting zoom-in format of the displacement changes as more axial force is applied

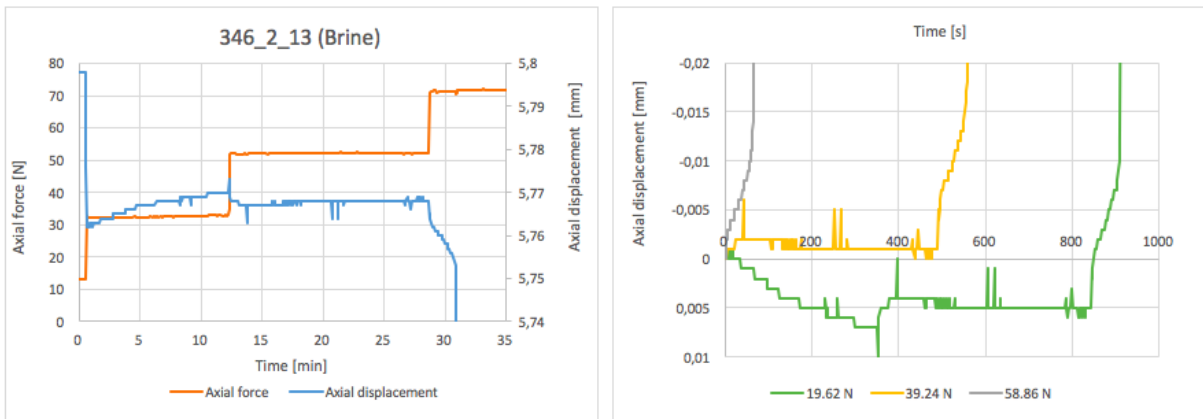


Figure A- 12 Hydrochloric acid 346_2_15: Axial force-displacement vs time curve and the resulting zoom-in format of the displacement changes as more axial force is applied

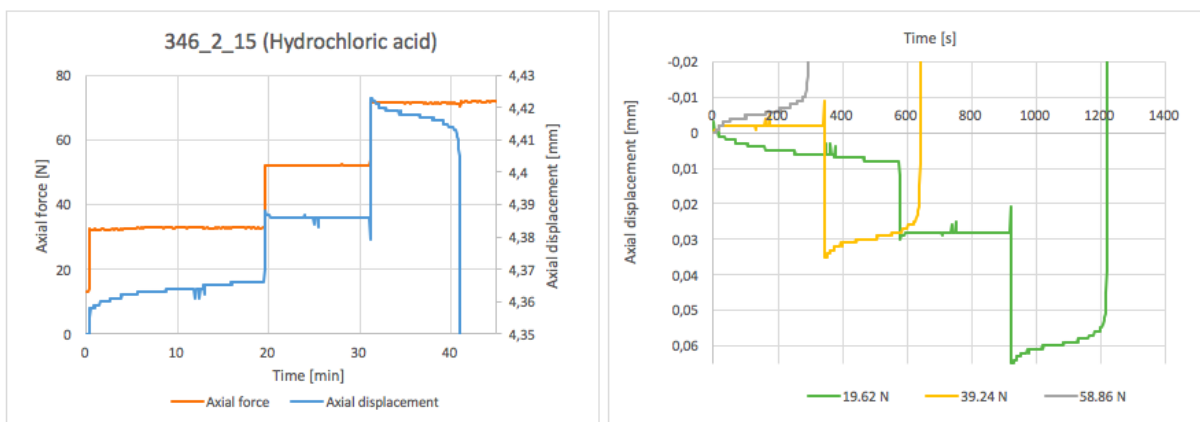
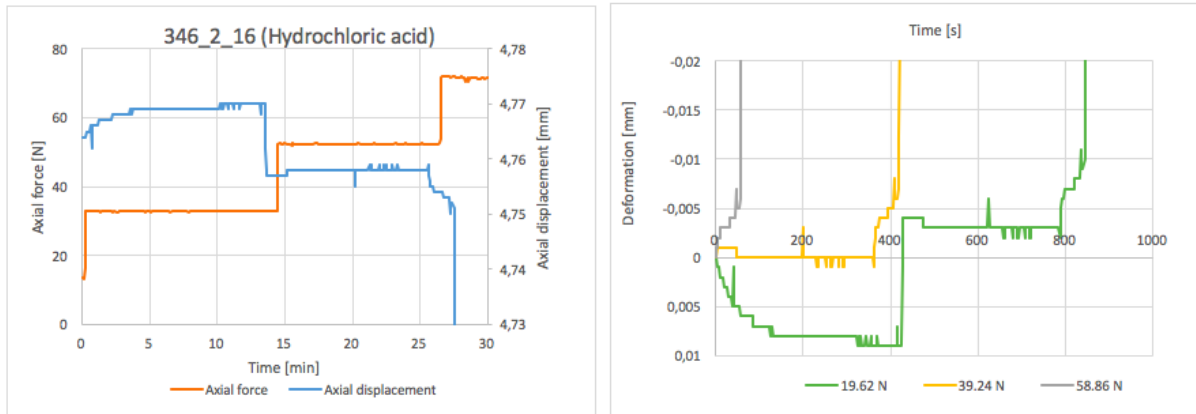


Figure A- 13 Hydrochloric acid 346_2_16: Axial force-displacement vs time curve and the resulting zoom-in format of the displacement changes as more axial force is applied



Appendix B Results: Puncher Test with Cont. Loading Path

Figure B- 1 Oil 223_3_01: Axial force and displacement vs time curve. Rate of displacement: 0.003 mm/min

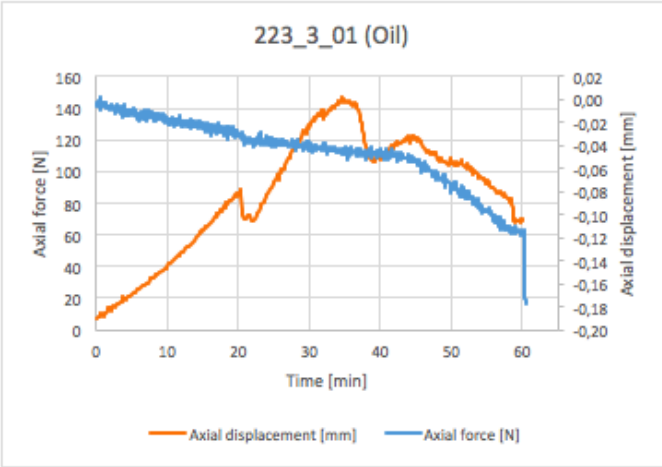


Figure B- 2 Oil 223_3_02: Axial force and displacement vs time curve. Rate of displacement: 0.01 mm/min

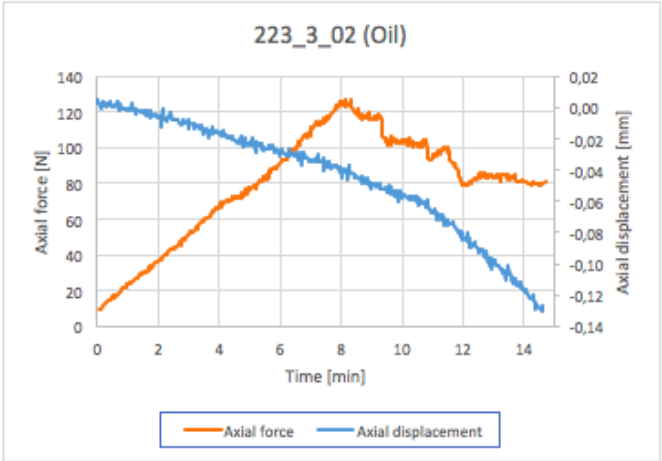


Figure B- 3 Oil 223_3_03: Axial force and displacement vs time curve. Rate of displacement: 0.02 mm/min

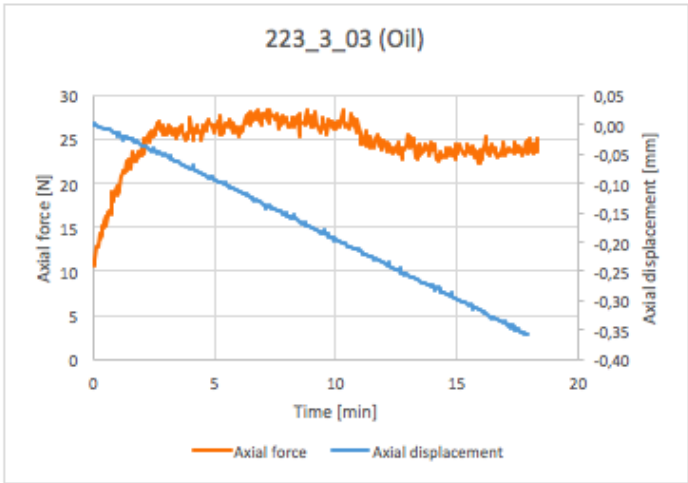


Figure B-4 Comparative axial force-displacement curve for all the oil samples

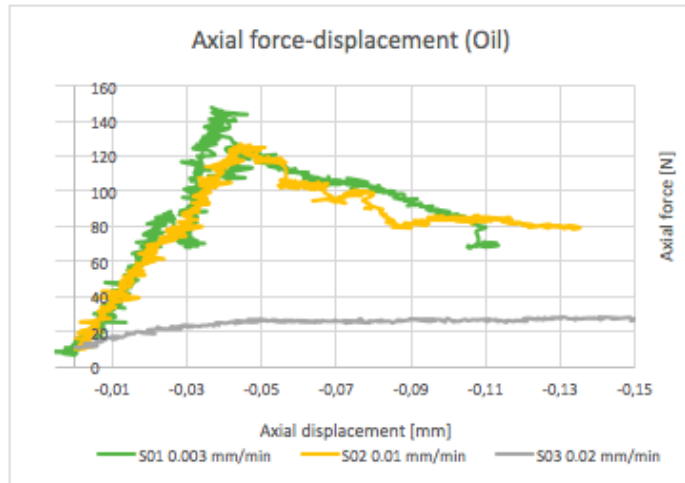


Figure B-5 Brine 223_3_04: Axial force and displacement vs time curve. Rate of displacement: 0.001 mm/min

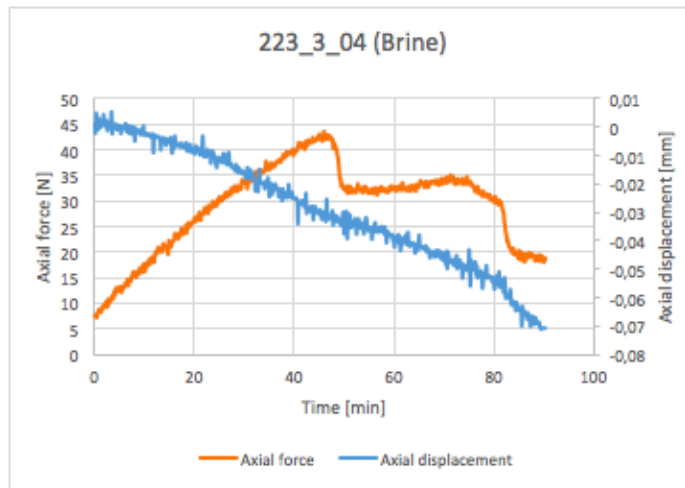


Figure B-6 Brine 223_3_05: Axial force and displacement vs time curve. Rate of displacement: 0.0025 mm/min

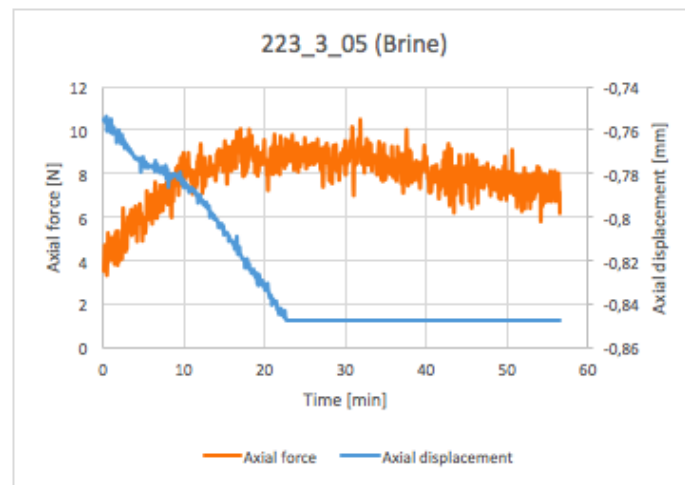


Figure B-7 Brine 223_3_06: Axial force and displacement vs time curve. Rate of displacement: 0.005 mm/min

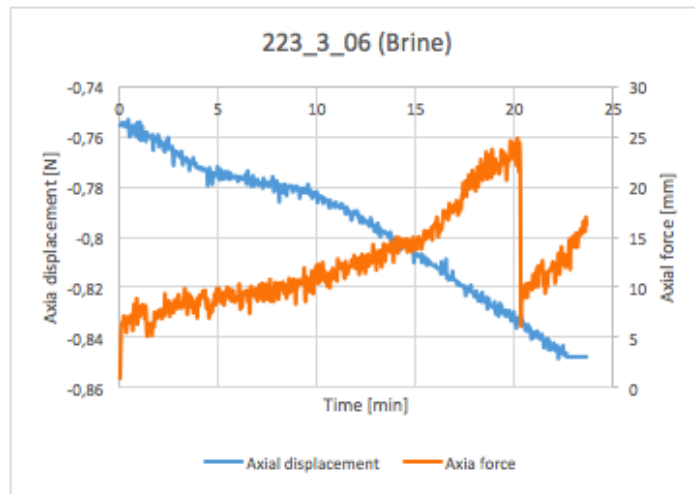


Figure B-8 Comparative axial force-displacement curves for all the brine samples

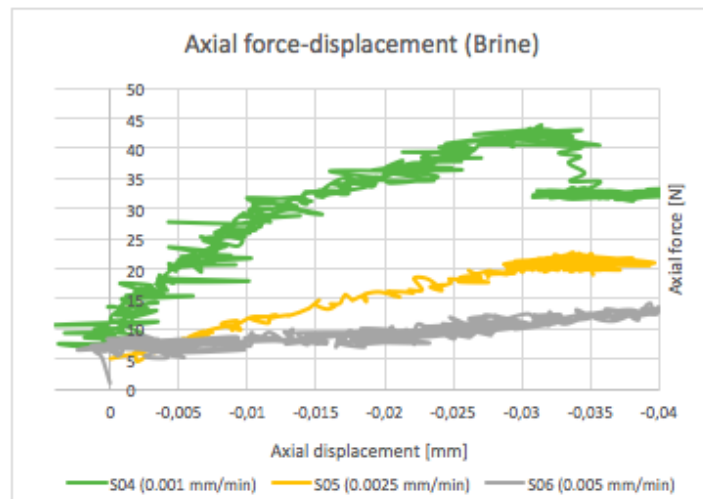


Figure B-9 Hydrochloric acid 223_3_07: Axial force and displacement vs time curve. Rate of displacement: 0.001 mm/min

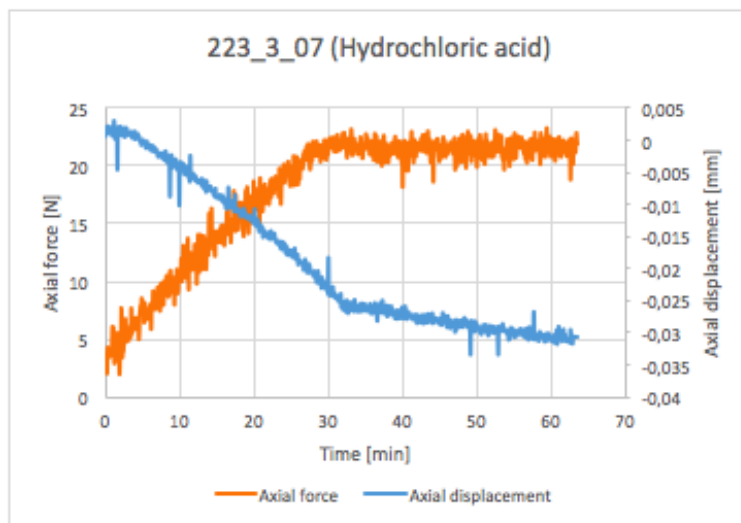


Figure B- 10 Hydrochloric acid 223_3_08: Axial force and displacement vs time curve. Rate of displacement: 0.005 mm/min

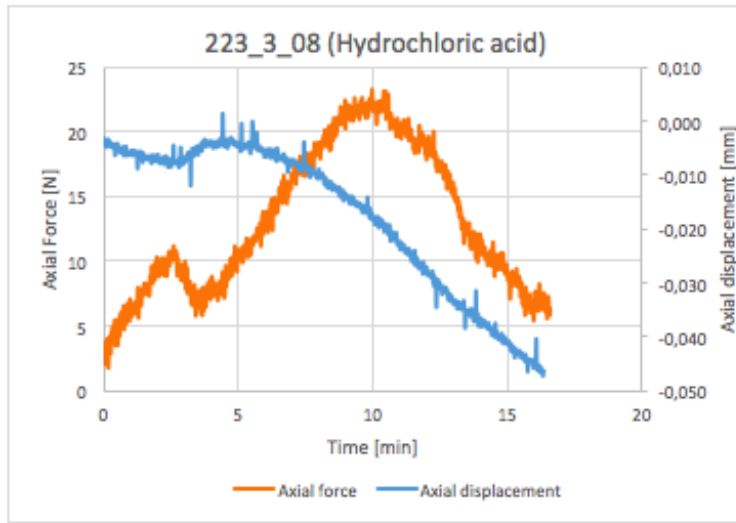


Figure B- 11 Hydrochloric acid 223_3_09: Axial force and displacement vs time curve. Rate of displacement: 0.01 mm/min

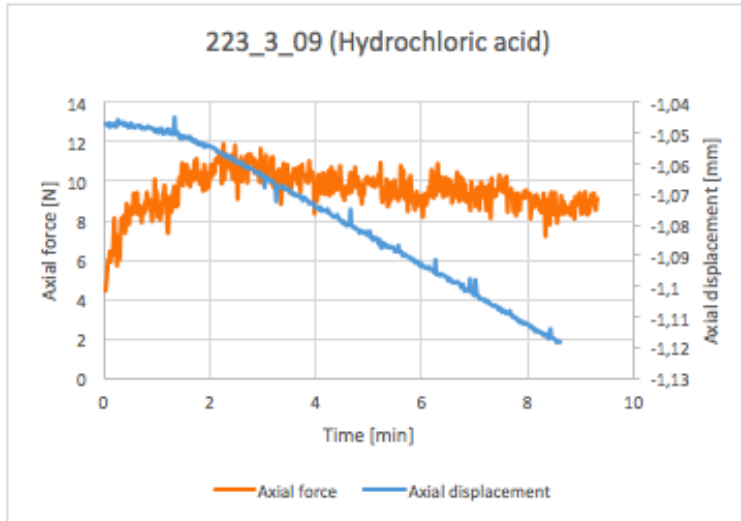


Figure B- 12 Comparative axial force-displacement curve for all two of the hydrochloric samples

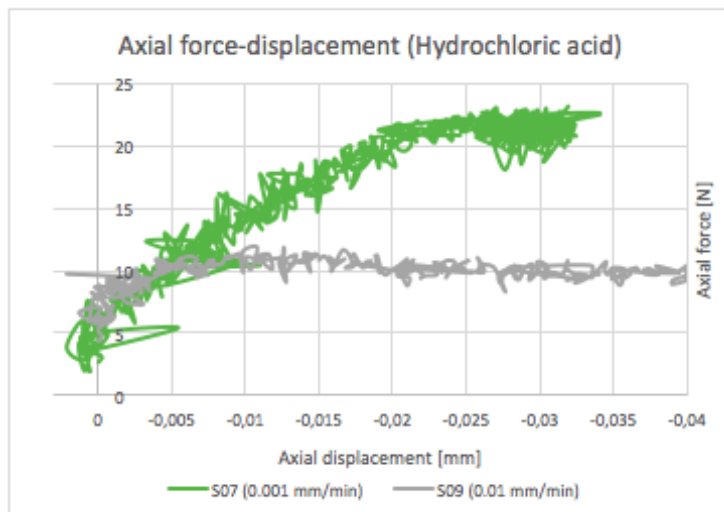
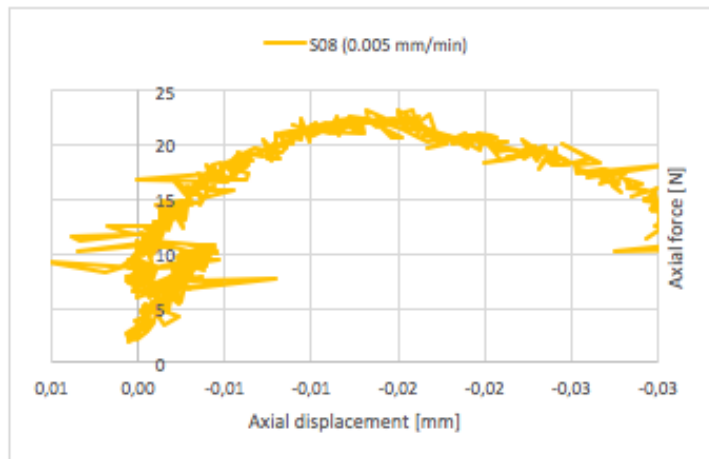


Figure B- 13 The axial force-displacement curve for 223_3_08 (discarded)



Appendix C Results: Cohesion Calculations

Table III- 1 Cohesion calculations for the oil-rich samples based on the P-wave velocities measured from CWT.

The table shows the P-wave velocity and cohesion of each sample before and after storage in marcol oil.

BEFORE STORAGE

Sample no.	P-Wave velocity from CWT		Cohesion calculations				
	V _{p,cw} [m/s]	± V _{p,cw} [m/s]	V _{p,cw} [km/s]	UCS [MPa]	Beta [Degrees]	[radians]	So [MPa]
346_2 - 01	2590	56	2,59	12,5	53,6	0,93	4,621
346_2 - 02	2637	33	2,637	13,2	53,8	0,94	4,835
346_2 - 03	2505	29	2,505	11,4	53,2	0,93	4,245
346_2 - 04	2612	46	2,612	12,8	53,6	0,94	4,721
346_2 - 05	2618	37	2,618	12,9	53,7	0,94	4,748

AFTER STORAGE

Sample no.	P-wave velocity from CWT		Cohesion calculations				
	V _{p,cw} [m/s]	± V _{p,cw} [m/s]	V _{p,cw} [km/s]	UCS [MPa]	Beta [Degrees]	[radians]	So [MPa]
346_2 - 01	2777	43	2,777	15,4	54,4	0,95	5,494
346_2 - 02	2869	81	2,869	16,9	54,9	0,96	5,943
346_2 - 03	2777	66	2,777	15,4	54,4	0,95	5,494
346_2 - 04	2805	47	2,805	15,8	54,5	0,95	5,630
346_2 - 05	2857	89	2,857	16,7	54,8	0,96	5,884

Table III- 2 Cohesion calculations based for the brine-rich samples based on the P-wave velocities measured from CWT.

The table shows the P-wave velocity and cohesion of each sample before and after storage in brine.

BEFORE STORAGE

Sample no.	P-wave velocity from CWT		Cohesion calculations				
	V _{p,cw} [m/s]	± V _{p,cw} [m/s]	V _{p,cw} [km/s]	UCS [MPa]	Beta [Degrees]	[radians]	So [MPa]
346_2 - 06	2692	61	2,692	14,0	54,0	0,94	5,091
346_2 - 07	2650	28	2,65	13,4	53,8	0,94	4,895
346_2 - 08	2512	39	2,512	11,4	53,2	0,93	4,275
346_2 - 09	2656	84	2,656	13,5	53,8	0,94	4,923
346_2 - 10	2861	79	2,861	16,8	54,8	0,96	5,903

AFTER STORAGE

Sample no.	P-wave velocity from CWT		Cohesion calculations				
	V _{p,cw} [m/s]	± V _{p,cw} [m/s]	V _{p,cw} [km/s]	UCS [MPa]	Beta [Degrees]	[radians]	So [MPa]
346_2 - 06	2355	24	2,355	9,5	52,6	0,92	3,615
346_2 - 07	2375	1	2,375	9,7	52,7	0,92	3,697
346_2 - 08	2332	35	2,332	9,2	52,6	0,92	3,523
346_2 - 09	2355	67	2,355	9,5	52,6	0,92	3,615
346_2 - 10	2259	80	2,259	8,4	52,3	0,91	3,238

Appendix D Calculations of Test Speeds

The rates of displacement (tests speeds) used for running the strain-rate experiments (223_3 series) in the electromechanical load frame is based on the typical change in displacement from the creep experiments (346_2_series). An example of the calculation of the rate of displacement for the oil samples is presented:

Considering that the test will be run approximately 15 minutes (short test), the rate of displacement will thus be:

$$t = 15 \text{ min}$$

$$UCS = 15 \text{ MPa}$$

$$90\% \text{ of } UCS = 13.5 \text{ MPa}$$

$$\Delta\varepsilon = 3.48 \text{ mm} - 3.161 \text{ mm} = 0.319 \text{ mm}$$

$$\frac{1}{E} = \frac{0.319 \text{ mm}}{13.5 \text{ MPa}} = 0.0236 \text{ mm/MPa}$$

$$\frac{\Delta\sigma}{\Delta t} = 0.9 \text{ MPa/min}$$

$$\frac{\Delta\varepsilon}{\Delta t} = 0.0236 \frac{\text{mm}}{\text{MPa}} \cdot \frac{0.9 \text{ MPa}}{\text{min}} = 0.02 \text{ mm/min}$$

Table D-1 The calculated running test speeds

Sample no.	Fluid	Calculated Test Speeds [mm/min]
223_3_01	Oil	0,00266
223_3_02	Oil	0,011062
223_3_03	Oil	0,0236
223_3_04	Brine	0,001
223_3_05	Brine	0,005
223_3_06	Brine	0,000125
223_3_07	HCl	0,001
223_3_08	HCl	0,005
223_3_09	HCl	0,000125

However, some of the test speeds were adjusted after conducting three test experiments (These results or not included in this thesis). Two test samples were run prior to the real experiments to check whether the calculated test speeds were reasonable or not. The actual running rates of displacement are presented in Table D-2.

Table D- 2 The actual running test speeds (some modifications were done after running two test experiments)

Sample no.	Fluid	Actual Running Test Speeds [mm/min]
223_3_01	Oil	0,003 mm/min
223_3_02	Oil	0,01 mm/min
223_3_03	Oil	0,02 mm/min
223_3_04	Brine	0,001 mm/min
223_3_05	Brine	0,0025 mm/min
223_3_06	Brine	0,005 mm/min
223_3_07	HCl	0,001 mm/min
223_3_08	HCl	0,005 mm/min
223_3_09	HCl	0,01 mm/min

Appendix E Additional Tables

Table E- 1 Calibration table for the load cell. The weight plates are added one by one on the load cell

Weight plates [g]	Cum. Weight [kg]	Actual Cumulative Weight [kg]
234,5	234,5	0,1892
2001,3	2235,8	2,265
2001,1	4236,9	4,234
2001,4	6238,3	6,183
1000,4	7238,7	7,209
1000,5	8239,2	8,193
1000,1	9239,3	9,206
494,6	9733,9	9,697
113,5	9847,4	9,806

Table E- 2 Test table for the concentration of hydrochloric acid, showing the measured pH and relative humidity. RH= 100=100% water

HCl (aq) Strength %	pH	Relative Humidity (RH)
0	7,31	94,2
5	-0,12	72,4
0	-0,35	63,7
15	-0,73	
1	0,29	
0,5	0,36	
0,25	0,51	
0,125	0,75	
0,025	1,36	
0,00125	3,14	93,8
0,000625	3,84	
0,0003125	4,17	
0,00015625	4,92	
0,00003906	6,23	


Table E- 3 Mineralogy composition of Pierre shale, block 346_2, given by the laboratory at SINTEF Petroleum Research

Mineral	Percentage [%]
Quartz	16
Kalifeldspar	0
Plagioclas	8,55
Chlorite	29,6
Kaolinite	0
Illite	19,9
ML	0
Smectite	19,8
Calcite	1,54
Siderite	1,43
Dolomite/Ankerite	2,63
Pyroxene	0,63

Table E- 4 Calibration of the CWT tool with a Plexiglas

Calibration attempt no.	Measured P-wave velocity [m/s]
1	2242 ± 42
2	2166 ± 19
3	2202 ± 15
4	2189 ± 21
5	2208 ± 11

Appendix F Risk Assessment

 SINTEF Enhet: IPT/SINTEF Bygning: PTS 2 Rom eller rigg / utstyr:		Dato: 2016.02.02 Deltagere: Anna Guan Linjeleder:										
Id	Aktivitet	Mulig uønsket hendelse	Eksisterende barrierer	Risikoverdi med eksisterende tiltak				Nye barrierer / risikoreducerende tiltak (handlingsplan)	Risikoverdi med nye tiltak			
				Menneske	Ytre miljø	Omdømme	Økonomi / materiell		Menneske	Ytre miljø	Omdømme	Økonomi / materiell
1	Adjusting loadframe.	Damage to equipment.	Emergency breaks on loadframe.	A1	A1	A1	B3	A1	A1	A1	B2	
2	Adjusting loadframe.	Damage to hands.		C2	A1	A1	A1	C1	A1	A1	A1	
3	Wrong/improper use of equipment.	Damage of expensive equipment.	User manual for the equipment.	A1	A1	A1	C3	A1	A1	A1	C2	
4	Wrong/improper use of equipment.	Damage to personnel.	Protective gear.	C3	A1	A1	A1	C2	A1	A1	A1	
5	Use of heating element.	Damage to personnel and short circuiting. Smoke emission.	Steel frame between salt liquid and heating element.	B1	A1	A1	A1	A1	A1	A1	A1	
6	Moving around inside the lab.	Damage to personnel due to slippery floor.	Stay inside marked guidelines when leaving your work station. Use proper shoes.	A3	A1	A1	A1	A2	A1	A1	A1	

MATRISSE FOR RISIKOVURDERINGER I SINTEF

KONSEKVENSENS	Svært alvorlig	E1	E2	E3	E4	E5
	Alvorlig	D1	D2	D3	D4	D5
	Moderat	C1	C2	C3	C4	C5
	Liten	B1	B2	B3	B4	B5
	Svært liten	A1	A2	A3	A4	A5
		Svært liten	Liten	Middels	Stor	Svært stor
		SANNSYNLIGHET				

Prinsipp over akseptkriterium. Forklaring av fargene som er brukt i risikomatrisen.

Farge	Beskrivelse
Rød	Uakseptabel risiko. Tiltak skal gjennomføres for å redusere risikoen.
Gul	Vurderingsområde. Tiltak skal vurderes.
Grønn	Akseptabel risiko. Tiltak kan vurderes ut fra andre hensyn.

Sannsynlighet		
1	Svært liten	Sjeldnere enn en gang hvert 50. år.
2	Liten	Mellom en gang hvert 10. år og en gang hvert 50. år.
3	Middels	Mellom en gang hvert år og en gang hvert 10. år.
4	Stor	Mellom en gang hver måned og en gang hvert år.
5	Svært stor	Oftere enn hver måned.

Konsekvensmatrise				
	Personskade	Skade på ytre miljø	Økonomisk tap / Materiell skade	Skade på omdømme
E	Død	Svært langvarig og ikke-reversibel skade	Tap på mer enn NOK 5 mill	Troverdighet og respekt betydelig og varig svekket
D	Alvorlig personskade/ mulig uferhet	Langvarig skade Lang restitusjonstid	Tap opp til NOK 5 mill	Troverdighet og respekt betydelig svekket.
C	Alvorlig personskade	Mindre skade og lang restitusjonstid	Tap opp til NOK 1 mill	Troverdighet og respekt svekket.
B	Medisinsk behandling	Mindre skade og kort restitusjonstid	Tap opp til NOK 250.000	Negativ påvirkning på troverdighet og respekt
A	Førstehjelp	Ubetydelig skade og kort restitusjonstid	Tap opp til NOK 50.000	Liten påvirkning på troverdighet og respekt

Appendix G Pictures of Shale Samples

Figure G- 1 Sample before testing (left) and punched sample (right)

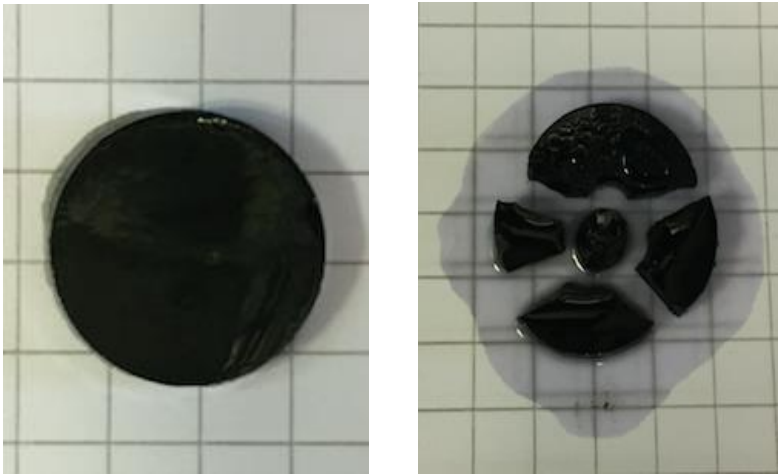


Figure G- 2 Disintegrated shale sample caused by the exposure to hydrochloric acid



Figure G- 3 Disintegrated shale sample caused by the exposure to brine. The surface of the sample is crumbled.

